Theory of Phasor-Field Imaging

by

Justin Dove

B.S., Adelphi University (2012)
S.M., Massachusetts Institute of Technology (2014)

Submitted to the
Department of Electrical Engineering and Computer Science
in partial fulfillment of the requirements for the degree of

Doctor of Philosophy

at the

MASSACHUSETTS INSTITUTE OF TECHNOLOGY

May 2020

Author . . . .
Department of Electrical Engineering and Computer Science
May 15, 2020

Certified by . . . .
Jeffrey H. Shapiro
Julius A. Stratton Professor of Electrical Engineering
Thesis Supervisor

Accepted by . . . .
Leslie A. Kolodziejski
Professor of Electrical Engineering and Computer Science
Chair, Department Committee on Graduate Students

Theory of Phasor-Field Imaging

by

Justin Dove

Submitted to the Department of Electrical Engineering and Computer Science
on May 15, 2020, in partial fulfillment of the
requirements for the degree of
Doctor of Philosophy

Abstract

Phasor-field ($\mathcal{P}$-field) imaging is a promising recent solution to the task of non-line-of-sight (NLoS) imaging, colloquially referred to as "seeing around corners". It consists of treating the oscillating envelope of amplitude-modulated, spatially-incoherent light as if it were itself an optical wave, akin to the oscillations of the underlying electromagnetic field. We present a formal analysis of $\mathcal{P}$-field propagation using paraxial wave optics and demonstrate how it can be used to form images of hidden diffuse targets both computationally and with physical lenses. In both cases, we find that hidden target planes can be imaged at the modulation-wavelength diffraction limit, despite the presence of intervening diffusers. To model propagation through more general scenarios, we introduce the two-frequency spatial Wigner distribution and derive primitives that characterize its behavior. These primitives are used to analyze occlusion-aided imaging scenarios as well as to verify intuitive results in the geometric-optics limit. Consistent with prior work, we find that intervening occluders offer the potential to form convolutional images of hidden target planes, even in the absence of time-of-flight information. Additionally, we demonstrate how to extend our framework beyond the paraxial regime and include a thorough exploration of the effects of speckle, which we find are likely manageable in realistic scenarios.

Thesis Supervisor: Jeffrey H. Shapiro
Title: Julius A. Stratton Professor of Electrical Engineering

Acknowledgments

Contents

List of Figures

List of Tables

Chapter 1

Introduction

Non-line-of-sight (NLoS) imaging, colloquially known as imaging around corners, is an important and growing area of research in the imaging community. Kirmani *et al.* [1] introduced the concept of transient NLoS imaging by using short pulses and time-resolved detection together with multipath analysis to recover the geometry of simple, occluded scenes. Their approach was independent of bidirectional reflectance distribution function (BRDF) and albedo, and they demonstrated its experimental feasibility. Velten *et al.* [2] revisited the problem, focusing on the case of diffuse reflection, using ultrafast streak cameras and computational backprojection. With these more powerful and developed tools, they were able to demonstrate human-identifiable reconstructions of relatively detailed geometry from around a corner. A major obstacle to applying Velten *et al.*'s approach in practice is the relative expense of their advanced equipment. This barrier was addressed by Heide *et al.* [3] who applied similar techniques with success to data collected by relatively inexpensive photonic-mixer-device (PMD) time-of-flight sensors. Buttafava *et al.* [4] also improved upon the practical feasibility—bearing in mind cost, power, size, etc.— of implementing these approaches by demonstrating NLoS imaging with single-photon avalanche diode (SPAD) detectors. Whereas all of this work had focused on static geometry reconstruction, Gariepy *et al.* [5] extended these techniques, using SPAD detectors, to detect motion and track moving objects around corners. With an awareness of the breadth of the preceding work, Kadambi *et al.* [6] provided a unified

theoretical framework for the problem of occluded geometry reconstruction and motion tracking, including an analysis of expected performance and a consideration of commercially available equipment. They also generalized their theory to deal with imaging through diffusers in addition to the around-the-corner scenario and offered experimental demonstration of the effectiveness of their framework. Pointing out that the experimentally collected data in the previous literature had quality and resource issues owing to experimental practicalities, Klein *et al.* [7] developed a simulation engine fit for thinking more broadly about NLoS imaging tasks without the limitations of real data. Additionally, leveraging their newfound ability to quickly simulate NLoS scenarios, they developed and demonstrated a new simulation-based inversion technique as an alternative to the computational backprojection methods that had been used in most of the prior work. Making further improvements in the area of reconstruction techniques and coping with practical resource limitations, O'Toole *et al.* [8] demonstrated a confocal NLoS imaging system which facilitated the development and use of a closed-form inversion formula.

With the goal of further advancing the field of NLoS imaging, Reza *et al.* [9] recently introduced the phasor-field ($\mathcal{P}$-field) representation for light transport that involves diffuse reflection (such as occurs in NLoS imaging) or diffuse transmission. The phasor-field concept exploits the wave-like propagation behavior of the oscillating envelope of amplitude-modulated, spatially-incoherent light. It relies on the fact that the physical correlates of diffuse phase disruption, while being large compared to the wavelength of the optical carrier field, are insignificant in scale to the much longer wavelength of radio-frequency amplitude modulation. As a result, walls that diffusely scatter light, owing to their roughness at the optical-wavelength scale (as shown in Fig. 1-1), appear smooth to the $\mathcal{P}$ field, and thin transmissive diffusers appear invisible. The upshot is that traditional wave-optical imaging techniques, e.g., lenses, can be applied despite the presence of these optically disruptive elements.

Attempting to apply Reza *et al.*'s light transport model to NLoS geometries that include intervening occluding objects or non-Lambertian reflections will reveal that the $\mathcal{P}$-field is an insufficient summary of the underlying field at the site of such fea-

16
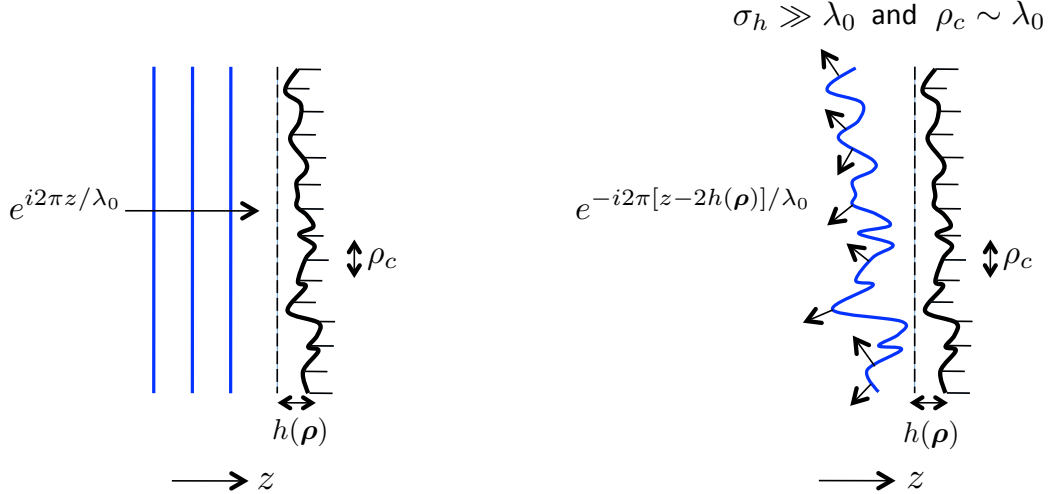
Figure 1-1: Illustration of diffuse scattering of an incident plane wave (left) by a rough, reflective surface by means of distorting the reflected wavefront (right). λ_0 represents the optical wavelength and $h(\boldsymbol{\rho})$ represents the height fluctuations of the surface, with standard deviation $\sigma_h \gg \lambda_0$ and correlation length $\rho_c \sim \lambda_0$. In isotropic media like air, light propagates perpendicular to surfaces of constant phase. Hence, the phase disruption induced by the surface scatters light in all directions, shown here by small black arrows normal to the reflected wavefront.

tures. Nevertheless, Liu *et al.* [10] used the $\mathcal{P}$-field approach to propose and demonstrate that line-of-sight imaging techniques can be fruitfully applied, in a computational manner, to NLoS operation, even in the presence of intervening occluders and non-Lambertian reflections. In doing so, they presented what may be the most robust and detailed reconstructions of NLoS scenes to date. Their success in this endeavor is due to their development of reconstruction techniques that obviate the need for a full light transport model by relying on there being initial and final Lambertian reflections. These techniques are fortunately, and somewhat surprisingly, not burdened by the limitations inherent in applying $\mathcal{P}$-field propagation to scenarios more general than purely Lambertian reflections. The success of Liu *et al.*'s experiments is impressive and promising. However, we believe that even greater performance might be possible if afforded a complete transport model that can account for all features that might be encountered in NLoS imaging. At the very least, such a transport model would facilitate anticipatory preparation and analysis for particular scenarios of interest. The argument could be made that the propagation rules for the optical-

17

frequency field—not those for the $\mathcal{P}$-field—already provide such a transport model, but the aforementioned work has demonstrated the intuitive utility of the $\mathcal{P}$-field approach. Consequently, we believe it is worthwhile to pursue propagation primitives that can establish the $\mathcal{P}$-field input-output relation for the initial and final Lambertian reflections when occluders and non-Lambertian reflectors are present in the intervening space.

In this thesis, we develop a set of propagation primitives that extend the $\mathcal{P}$-field formalism to scenarios that go beyond what was considered in Ref. [9]. For convenience, we mostly assume a transmissive geometry (without reflections) that is an unfolded proxy for occlusion-aided, three-bounce NLoS imaging [11, 12] and use scalar-wave, paraxial optics although these restrictions are not essential. In Chapter 2 we present our own development and analysis of the $\mathcal{P}$-field notion. We begin by tracing light propagation through an example transmissive geometry wherein a natural definition for the $\mathcal{P}$ field presents itself. Continuing this analysis, we arrive at a paraxial $\mathcal{P}$-field propagator analogous to that reported by Reza *et al.* [9]. Using this result, we analyze the performance of $\mathcal{P}$-field imaging for unoccluded transmissive geometries using a computational approach to reconstruction. Then, we derive a set of primitives characterizing $\mathcal{P}$-field propagation through lenses and demonstrate how images can be reconstructed physically. Next, moving beyond the $\mathcal{P}$-field, in Chapter 3 we introduce the two-frequency spatial Wigner distribution (TFSWD) and derive primitives for its propagation through a diffuser, through a deterministic occluder, through a specular-plus-diffuser mask, and through Fresnel diffraction. With these primitives, we then derive the $\mathcal{P}$-field input-output relation for occlusion-aided, diffuse-object, transmissive imaging. With that analysis in hand, we compare the $\mathcal{P}$-field point-spread function for diffuse-object imaging using modulated light in the absence of an occluder with those for diffuse-object imaging using unmodulated light that is aided by the presence of either a Gaussian-pinhole occluder or a Gaussian-pinspeck occluder. We then abstract these results by deriving a $\mathcal{P}$-field input-output relation for occluder-interrupted, post-diffuser propagation and verify an intuitive simplification of this result in the geometric-optics limit. In Chapter 4 we extend our formalism be-

yond the paraxial regime. In particular, we show how our Fresnel propagation results for the $\mathcal{P}$ field can be extended to Rayleigh–Sommerfeld propagation. Then, using an intuitive geometric argument, we propose equivalent behavior for the TFSWD. We verify that it reproduces the expected $\mathcal{P}$-field result and provide a more formal derivation for the special case of partial coherence. Additionally, we derive a pair of differential equations that characterize the TFSWD more generally. In Chapter 5 we consider the effects of speckle. We start by analyzing multi-bounce speckle effects for monochromatic illumination and consider how geometry and averaging techniques can reduce speckle's ill effects. Then we explore the effects of first-order speckle on modulated illumination and investigate a concrete example. The impact on overall signal-to-noise ratio in conjunction with shot noise is considered, and a treatment of speckle in the limit of small reflectors is provided, where we find additional results can be derived. Finally, in Chapter 6 we summarize our results and consider options for future work.

Chapter 2

$\mathcal{P}$-Field Propagation and Imaging

In this chapter we consider electromagnetic field propagation through a paraxial, transmissive geometry that serves as a surrogate for an around-the-corner imaging configuration.[1] As was done by Reza *et al.* [9], we define the $\mathcal{P}$ field as the Fourier transform of the diffuser-averaged short-time average (STA) irradiance. Using this definition, we derive a formula for paraxial propagation of the $\mathcal{P}$ field, which we find to be similar to the traditional Fresnel-diffraction formula for the propagation of the electromagnetic field, as reported by Reza *et al.* [9]. We then apply this understanding of the $\mathcal{P}$ field to the task of computationally imaging through diffusers and analyze the associated performance. Finally, we consider how the $\mathcal{P}$ field interacts with a variety of lens configurations and demonstrate that targets hidden by diffusers can be directly imaged physically, i.e., without the need for nontrivial computation.

2.1 Setup for Paraxial Propagation through Multiple Diffusers

Figure 2-1 shows the transmissive geometry we shall address in this chapter for $\mathcal{P}$-field propagation within the paraxial regime, i.e., wherein Fresnel diffraction applies.

---

[1] Throughout this thesis, we will work almost entirely with such paraxial, transmissive geometries. Extending our techniques to nonparaxial propagation is discussed in Chapter 4, and a discussion of how our transmissive framework can be applied to typical reflective geometries can be found in Appendix A.

Here, $E_0(\boldsymbol{\rho}_0, t)$ is the baseband, complex field envelope for a quasimonochromatic, scalar-wave, modulated laser field entering the $z = 0$ plane, expressed as a function of the transverse spatial coordinates, $\boldsymbol{\rho}_0 = (x_0, y_0)$, and time, t. This field has center frequency ω_0 and bandwidth $\Delta\omega \ll \omega_0$, so that the optical-frequency field is $\text{Re}[E_0(\boldsymbol{\rho}_0, t)e^{-i\omega_o t}]$. Its units are $\sqrt{\text{W/m}^2}$, making $I_0(\boldsymbol{\rho}_0, t) = |E_0(\boldsymbol{\rho}_0, t)|^2$ the STA irradiance[2] illuminating the $z = 0$ plane. It will be assumed, in all that follows, that $\Delta\omega$ is such that available photodetectors can fully resolve the time dependence of $I_0(\boldsymbol{\rho}_0, t)$. As soon will be seen, it will be valuable to employ the time-domain Fourier transform of $E_0(\boldsymbol{\rho}_0, t)$, viz.[3],

$$\mathcal{E}_0(\boldsymbol{\rho}_0, \omega) \equiv \int \mathrm{d}t\, E_0(\boldsymbol{\rho}_0, t)e^{i\omega t}, \tag{2.1}$$

for use analyzing the Fig. 2-1 configuration.
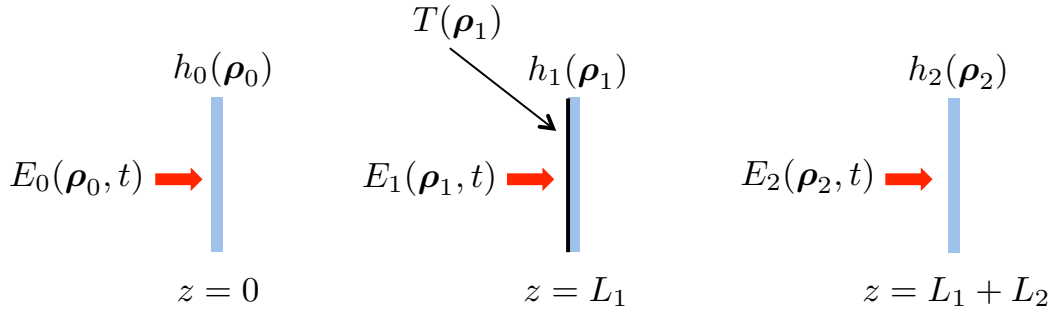
Figure 2-1: Unfolded geometry for three-bounce NLoS active imaging. Scalar, paraxial diffraction theory is assumed, with $\{E_k(\boldsymbol{\rho}_k, t) : 0 \le k \le 2\}$ being the baseband complex field envelopes illuminating the $z = 0$, $z = L_1$, and $z = L_1 + L_2$ planes, respectively, written as functions of the transverse spatial coordinates, $\{\boldsymbol{\rho}_k = (x_k, y_k) : 0 \le k \le 2\}$, in those planes and time, t. The blue rectangles represent thin transmissive diffusers, and the black line represents a thin transmission screen whose intensity transmission pattern, $T(\boldsymbol{\rho}_1)$, is to be imaged using the light that emerges from the $z = L_1 + L_2$ plane.

After propagating through the thin diffuser $h_0(\boldsymbol{\rho}_0)$, the Fourier-domain field at $z = 0_+$ is

$$\mathcal{E}_0'(\boldsymbol{\rho}_0, \omega) = \mathcal{E}_0(\boldsymbol{\rho}_0, \omega) \exp[i(\omega_0 + \omega)h_0(\boldsymbol{\rho}_0)/c], \tag{2.2}$$

---

[2] The STA z-plane irradiance is the instantaneous irradiance averaged over a time T_a satisfying $\omega_0 T_a \gg 1$ and $\Delta\omega T_a \ll 1$.

[3] In what follows, integrals without explicit limits are over the integration variable's entire domain.

where c is light speed and we have normalized away the diffuser's refractive index. Physically, we are modeling this diffuser as a space-dependent $h_0(\boldsymbol{\rho}_0)/c$ time delay. Because it is unreasonable to presume we can accurately account for this delay as a deterministic quantity, we shall suppress its average value—across an ensemble of statistically identical diffusers—and consider $h_0(\boldsymbol{\rho}_0)$ to be a zero-mean, homogeneous, isotropic, Gaussian random function of $\boldsymbol{\rho}_0$, with covariance function $K_h(|\Delta\boldsymbol{\rho}|) = \langle h_0(\boldsymbol{\rho}_0 + \Delta\boldsymbol{\rho})h_0(\boldsymbol{\rho}_0)\rangle$, where angle brackets denote ensemble average. Moreover, in keeping with $h_0(\boldsymbol{\rho}_0)$'s being a diffuser, we shall take its standard deviation, $\sigma_h = \sqrt{K_h(0)}$ to be much greater than the center wavelength, $\lambda_0 = 2\pi c/\omega_0$, and its coherence length ρ_c—the transverse distance beyond which $K_h(|\Delta\boldsymbol{\rho}|)$ vanishes—to be at most a few λ_0. Furthermore—and this condition is essential to there being a useful $\mathcal{P}$-field propagator—we shall assume that σ_h is much *smaller* than the wavelength of the modulation bandwidth, $\Delta\lambda = 2\pi c/\Delta\omega$.

Within the paraxial (Fresnel-diffraction) propagation regime we have that

$$\mathcal{E}_1(\boldsymbol{\rho}_1,\omega) = \int \mathrm{d}^2\boldsymbol{\rho}_0 \, \mathcal{E}_0'(\boldsymbol{\rho}_0,\omega) \frac{\exp[i(\omega_0+\omega)L_1/c + i(\omega_0+\omega)|\boldsymbol{\rho}_1 - \boldsymbol{\rho}_0|^2/2cL_1](\omega_0+\omega)}{i2\pi cL_1},$$
(2.3)

is the time-domain Fourier transform of $E_1(\boldsymbol{\rho}_1,t)$, the field illuminating the $z = L_1$ plane. This illumination results in

$$\mathcal{E}_1'(\boldsymbol{\rho}_1,\omega) = \mathcal{E}_1(\boldsymbol{\rho}_1,\omega)\sqrt{T(\boldsymbol{\rho}_1)}\exp[i(\omega_0+\omega)h_1(\boldsymbol{\rho}_1)/c], \tag{2.4}$$

being the time-domain Fourier transform of $E_1'(\boldsymbol{\rho}_1,t)$, the field that emerges at $z = L_{1_+}$, after propagation through a deterministic thin transmission screen with intensity transmission pattern $T(\boldsymbol{\rho}_1)$, and a thin diffuser, $h_1(\boldsymbol{\rho}_1)$, that we will take to be statistically independent of, but identically distributed as, $h_0(\boldsymbol{\rho}_0)$.

Paraxial propagation to $z = L_1 + L_2$, now gives us

$$\mathcal{E}_2(\boldsymbol{\rho}_2,\omega) = \int \mathrm{d}^2\boldsymbol{\rho}_1 \, \mathcal{E}_1'(\boldsymbol{\rho}_1,\omega) \frac{\exp[i(\omega_0+\omega)L_2/c + i(\omega_0+\omega)|\boldsymbol{\rho}_2 - \boldsymbol{\rho}_1|^2/2cL_2](\omega_0+\omega)}{i2\pi cL_2},$$
(2.5)

and propagation through the thin diffuser at $z = L_1 + L_2$ results in

$$\mathcal{E}_2'(\boldsymbol{\rho}_2, \omega) = \mathcal{E}_2(\boldsymbol{\rho}_2, \omega) \exp[i(\omega_0 + \omega)h_2(\boldsymbol{\rho}_2)/c], \tag{2.6}$$

being the time-domain Fourier transform of $E_2'(\boldsymbol{\rho}_2, t)$, the field that emerges at $z = (L_1 + L_2)_+$. We will assume that $h_2(\boldsymbol{\rho}_2)$ is statistically independent of, but identically distributed as, $h_0(\boldsymbol{\rho}_0)$ and $h_1(\boldsymbol{\rho}_1)$.

Before proceeding further, let us briefly comment on how the Fig. 2-1 geometry relates to three-bounce NLoS active imaging. The $z = 0$ diffuser, which is illuminated by modulated laser light, represents a Lambertian-reflecting visible wall with a uniform albedo. The combination of the intensity transmission pattern $T(\boldsymbol{\rho}_1)$ and the $z = L_1$ diffuser represent a Lambertian-reflecting hidden wall with spatially-varying albedo $T(\boldsymbol{\rho}_1)$. The $z = L_1 + L_2$ diffuser represents a second Lambertian reflection at the visible wall, where statistical independence from the first visible-wall reflection can be ensured by the NLoS imaging sensor's viewing a different section of that wall than what the laser illuminates. The goal of three-bounce NLoS active imaging in this setting is to use the third-bounce light returned from the visible wall to reconstruct the hidden wall's albedo $T(\boldsymbol{\rho}_1)$. In the next section, we will derive the $\mathcal{P}$-field propagator for the preceding transmission geometry.

2.2 $\mathcal{P}$-Field Propagator in the Paraxial Regime

To start our derivation, consider $\langle I_1(\boldsymbol{\rho}_1, t) \rangle$, where $I_1(\boldsymbol{\rho}_1, t) \equiv |E_1(\boldsymbol{\rho}_1, t)|^2$ is the STA irradiance illuminating the $z = L_1$ plane and angle brackets denote averaging over the statistics of $h_0(\boldsymbol{\rho}_0)$. Going to the temporal-frequency domain, we have that

$$\langle I_1(\boldsymbol{\rho}_1, t) \rangle = \int \frac{\mathrm{d}\omega}{2\pi} \int \frac{\mathrm{d}\omega'}{2\pi} \langle \mathcal{E}_1(\boldsymbol{\rho}_1, \omega)\mathcal{E}_1^*(\boldsymbol{\rho}_1, \omega') \rangle e^{-i(\omega-\omega')t} \tag{2.7}$$

$$= \int \frac{\mathrm{d}\omega_-}{2\pi} \left[\int \frac{\mathrm{d}\omega_+}{2\pi} \langle \mathcal{E}_1(\boldsymbol{\rho}_1, \omega_+ + \omega_-/2)\mathcal{E}_1^*(\boldsymbol{\rho}_1, \omega_+ - \omega_-/2) \rangle \right] e^{-i\omega_- t} \tag{2.8}$$

$$= \int \frac{\mathrm{d}\omega_-}{2\pi} \mathcal{P}_1(\boldsymbol{\rho}_1, \omega_-) e^{-i\omega_- t}, \tag{2.9}$$

24

where $*$ denotes complex conjugate, $\omega_+ \equiv (\omega + \omega')/2$, $\omega_- \equiv \omega - \omega'$, and we have introduced the $\mathcal{P}$ field at the $z = L_1$ plane as the Fourier transform of $\langle I_1(\boldsymbol{\rho}_1, t) \rangle$. Next, employing Eqs. (2.2) and (2.3), we get

$$\mathcal{P}_1(\boldsymbol{\rho}_1, \omega_-) = \int d^2\boldsymbol{\rho}_0 \int d^2\boldsymbol{\rho}_0' \int \frac{d\omega_+}{2\pi} \mathcal{E}_0(\boldsymbol{\rho}_0, \omega)\mathcal{E}_0^*(\boldsymbol{\rho}_0', \omega')\langle e^{i[(\omega_0+\omega)h_0(\boldsymbol{\rho}_0)-(\omega_0+\omega')h_0(\boldsymbol{\rho}_0')]/c}\rangle$$

$$\times (\omega_0 + \omega)(\omega_0 + \omega')e^{i(\omega-\omega')L_1/c+i[(\omega_0+\omega)|\boldsymbol{\rho}_1-\boldsymbol{\rho}_0|^2-(\omega_0+\omega')|\boldsymbol{\rho}_1-\boldsymbol{\rho}_0'|^2]/2cL_1}/(2\pi cL_1)^2, \quad (2.10)$$

where, as before, $\omega_+ \equiv (\omega + \omega')/2$ and $\omega_- \equiv \omega - \omega'$. Because $\Delta\omega \ll \omega_0$ and $\sigma_h \ll \Delta\lambda$, the preceding result can be reduced to

$$\mathcal{P}_1(\boldsymbol{\rho}_1, \omega_-) = \int d^2\boldsymbol{\rho}_0 \int d^2\boldsymbol{\rho}_0' \int \frac{d\omega_+}{2\pi} \mathcal{E}_0(\boldsymbol{\rho}_0, \omega)\mathcal{E}_0^*(\boldsymbol{\rho}_0', \omega')\langle e^{i\omega_0[h_0(\boldsymbol{\rho}_0)-h_0(\boldsymbol{\rho}_0')]/c}\rangle\omega_0^2/(2\pi cL_1)^2$$

$$\times e^{i(\omega-\omega')L_1/c+i[(\omega_0+\omega)|\boldsymbol{\rho}_1-\boldsymbol{\rho}_0|^2-(\omega_0+\omega')|\boldsymbol{\rho}_1-\boldsymbol{\rho}_0'|^2]/2cL_1}. \quad (2.11)$$

Since $h_0(\boldsymbol{\rho})$ is a zero-mean Gaussian process, its samples at $\boldsymbol{\rho}_0$ and $\boldsymbol{\rho}_0'$ are zero-mean jointly Gaussian random variables whose joint characteristic function is given by

$$\langle e^{i\omega_0[h_0(\boldsymbol{\rho}_0)-h_0(\boldsymbol{\rho}_0')]/c}\rangle = \exp\{-\omega_0^2[\sigma_h^2 - K_h(|\boldsymbol{\rho}_0 - \boldsymbol{\rho}_0'|)]/c^2\}. \quad (2.12)$$

Then, because $\sigma_h \gg \lambda_0$ and $\rho_c \sim \lambda_0$ we can use an impulse approximation, viz.,

$$\langle e^{i\omega_0[h_0(\boldsymbol{\rho}_0)-h_0(\boldsymbol{\rho}_0')]/c}\rangle \approx \lambda_0^2\delta(\boldsymbol{\rho}_0 - \boldsymbol{\rho}_0'), \quad (2.13)$$

in Eq. (2.11) to obtain

$$\mathcal{P}_1(\boldsymbol{\rho}_1, \omega_-) = \int d^2\boldsymbol{\rho}_0 \int \frac{d\omega_+}{2\pi} \mathcal{E}_0(\boldsymbol{\rho}_0, \omega)\mathcal{E}_0^*(\boldsymbol{\rho}_0, \omega')e^{i(\omega-\omega')L_1/c+i(\omega-\omega')|\boldsymbol{\rho}_1-\boldsymbol{\rho}_0|^2/2cL_1}/L_1^2$$

$$(2.14)$$

$$= \int d^2\boldsymbol{\rho}_0 \, \mathcal{P}_0(\boldsymbol{\rho}_0, \omega_-)e^{i\omega_- L_1/c+i\omega_-|\boldsymbol{\rho}_1-\boldsymbol{\rho}_0|^2/2cL_1}/L_1^2. \quad (2.15)$$

Here, the $\mathcal{P}$ field at $z = 0$ is

$$\mathcal{P}_0(\boldsymbol{\rho}_0, \omega_-) = \int \frac{d\omega_+}{2\pi} \, \mathcal{E}_0(\boldsymbol{\rho}_0, \omega_+ + \omega_-/2) \mathcal{E}_0^*(\boldsymbol{\rho}_0, \omega_+ - \omega_-/2), \qquad (2.16)$$

with no averaging brackets required, because the laser illumination of the $z = 0$ plane is deterministic.

Equation (2.15)—which coincides with the result of applying the Fresnel approximation to Reza $et\ al.$'s Rayleigh-Sommerfeld $\mathcal{P}$-field propagator [9]—is our essential result for paraxial $\mathcal{P}$-field propagation over a distance L_1. It shows that the field emerging from a diffuser that imposes complete spatial incoherence at the optical frequency, but is smooth at the modulation frequency, leads to paraxial $\mathcal{P}$-field propagation at frequency ω_- over a distance L_1 that is governed by a modified version of the $\mathcal{E}$-field's Fresnel-diffraction formula, viz., one in which the exponent's optical frequency in the $\mathcal{E}$-field Fresnel formula is replaced by the $\mathcal{P}$ field's modulation frequency and the $\mathcal{E}$-field formula's $\omega_0/i2\pi cL_1$ factor is replaced by the $\mathcal{P}$ field's $1/L_1^2$ factor. The physical implication of this result is illustrated in the double-slit configurations shown in Fig. 2-2. By inverse Fourier transformation of Eq. (2.15), we see that irradiance propagation from the diffuser at $z = 0$ to the $z = L_1$ plane is governed by

$$\langle I_1(\boldsymbol{\rho}_1, t)\rangle = \int d^2\boldsymbol{\rho}_0 \, I_0(\boldsymbol{\rho}_0, t - L_1/c - |\boldsymbol{\rho}_1 - \boldsymbol{\rho}_0|^2/2cL_1)/L_1^2, \qquad (2.17)$$

which has the following pleasing physical interpretation: Paraxial propagation of the diffuser-averaged STA irradiance from the diffuser's output to the $z = L_1$ presumes that

$$\frac{\exp\left[i\omega\sqrt{L_1^2 + |\boldsymbol{\rho}_1 - \boldsymbol{\rho}_0|^2}/c\right]}{\sqrt{L_1^2 + |\boldsymbol{\rho}_1 - \boldsymbol{\rho}_0|^2}} \approx \frac{\exp(i\omega L_1/c + i\omega|\boldsymbol{\rho}_1 - \boldsymbol{\rho}_0|^2/2cL_1)}{L_1}, \text{ for } |\omega| \leq \Delta\omega$$

$$(2.18)$$

can be employed, and results in $\langle I_1(\boldsymbol{\rho}_1, t)\rangle$ being governed by the paraxial form of geometric optics, viz., the differential contribution of $I_0(\boldsymbol{\rho}_0, t)$ to $\langle I_1(\boldsymbol{\rho}_1, t)\rangle$ is time delayed by $L_1/c + |\boldsymbol{\rho}_1 - \boldsymbol{\rho}_0|^2/2cL_1$ and attenuated by the inverse-square-law factor

$1/L_1^2$.

Paralleling the previous development, it is now easy to show that

$$\mathcal{P}_2(\boldsymbol{\rho}_2, \omega_-) \equiv \int \frac{\mathrm{d}\omega_+}{2\pi} \langle \mathcal{E}_2(\boldsymbol{\rho}_2, \omega_+ + \omega_-/2) \mathcal{E}_2^*(\boldsymbol{\rho}_2, \omega_+ - \omega_-/2) \rangle \tag{2.19}$$

$$= \int \mathrm{d}^2\boldsymbol{\rho}_1 \, \mathcal{P}_1(\boldsymbol{\rho}_1, \omega_-) T(\boldsymbol{\rho}_1) \exp(i\omega_- L_2/c + i\omega_-|\boldsymbol{\rho}_2 - \boldsymbol{\rho}_1|^2/2cL_2)/L_2^2, \tag{2.20}$$

where the averaging brackets in Eq. (2.19) represent averaging over the $h_0(\boldsymbol{\rho}_0)$ *and* the $h_1(\boldsymbol{\rho}_1)$ ensembles. Combining this result with what we have already obtained for relating $\mathcal{P}_1(\boldsymbol{\rho}_1, \omega_-)$ to $\mathcal{P}_0(\boldsymbol{\rho}_0, \omega_-)$ we get

$$\mathcal{P}_2(\boldsymbol{\rho}_2, \omega_-) = \int \mathrm{d}^2\boldsymbol{\rho}_1 \left(\int \mathrm{d}^2\boldsymbol{\rho}_0 \, \mathcal{P}_0(\boldsymbol{\rho}_0, \omega_-) \exp(i\omega_- L_1/c + i\omega_-|\boldsymbol{\rho}_1 - \boldsymbol{\rho}_0|^2/2cL_1)/L_1^2 \right)$$

$$\times T(\boldsymbol{\rho}_1) \exp(i\omega_- L_2/c + i\omega_-|\boldsymbol{\rho}_2 - \boldsymbol{\rho}_1|^2/2cL_2)/L_2^2. \tag{2.21}$$

Before continuing, it is crucial to note the behavior of $\mathcal{P}_2(\boldsymbol{\rho}_2, 0)$. From Eq. (2.21) we immediately find that

$$\mathcal{P}_2(\boldsymbol{\rho}_2, 0) = \int \mathrm{d}^2\boldsymbol{\rho}_1 \, T(\boldsymbol{\rho}_1) \int \mathrm{d}^2\boldsymbol{\rho}_0 \, \mathcal{P}_0(\boldsymbol{\rho}_0, 0)/(L_1 L_2)^2, \tag{2.22}$$

indicating that there is *no* spatial information about $T(\boldsymbol{\rho}_1)$ available in $\mathcal{P}_2(\boldsymbol{\rho}_2, 0)$. This behavior is a consequence of using the paraxial approximation. Going beyond the paraxial-propagation regime—to Rayleigh-Sommerfeld diffraction—will yield a $\mathcal{P}_2(\boldsymbol{\rho}_2, 0)$ containing *some* spatial information about $T(\boldsymbol{\rho}_1)$, but the inverse problem for recovering $T(\boldsymbol{\rho}_1)$ from $\mathcal{P}_2(\boldsymbol{\rho}_2, 0)$ will still be poorly conditioned in the Fig. 2-1 configuration. This behavior has been seen by Xu *et al.* [11] and Thrampoulidis *et al.* [12] in their work on NLoS active imaging with pulsed illumination, in which occlusion-aided operation was needed to obtain useful albedo reconstructions when transient behavior was ignored.
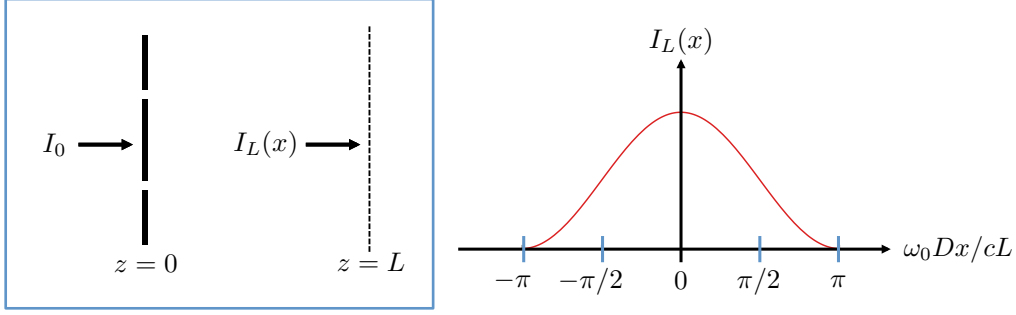
(a) Double-slit diffraction.
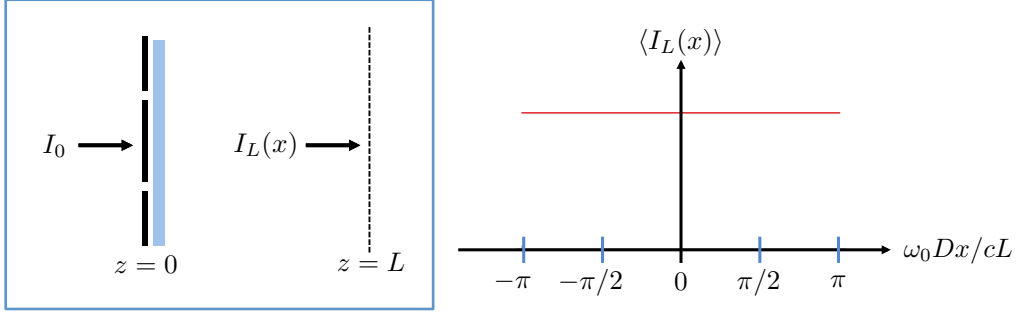
(b) Diffuser eliminates fringes.
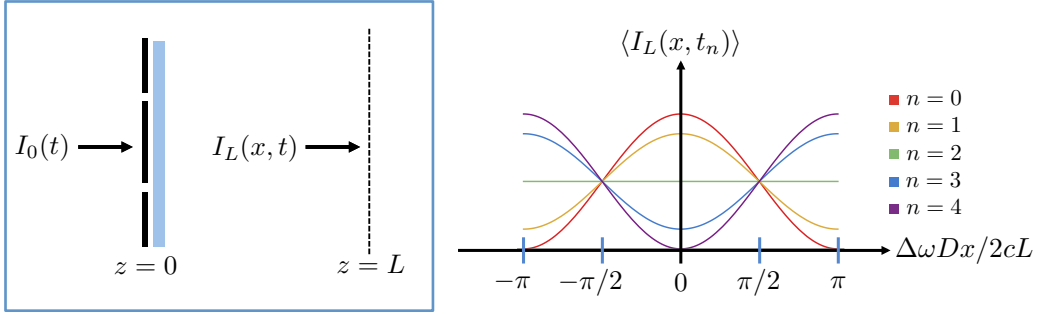
(c) Modulated fringes emerge when illumination is modulated.

Figure 2-2: Illustration of $\mathcal{P}$-field double-slit diffraction in a simplified geometry with one transverse dimension (x) and one longitudinal dimension (z). (a) Illuminating a double-slit screen (slit widths $= d$, slit spacing $D \gg d$) at $z = 0$ with a normally-incident, monochromatic (frequency ω_0) plane wave of irradiance I_0 produces a fringe-patterned irradiance, $I_L(x) \propto I_0[1 + \cos(\omega_0 Dx/cL)]$, in the $z = L$ plane. (b) Placing a diffuser immediately behind the double-slit screen in the setup from (a) results in there being no fringe pattern in the diffuser-averaged irradiance, $\langle I_L(x) \rangle$. (c) Illuminating the screen-plus-diffuser setup from (b) with a single-sideband modulated (at frequency $\Delta\omega \ll \omega_0$), normally-incident plane wave with STA irradiance $I_0(t) = \mathcal{P}_0[1 + \cos(\Delta\omega t)]$ produces a $z = 0_+$ plane $\mathcal{P}$ field $\mathcal{P}_0(x, \omega_-) = \pi\mathcal{P}_0[\delta(\omega_- + \Delta\omega) + 2\delta(\omega_-) + \delta(\omega_- - \Delta\omega)]P(x)$, where $P(x)$ is the double-slit screen's transmissivity pattern. Propagating this $\mathcal{P}$ field to the $z = L$ plane produces the time-varying fringe pattern, $\langle I_L(x, t) \rangle \propto \mathcal{P}_0[1 + \cos[\Delta\omega(t - L/c)] \cos[\Delta\omega Dx/2cL]]$, in the diffuser-averaged STA irradiance, where we have assumed $\Delta\omega D^2/8cL \ll 1$ and $\Delta\omega x^2/2cL \ll 1$. The five lines in (c) show $\langle I_L(x, t_n) \rangle$ for $t_n = \pi n/4\Delta\omega$ with $n = 0, 1, 2, 3, 4$ and $\cos(\Delta\omega L/c) = 1$.

28

2.3 $T(\boldsymbol{\rho}_1)$ Reconstruction in the Paraxial Regime $\mathcal{P}$-Field Formalism

Equation (2.21) shows that the intensity transmission pattern, $T(\boldsymbol{\rho}_1)$, we wish to reconstruct is illuminated by $\mathcal{P}_1(\boldsymbol{\rho}_1, \omega_-)$, the $\mathcal{P}$ field that results from propagation of the laser illumination's $\mathcal{P}_0(\boldsymbol{\rho}_0, \omega_-)$ from $z = 0$ to $z = L_1$. After transmission through $T(\boldsymbol{\rho}_1)$ and the diffuser $h_1(\boldsymbol{\rho}_1)$, $\mathcal{P}$-field propagation from to $z = L_1 + L_2$ results in $\mathcal{P}_2(\boldsymbol{\rho}_2, \omega_-)$, which encounters another diffuser. Because that last diffuser will render the field emerging from it spatially incoherent, we will use the conventional thin-lens imaging system, shown in Fig. 2-3, to gather the data needed to reconstruct $T(\boldsymbol{\rho}_1)$.

Let $E_2'(\boldsymbol{\rho}_2, t)$ be the baseband, complex field envelope emerging from the diffuser in the $z = L_1 + L_2$ plane, and let $\mathcal{E}_2'(\boldsymbol{\rho}_2, \omega)$ be its time-domain Fourier transform. After Fresnel propagation from $z = L_1 + L_2$ to $z = L_1 + L_2 + L_3$, propagation through the diameter-D circular-pupil, focal-length-f thin lens, and Fresnel propagation over an additional L_{im} distance where $1/f = 1/L_3 + 1/L_{\text{im}}$, the resulting image-plane field $E_{\text{im}}(\boldsymbol{\rho}, t)$ has time-domain Fourier transform given by

$$
\mathcal{E}_{\text{im}}(\boldsymbol{\rho}_{\text{im}}, \omega) = \int\limits_{|\boldsymbol{\rho}_3| \leq D/2} \mathrm{d}^2\boldsymbol{\rho}_3 \, \frac{e^{i(\omega_0+\omega)L_{\text{im}}/c + i(\omega_0+\omega)|\boldsymbol{\rho}_{\text{im}} - \boldsymbol{\rho}_3|^2/2cL_{\text{im}} - i(\omega_0+\omega)|\boldsymbol{\rho}_3|^2/2cf}}{i\lambda_0 L_{\text{im}}}
$$

$$
\times \int \mathrm{d}^2\boldsymbol{\rho}_2 \, \mathcal{E}_2'(\boldsymbol{\rho}_2, \omega) \frac{e^{i(\omega_0+\omega)L_3/c + i(\omega_0+\omega)|\boldsymbol{\rho}_3 - \boldsymbol{\rho}_2|^2/2cL_3}}{i\lambda_0 L_3} \tag{2.23}
$$

$$
= e^{i(\omega_0+\omega)|\boldsymbol{\rho}_{\text{im}}|^2/2cL_{\text{im}}} \int \mathrm{d}^2\boldsymbol{\rho}_2 \, \mathcal{E}_2'(\boldsymbol{\rho}_2, \omega) \frac{e^{i(\omega_0+\omega)(L_3+L_{\text{im}})/c + i(\omega_0+\omega)|\boldsymbol{\rho}_2|^2/2cL_3}}{i\lambda_0 L_3}
$$

$$
\times \int\limits_{|\boldsymbol{\rho}_3| \leq D/2} \mathrm{d}^2\boldsymbol{\rho}_3 \, \frac{e^{-i(\omega+\omega_0)\boldsymbol{\rho}_3 \cdot (\boldsymbol{\rho}_2/L_3 + \boldsymbol{\rho}_{\text{im}}/L_{\text{im}})/c}}{i\lambda_0 L_{\text{im}}}. \tag{2.24}
$$

Performing the integration over $\boldsymbol{\rho}_3$ results in

$$
\begin{aligned}
\mathcal{E}_{\mathrm{im}}(\boldsymbol{\rho}_{\mathrm{im}}, \omega) = {} & e^{i(\omega_0+\omega)|\boldsymbol{\rho}_{\mathrm{im}}|^2/2cL_{\mathrm{im}}} \int \mathrm{d}^2\boldsymbol{\rho}_2 \, \mathcal{E}'_2(\boldsymbol{\rho}_2, \omega) \frac{e^{i(\omega_0+\omega)(L_3+L_{\mathrm{im}})/c + i(\omega_0+\omega)|\boldsymbol{\rho}_2|^2/2cL_3}}{-\lambda_0^2 L_3 L_{\mathrm{im}}} \\
& \times \frac{\pi D^2}{4} \frac{J_1\left(\frac{\pi D}{\lambda_0}\left|\frac{\boldsymbol{\rho}_2}{L_3} + \frac{\boldsymbol{\rho}_{\mathrm{im}}}{L_{\mathrm{im}}}\right|\right)}{\frac{\pi D}{2\lambda_0}\left|\frac{\boldsymbol{\rho}_2}{L_3} + \frac{\boldsymbol{\rho}_{\mathrm{im}}}{L_{\mathrm{im}}}\right|},
\end{aligned}
\tag{2.25}
$$

where $J_1(\cdot)$ is the first-order Bessel function of the first kind, and we have used $\pi D/\lambda_0$ in lieu of $(\omega_0+\omega)D/2c$ in the Airy pattern because $\Delta\omega \ll \omega_0$.
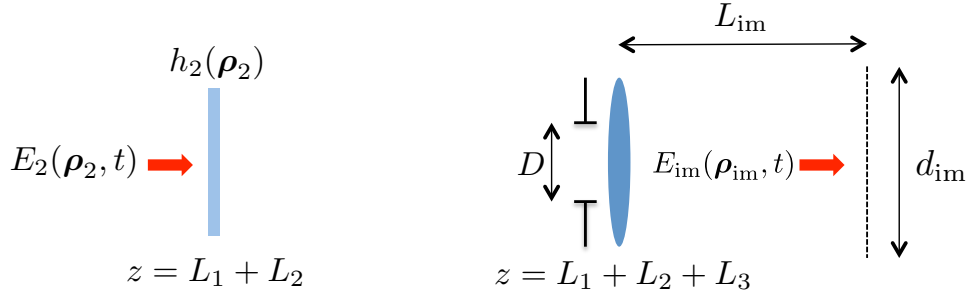
Figure 2-3: Thin-lens imaging setup. A focal-length-f thin lens casts an inverted image of the intensity pattern that emerges from the diffuser at $z = L_1 + L_2$. The image is located in the plane—shown as a black dashed line—a distance L_{im} behind the lens, where $1/f = 1/L_3 + 1/L_{\mathrm{im}}$. We imagine that the STA irradiance at this plane will be detected by a detector array of diameter d_{im}.

The presence of the diffuser $h_2(\boldsymbol{\rho}_2)$ makes

$$
\langle \mathcal{E}'_2(\boldsymbol{\rho}_2, \omega)\mathcal{E}'^*_2(\boldsymbol{\rho}'_2, \omega')\rangle \approx \lambda_0^2 \langle \mathcal{E}_2(\boldsymbol{\rho}_2, \omega)\mathcal{E}^*_2(\boldsymbol{\rho}_2, \omega')\rangle \delta(\boldsymbol{\rho}_2 - \boldsymbol{\rho}'_2),
\tag{2.26}
$$

which together with Eq. (2.25) yields

$$
\begin{aligned}
\mathcal{P}_{\mathrm{im}}(\boldsymbol{\rho}_{\mathrm{im}}, \omega_-) = {} & \int \mathrm{d}^2\boldsymbol{\rho}_2 \, \mathcal{P}_2(\boldsymbol{\rho}_2, \omega_-) e^{i\omega_-(L_3+L_{\mathrm{im}})/c + i\omega_-|\boldsymbol{\rho}_2|^2/2cL_3 + i\omega_-|\boldsymbol{\rho}_{\mathrm{im}}|^2/2cL_{\mathrm{im}}} \\
& \times \left[\frac{\pi D^2}{4\lambda_0 L_3 L_{\mathrm{im}}} \frac{J_1\left(\frac{\pi D}{\lambda_0}\left|\frac{\boldsymbol{\rho}_2}{L_3} + \frac{\boldsymbol{\rho}_{\mathrm{im}}}{L_{\mathrm{im}}}\right|\right)}{\frac{\pi D}{2\lambda_0}\left|\frac{\boldsymbol{\rho}_2}{L_3} + \frac{\boldsymbol{\rho}_{\mathrm{im}}}{L_{\mathrm{im}}}\right|} \right]^2.
\end{aligned}
\tag{2.27}
$$

and hence

$$\langle I_{\text{im}}(\boldsymbol{\rho}_{\text{im}}, t) \rangle = \int d^2\boldsymbol{\rho}_2 \, \langle I_2(\boldsymbol{\rho}_2, t - (L_3 + L_{\text{im}})/c - |\boldsymbol{\rho}_2|^2/2cL_3 - |\boldsymbol{\rho}_{\text{im}}|^2/2cL_{\text{im}}) \rangle$$

$$\times \left[\frac{\pi D^2}{4\lambda_0 L_3 L_{\text{im}}} \frac{J_1\left(\frac{\pi D}{\lambda_0} \left| \frac{\boldsymbol{\rho}_2}{L_3} + \frac{\boldsymbol{\rho}_{\text{im}}}{L_{\text{im}}} \right| \right)}{\frac{\pi D}{2\lambda_0} \left| \frac{\boldsymbol{\rho}_2}{L_3} + \frac{\boldsymbol{\rho}_{\text{im}}}{L_{\text{im}}} \right|} \right]^2. \tag{2.28}$$

So, by measuring $\langle I_{\text{im}}(\boldsymbol{\rho}_{\text{im}}, t) \rangle$, i.e., the diffuser-averaged, STA, image-plane irradiance, we obtain a $1.22\lambda_0/D$-angular-resolution, image of $\langle I_2(\boldsymbol{\rho}_2, t - (L_3 + L_{\text{im}})/c - |\boldsymbol{\rho}_2|^2/2cL_3 - |\boldsymbol{\rho}_{\text{im}}|^2/2cL_{\text{im}}) \rangle$. From that irradiance image we can then compute a $1.22\lambda_0/D$-angular-resolution image of $\mathcal{P}_2(\boldsymbol{\rho}_2, \omega_-)$ at any modulation frequency of interest.

For reconstructing $T(\boldsymbol{\rho}_1)$, let us suppose that the $z = 0$ illumination is a duration t_0, cosinusoidally-modulated, collimated Gaussian-beam laser field where $\Delta\omega t_0 \gg 1$, i.e.,

$$E_0(\boldsymbol{\rho}_0, t) = \begin{cases} \sqrt{\frac{8P_0}{\pi d^2}} \, e^{-4|\boldsymbol{\rho}_0|^2/d^2} \cos(\Delta\omega t/2), & \text{for } |t| \leq t_0/2, \\ 0, & \text{otherwise,} \end{cases} \tag{2.29}$$

with $P_0 t_0/2$ being the energy illuminating the $z = 0$ plane. This field's STA irradiance is then

$$I_0(\boldsymbol{\rho}_0, t) = \begin{cases} \frac{8P_0}{\pi d^2} e^{-8|\boldsymbol{\rho}_0^2/d^2} \cos^2(\Delta\omega t/2) \\ = \frac{4P_0}{\pi d^2} e^{-8|\boldsymbol{\rho}_0^2/d^2} [1 + \cos(\Delta\omega t)], & \text{for } |t| \leq t_0/2, \\ 0, & \text{otherwise,} \end{cases} \tag{2.30}$$

which leads to

$$\mathcal{P}_0(\boldsymbol{\rho}_0, \omega_-) = \frac{8P_0 t_0}{\pi d^2} e^{-8|\boldsymbol{\rho}_0|^2/d^2}$$

$$\times \left[\frac{\sin(\omega_- t_0/2)}{\omega_- t_0/2} + \frac{\sin[(\omega_- + \Delta\omega)t_0/2]}{(\omega_- + \Delta\omega)t_0} + \frac{\sin[(\omega_- - \Delta\omega)t_0/2]}{(\omega_- - \Delta\omega)t_0} \right], \tag{2.31}$$

31

and hence

$$\mathcal{P}_1(\boldsymbol{\rho}_1, \Delta\omega) \approx \int \mathrm{d}^2\boldsymbol{\rho}_0 \, \frac{4P_0 t_0}{\pi d^2} \, e^{-8|\boldsymbol{\rho}_0|^2/d^2} \frac{\exp(i\Delta\omega L_1/c + i\Delta\omega|\boldsymbol{\rho}_1 - \boldsymbol{\rho}_0|^2/2cL_1)}{L_1^2}, \quad (2.32)$$

because $\Delta\omega t_0 \gg 1$. Although this expression can be evaluated analytically, we shall not bother. We just note that with $\Delta\omega/2\pi \sim 1\,\mathrm{GHz}$, $d \sim 1\,\mathrm{mm}$, and $L_1 \sim 1\,\mathrm{m}$, we have $cL_1/\Delta\omega d^2 \gg 1$ from which it follows that the spatial extent of $\mathcal{P}_1(\boldsymbol{\rho}_1, \Delta\omega)$ will be $\sim cL_1/\Delta\omega d \gg d$. In other words, the effect of the diffuser $h_0(\boldsymbol{\rho}_0)$ is to ensure that a finite, but much larger than diameter-d, region of the $z = L_1$ plane is illuminated by the frequency-$\Delta\omega$ $\mathcal{P}$ field.

To proceed further, assume we have generated the computed image,

$$\tilde{\mathcal{P}}_2(\boldsymbol{\rho}_2, \Delta\omega) \equiv (L_{\mathrm{im}}/L_3)^2 \mathcal{P}_{\mathrm{im}}(-\boldsymbol{\rho}_2 L_{\mathrm{im}}/L_3, \Delta\omega)$$
$$\times \, e^{-i\Delta\omega(L_3 + L_{\mathrm{im}})/c - i\Delta\omega|\boldsymbol{\rho}_2|^2/2cL_3 - i\Delta\omega|\boldsymbol{\rho}_{\mathrm{im}}|^2/2cL_{\mathrm{im}}}, \qquad (2.33)$$

of $\mathcal{P}_2(\boldsymbol{\rho}_2, \Delta\omega)$ from the $\langle I_{\mathrm{im}}(\boldsymbol{\rho}_{\mathrm{im}}, t) \rangle$ measurement. We can computationally invert Eq. (2.20) to obtain a reconstruction of $T(\boldsymbol{\rho}_1)\mathcal{P}_1(\boldsymbol{\rho}_1, \Delta\omega)$ and use our knowledge of $\mathcal{P}_1(\boldsymbol{\rho}_1, \Delta\omega)$ to obtain a $T(\boldsymbol{\rho}_1)$ image. In particular, suppose we measure $\langle I_{\mathrm{im}}(\boldsymbol{\rho}_{\mathrm{im}}, t) \rangle$ for $|\boldsymbol{\rho}_{\mathrm{im}}| \leq d_{\mathrm{im}}/2$, and then define $\tilde{T}(\tilde{\boldsymbol{\rho}}_1)$ by

$$\tilde{T}(\tilde{\boldsymbol{\rho}}_1)|\mathcal{P}_1(\tilde{\boldsymbol{\rho}}_1, \Delta\omega)| = \left| \int\limits_{|\boldsymbol{\rho}_2| \leq D'/2} \mathrm{d}^2\boldsymbol{\rho}_2 \, \tilde{\mathcal{P}}_2(\boldsymbol{\rho}_2, \Delta\omega) \frac{e^{-i\Delta\omega|\boldsymbol{\rho}_2|^2/2cL_2 + i\Delta\omega\boldsymbol{\rho}_2 \cdot \tilde{\boldsymbol{\rho}}_1/cL_2}}{\Delta\lambda^2} \right|, \quad (2.34)$$

where $D' \equiv d_{\mathrm{im}}L_3/L_{\mathrm{im}}$. Neglecting noise, and assuming that the $1.22\lambda_0/D$ angular resolution is sufficient to make

$$\tilde{\mathcal{P}}_2(\boldsymbol{\rho}_2, \Delta\omega) \approx \mathcal{P}_2(\boldsymbol{\rho}_2, \Delta\omega), \qquad (2.35)$$

$\mathrm{Ai}(x)$
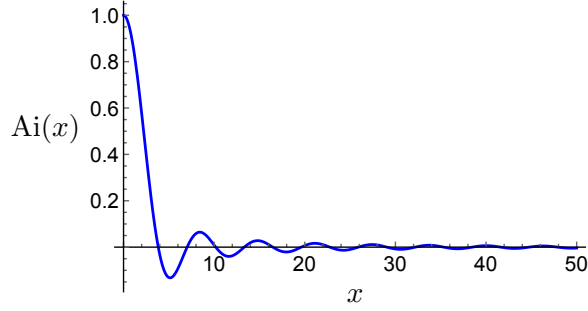
Figure 2-4: The Airy-disk function.

for $|\boldsymbol{\rho}_2| \leq D'/2$, Eq. (2.34) leads to

$$\tilde{T}(\tilde{\boldsymbol{\rho}}_1)|\mathcal{P}_1(\tilde{\boldsymbol{\rho}}_1, \Delta\omega)| = \left| \int \mathrm{d}^2\boldsymbol{\rho}_1\, \mathcal{P}_1(\boldsymbol{\rho}_1, \Delta\omega)T(\boldsymbol{\rho}_1)e^{i\Delta\omega|\boldsymbol{\rho}_1|^2/2cL_2} \right.$$
$$\left. \times \frac{\pi}{4}\left(\frac{D'}{\Delta\lambda L_2}\right)^2 \mathrm{Ai}(\pi D'|\tilde{\boldsymbol{\rho}}_1 - \boldsymbol{\rho}_1|/\Delta\lambda L_2) \right|, \qquad (2.36)$$

where $\mathrm{Ai}(x) \equiv 2J_1(x)/x$ denotes the Airy disk, plotted in Fig 2-4. Thus, over the region in the $z = L_1$ plane wherein $|\mathcal{P}_1(\boldsymbol{\rho}_1, \Delta\omega)|$ has an appreciable value, the $\mathcal{P}$-field imager using cosinusoidal E-field modulation at frequency $\Delta\omega/2$ achieves a spatial resolution of $1.22\Delta\lambda L_2/D'$, where: $\Delta\lambda = 2\pi c/\Delta\omega$; L_2 is the distance from the transparency-containing plane to the plane visible to the sensor; and $D' = d_{\mathrm{im}}L_3/L_{\mathrm{im}}$, with L_3 being the distance from the plane visible to the sensor to the sensor's entrance pupil, L_{im} being the distance from that entrance pupil to the image plane where irradiance measurements are made, and d_{im} being the diameter of the image-plane region over which those measurements are made, as shown in Figs. 2-1 and 2-3.

This is an exciting result, that the $\mathcal{P}$-field framework enables us to use a wave-optical imaging approach to form diffraction-limited reconstructions of targets hidden by diffusers. However, Fig. 2-3 might leave one wondering whether we cannot go a step further and configure our lens to directly image the target plane as if the intervening diffuser were not there at all. With this motivation in mind, we turn our attention to understanding the input-output behavior of the $\mathcal{P}$ field for a variety of lens configurations.

2.4 $\mathcal{P}$-Field Propagation Through Lenses

In this section, we consider the propagation of the $\mathcal{P}$ field through lenses. In particular, we assume thin lenses modeled by quadratic phase shifts. We consider the scenario depicted in Fig. 2-1, and ask how the target plane at $z = L_1$ might be directly interrogated with the help of lenses in the accessible space—$z < 0$ and $z > L_1 + L_2$.

2.4.1 Plane-Wave Focusing
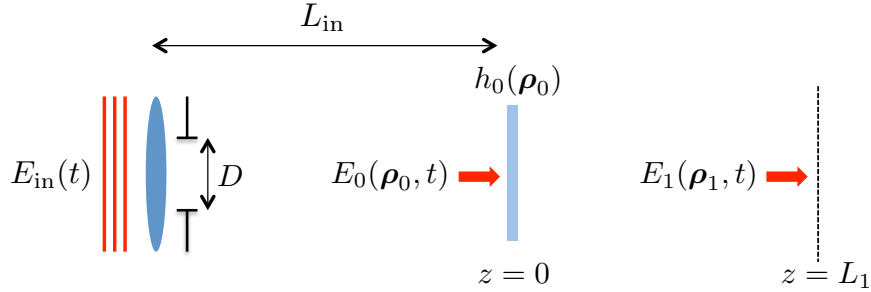
Figure 2-5: Geometry for focusing a plane wave onto a hidden target plane. The lens is taken to have a Gaussian field-transmission aperture $e^{-|\rho|^2/2D^2}$.

First we attempt to focus an infinite plane wave of complex field envelope $E_{\text{in}}(t)$ onto the target plane by means of a focal-length-$f = L_{\text{in}} + L_1$ lens that is set back a distance L_{in} from the first diffuser, as depicted in Fig. 2-5. The temporal-frequency-domain complex field envelope at the first diffuser is given by

$$\mathcal{E}_0(\boldsymbol{\rho}_0, \omega) = \frac{e^{i\frac{\omega_0+\omega}{c}L_{\text{in}}}}{i\lambda_0 L_{\text{in}}} \int d^2\boldsymbol{\rho}_{\text{in}}\, \mathcal{E}_{\text{in}}(\omega) e^{i\frac{\omega_0+\omega}{c}\frac{|\boldsymbol{\rho}_0-\boldsymbol{\rho}_{\text{in}}|^2}{2L_{\text{in}}}} e^{-i\frac{\omega_0+\omega}{c}\frac{|\boldsymbol{\rho}_{\text{in}}|^2}{2f}} e^{-\frac{|\boldsymbol{\rho}_{\text{in}}|^2}{2D^2}}, \qquad (2.37)$$

where $\mathcal{E}_{\text{in}}(\omega)$, the Fourier transform of $E_{\text{in}}(t)$, doesn't depend on $\boldsymbol{\rho}_{\text{in}}$ because the input illumination is an infinite plane wave. Physically, the resolving power of the lens will be limited by a finite aperture diameter, which should appear as limits on this integral. However, for simplicity we assume a Gaussian aperture with $e^{-1/2}$-field-attenuation radius D, which appears as the last term in the integral. The Gaussian model allows us to obtain closed-form results while still capturing the essential physics

of the limitations induced by a physical aperture.[4] Rearranging terms we have

$$\mathcal{E}_0(\boldsymbol{\rho}_0,\omega) = \frac{e^{i\frac{\omega_0+\omega}{c}L_{\text{in}}}}{i\lambda_0 L_{\text{in}}}\mathcal{E}_{\text{in}}(\omega)e^{i\frac{\omega_0+\omega}{c}\frac{|\boldsymbol{\rho}_0|^2}{2L_{\text{in}}}}\int\mathrm{d}^2\boldsymbol{\rho}_{\text{in}}\,e^{-i\frac{\omega_0+\omega}{c}\frac{\boldsymbol{\rho}_0}{L_{\text{in}}}\cdot\boldsymbol{\rho}_{\text{in}}}e^{-i\frac{\omega_0+\omega}{c}\frac{|\boldsymbol{\rho}_{\text{in}}|^2}{2}\left(\frac{1}{f}-\frac{1}{L_{\text{in}}}\right)}e^{-\frac{|\boldsymbol{\rho}_{\text{in}}|^2}{2D^2}}$$

$$(2.38)$$

$$= \frac{e^{i\frac{\omega_0+\omega}{c}L_{\text{in}}}}{i\lambda_0 L_{\text{in}}}\mathcal{E}_{\text{in}}(\omega)e^{i\frac{\omega_0+\omega}{c}\frac{|\boldsymbol{\rho}_0|^2}{2L_{\text{in}}}}\frac{2\pi}{\frac{1}{D^2}-i\frac{f-L_{\text{in}}}{fL_{\text{in}}}\frac{\omega_0+\omega}{c}}e^{-\frac{|\boldsymbol{\rho}_0|^2}{2}\frac{(\omega_0+\omega)^2}{c^2L_{\text{in}}^2}\frac{\frac{1}{D^2}+i\frac{f-L_{\text{in}}}{fL_{\text{in}}}\frac{\omega_0+\omega}{c}}{\frac{1}{D^4}+\left(\frac{f-L_{\text{in}}}{fL_{\text{in}}}\frac{\omega_0+\omega}{c}\right)^2}},$$

$$(2.39)$$

where the integral can be evaluated by treating it as a Fourier transform of a complex-valued Gaussian. To simplify this result, we impose the reasonable assumption that $D\gg\sqrt{\frac{fL_{\text{in}}}{f-L_{\text{in}}}\frac{c}{\omega_0+\omega}}$. For $f=2\,\mathrm{m}$, $L_{\text{in}}=1\,\mathrm{m}$, and $\lambda_0=500\,\mathrm{nm}$ this approximately reduces to $D\gg 0.3\,\mathrm{mm}$, which is eminently reasonable. Using this assumption we find that

$$\mathcal{E}_0(\boldsymbol{\rho}_0,\omega)$$
$$= \frac{e^{i\frac{\omega_0+\omega}{c}L_{\text{in}}}}{i\lambda_0 L_{\text{in}}}\mathcal{E}_{\text{in}}(\omega)e^{i\frac{\omega_0+\omega}{c}\frac{|\boldsymbol{\rho}_0|^2}{2L_{\text{in}}}}\frac{2\pi}{\frac{1}{D^2}-i\frac{f-L_{\text{in}}}{fL_{\text{in}}}\frac{\omega_0+\omega}{c}}e^{-\frac{|\boldsymbol{\rho}_0|^2}{2D^2}\frac{f^2}{(f-L_{\text{in}})^2}}e^{-i\frac{\omega_0+\omega}{c}\frac{f}{L_{\text{in}}(f-L_{\text{in}})}\frac{|\boldsymbol{\rho}_0|^2}{2}},$$

$$(2.40)$$

which ultimately yields

$$\mathcal{P}_0(\boldsymbol{\rho}_0,\omega_-) = \frac{f^2}{(f-L_{\text{in}})^2}e^{i\frac{\omega_-}{c}L_{\text{in}}}\mathcal{P}_{\text{in}}(\omega_-)e^{i\frac{\omega_-|\boldsymbol{\rho}_0|^2}{2c(L_{\text{in}}-f)}}e^{-\frac{|\boldsymbol{\rho}_0|^2}{D^2}\frac{f^2}{(f-L_{\text{in}})^2}}. \qquad (2.41)$$

---

[4]In the absence of the diffuser, a hard-aperture lens would focus the plane wave down to an Airy disk, whereas a Gaussian-aperture lens would result in a Gaussian spot. The spatial extent of the focused spot, in both cases, scales as $\lambda_0 L/D$, where L is the propagation distance and D the aperture diameter. The difference is in the ringing artifacts of the Airy disk, induced by the hard aperture's edge. Thus, for the sake of analyzing resolution limits, the Gaussian model provides a sufficient, simplified alternative.

Using the Fresnel-diffraction formula for $\mathcal{P}$-fields now gives us

$$\mathcal{P}_1(\boldsymbol{\rho}_1, \omega_-) = \frac{e^{i\frac{\omega_-}{c}L_1}}{L_1^2} \int d^2\boldsymbol{\rho}_0 \, \mathcal{P}_0(\boldsymbol{\rho}_0, \omega_-) e^{i\frac{\omega_-}{c}\frac{|\boldsymbol{\rho}_1-\boldsymbol{\rho}_0|^2}{2L_1}} \tag{2.42}$$

$$= \frac{f^2}{(f-L_{\text{in}})^2} \mathcal{P}_{\text{in}}(\omega_-) \frac{e^{i\frac{\omega_-}{c}(L_{\text{in}}+L_1)}}{L_1^2} e^{i\frac{\omega_-}{c}\frac{|\boldsymbol{\rho}_1|^2}{2L_1}}$$

$$\times \int d^2\boldsymbol{\rho}_0 \, e^{-i\frac{\omega_-\boldsymbol{\rho}_1}{cL_1}\cdot\boldsymbol{\rho}_0} e^{-\frac{|\boldsymbol{\rho}_0|^2}{D^2}\frac{f^2}{(f-L_{\text{in}})^2}} e^{i\frac{\omega_-}{c}\frac{|\boldsymbol{\rho}_0|^2}{2}\left(\frac{1}{L_{\text{in}}-f}+\frac{1}{L_1}\right)}. \tag{2.43}$$

By focusing the lens on the $z = L_1$ plane we have $f = L_{\text{in}} + L_1$, which eliminates the final exponential term. The integral that remains evaluates to a Gaussian leaving

$$\mathcal{P}_1(\boldsymbol{\rho}_1, \omega_-) = \pi \frac{D^2}{L_1^2} e^{i\frac{\omega_-}{c}(L_{\text{in}}+L_1)} e^{i\frac{\omega_-}{c}\frac{|\boldsymbol{\rho}_1|^2}{2L_1}} \mathcal{P}_{\text{in}}(\omega_-) e^{-\frac{|\boldsymbol{\rho}_1|^2}{4}\frac{\omega_-^2 D^2}{c^2(L_{\text{in}}+L_1)^2}}. \tag{2.44}$$

Using $f = L_{\text{in}} + L_1$ this result simplifies to

$$\mathcal{P}_1(\boldsymbol{\rho}_1, \omega_-) = \pi \frac{D^2}{L_1^2} e^{i\omega_- f/c} e^{i\omega_-|\boldsymbol{\rho}_1|^2/2cL_1} \mathcal{P}_{\text{in}}(\omega_-) e^{-(\omega_- D/2cf)^2|\boldsymbol{\rho}_1|^2}. \tag{2.45}$$

The implication of this result is that the incident plane wave creates a $\mathcal{P}$-field illumination that is tightly focused by the lens onto a small point—diffraction limited at the modulation wavelength—in the center of the desired plane. From the perspective of phasor-field imaging, this enables us to raster scan the target as if the initial diffuser weren't present. Having said that, although this enables the $\mathcal{P}$ field at a given modulation frequency to be spatially focused, it does *not* focus the optical power, which is still spread out by the diffuser, as verified by Reza *et al.* [13]. Since the $\mathcal{P}$ field is ultimately supported by the optical field, its peak strength, like the STA irradiance's, is still subject to inverse-square falloff, even in the presence of the lens. That Eq. (2.45) suggests otherwise—i.e., that the inverse-square falloff can be compensated for by increasing D—is only a function of the fact that we have assumed infinite-plane-wave illumination, and thus by increasing the size of the aperture D we allow more and more power to pass through the lens, proportional to the area of the aperture. Correcting for this scaling it is clear that the peak $\mathcal{P}$ field follows inverse-square falloff relative to the input power, regardless of the aperture diameter,

i.e., how tightly the $\mathcal{P}$ field is confined in the target plane.

2.4.2   Lens-Aided Bucket Detection
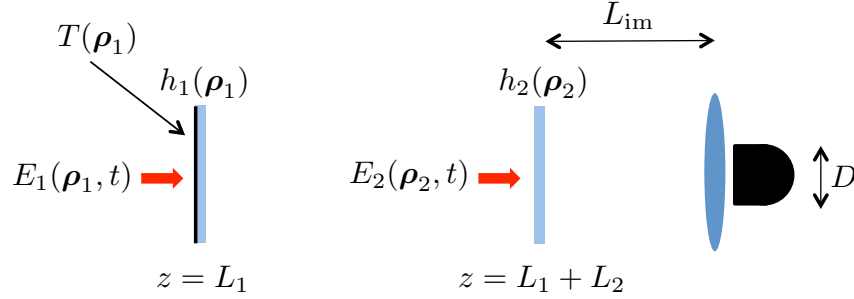
Figure 2-6: Geometry for detecting the $\mathcal{P}$ field from a small region on a hidden target plane by means of a lens and bucket detection. The detector is assumed to have an active region $|\boldsymbol{\rho}| \leq D/2$.

The dual of our focusing result is also readily obtained. Considering again the same transmissive geometry, we examine the effect of placing a lens of focal length $f = L_2 + L_{\text{im}}$ at a distance L_{im} beyond the final diffuser, followed by a bucket detector, as depicted in Fig. 2-6. Paralleling what we did in Sec. 2.3 and ignoring, for now, the finite lens aperture, we have that

$$
\begin{aligned}
&\mathcal{P}_{\text{im}}\left(\boldsymbol{\rho}_{\text{im}}, \omega_-\right) \\
&= \frac{e^{i\frac{\omega_-}{c}(L_2+L_{\text{im}})}}{L_2^2 L_{\text{im}}^2} e^{-i\frac{\omega_-}{c}\frac{|\boldsymbol{\rho}_{\text{im}}|^2}{2f}} \int \mathrm{d}^2\boldsymbol{\rho}_2 \, e^{i\frac{\omega_-}{c}\frac{|\boldsymbol{\rho}_{\text{im}}-\boldsymbol{\rho}_2|^2}{2L_{\text{im}}}} \int \mathrm{d}^2\boldsymbol{\rho}_1 \, e^{i\frac{\omega_-}{c}\frac{|\boldsymbol{\rho}_2-\boldsymbol{\rho}_1|^2}{2L_2}} T(\boldsymbol{\rho}_1)\mathcal{P}_1(\boldsymbol{\rho}_1, \omega_-)
\end{aligned}
$$

(2.46)

$$
\begin{aligned}
&= \frac{e^{i\frac{\omega_-}{c}(L_2+L_{\text{im}})}}{L_2^2 L_{\text{im}}^2} e^{i\frac{\omega_-}{c}\frac{|\boldsymbol{\rho}_{\text{im}}|^2}{2}\left(\frac{1}{L_{\text{im}}}-\frac{1}{f}\right)} \int \mathrm{d}^2\boldsymbol{\rho}_1 \, \mathcal{P}_1(\boldsymbol{\rho}_1, \omega_-)T(\boldsymbol{\rho}_1)e^{i\frac{\omega_-}{c}\frac{|\boldsymbol{\rho}_1|^2}{2L_2}} \\
&\quad \times \int \mathrm{d}^2\boldsymbol{\rho}_2 \, e^{-i\frac{\omega_-}{c}\left(\frac{\boldsymbol{\rho}_{\text{im}}}{L_{\text{im}}}+\frac{\boldsymbol{\rho}_1}{L_2}\right)\cdot\boldsymbol{\rho}_2} e^{i\frac{\omega_-}{c}\frac{|\boldsymbol{\rho}_2|^2}{2}\left(\frac{1}{L_{\text{im}}}+\frac{1}{L_2}\right)}
\end{aligned}
$$

(2.47)

$$
\begin{aligned}
&= i\frac{2\pi c}{\omega_-} \frac{e^{i\frac{\omega_-}{c}(L_2+L_{\text{im}})}}{L_2 L_{\text{im}}(L_2+L_{\text{im}})} e^{i\frac{\omega_-}{c}\frac{|\boldsymbol{\rho}_{\text{im}}|^2}{2}\left(\frac{1}{L_{\text{im}}+L_2}-\frac{1}{f}\right)} \\
&\quad \times \int \mathrm{d}^2\boldsymbol{\rho}_1 \, \mathcal{P}_1(\boldsymbol{\rho}_1, \omega_-)T(\boldsymbol{\rho}_1)e^{i\frac{\omega_-}{c(L_2+L_{\text{im}})}(|\boldsymbol{\rho}_1|^2/2-\boldsymbol{\rho}_{\text{im}}\cdot\boldsymbol{\rho}_1)}.
\end{aligned}
$$

(2.48)

Taking the lens to be focused on the target plane, $f = L_2 + L_{\text{im}}$, the $\boldsymbol{\rho}_{\text{im}}$-dependent

37

leading exponential term vanishes. Integrating over the $z = L_1 + L_2 + L_\mathrm{im}$ plane, representing bucket detection, constrained by a diameter D representing the smaller of either the lens's aperture or the detector's active region leaves us with

$$
\int\limits_{|\boldsymbol{\rho}_\mathrm{im}|\leq D/2} \mathrm{d}^2\boldsymbol{\rho}_\mathrm{im}\, \mathcal{P}_\mathrm{im}(\boldsymbol{\rho}_\mathrm{im}, \omega_-)
$$

$$
= i\frac{2\pi c}{\omega_-}\frac{e^{i\frac{\omega_-}{c}(L_2+L_\mathrm{im})}}{L_2 L_\mathrm{im}(L_2+L_\mathrm{im})}\int \mathrm{d}^2\boldsymbol{\rho}_1\, \mathcal{P}_1(\boldsymbol{\rho}_1, \omega_-)T(\boldsymbol{\rho}_1)e^{i\frac{\omega_-|\boldsymbol{\rho}_1|^2}{2c(L_2+L_\mathrm{im})}}\frac{\pi D^2}{4}\frac{J_1\left(\frac{D\omega_-}{2c(L_2+L_\mathrm{im})}|\boldsymbol{\rho}_1|\right)}{\frac{D\omega_-}{4c(L_2+L_\mathrm{im})}|\boldsymbol{\rho}_1|}.
$$

$$(2.49)$$

Using $f = L_2 + L_\mathrm{im}$, denoting the active area of the detector by $A \equiv \pi D^2/4$, and denoting the Airy disk by $\mathrm{Ai}(x) \equiv 2J_1(x)/x$, this result simplifies to

$$
\int\limits_{|\boldsymbol{\rho}_\mathrm{im}|\leq D/2} \mathrm{d}^2\boldsymbol{\rho}_\mathrm{im}\, \mathcal{P}_\mathrm{im}(\boldsymbol{\rho}_\mathrm{im}, \omega_-) = i\frac{2\pi c}{\omega_-}\frac{A}{L_2 L_\mathrm{im}f}e^{i\omega_- f/c}
$$

$$
\times \int \mathrm{d}^2\boldsymbol{\rho}_1\, \mathcal{P}_1(\boldsymbol{\rho}_1, \omega_-)T(\boldsymbol{\rho}_1)e^{i\omega_-|\boldsymbol{\rho}_1|^2/2cf}\mathrm{Ai}((\omega_- D/2cf)|\boldsymbol{\rho}_1|). \qquad (2.50)
$$

Ignoring inessential phase and scaling terms, the result, as expected, is a detection of the center of the target plane's $\mathcal{P}$-field weighted by the modulation wavelength's Airy disk. Taking this result together with the previous result for an initial, focusing lens, one could imagine adjusting the focusing paths of both lenses via galvos, thus creating the NLoS $\mathcal{P}$-field analogy of a scanning confocal microscope. The bucket detector in Fig. 2-6 might take the physical form of a large single-element detector, or a small single-element detector coupled to a large collimator. By the Fourier transform's linearity, spatial integration of the diffuser-averaged STA irradiance corresponds to spatial integration of the $\mathcal{P}$ field. However, this bucket-detector scenario seems somewhat contrived, physically speaking, and is presented here primarily for theoretical interest as it is the mathematical dual of the focusing case. In practice, high-bandwidth single-element detectors have very small active areas, and if we wanted to use such detectors in conjunction with optics to probe a small region of the target plane, why not configure our optics for imaging? In fact, as one might hope,

the use of lenses with $\mathcal{P}$ fields allows us to go a step further than these two scenarios to project arbitrary $\mathcal{P}$-field patterns onto the target plane and directly image its outgoing $\mathcal{P}$ field.

2.4.3   Lens Primitive for Projecting and Imaging Cases

$$E_0(\boldsymbol{\rho}_0, t) \to \quad h_0(\boldsymbol{\rho}_0) \qquad D \quad \qquad \to E_2(\boldsymbol{\rho}_2, t)$$

$$z = 0 \qquad\qquad z = L_1 \qquad\qquad z = L_1 + L_2$$
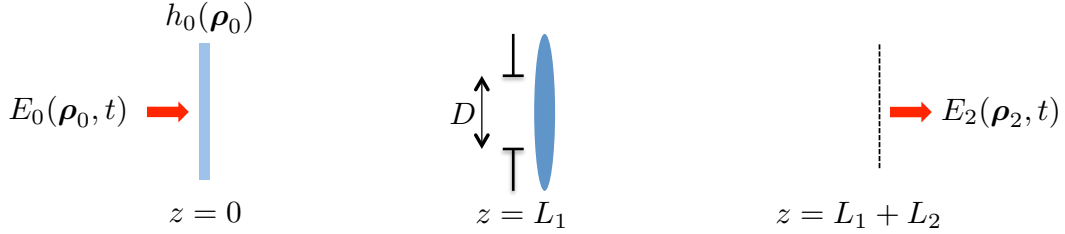
Figure 2-7: Fresnel propagation with an intervening lens.

In this section we derive a $\mathcal{P}$-field propagation primitive for Fresnel propagation with an intervening focal-length-f thin lens limited by a Gaussian aperture of $e^{-1/2}$-field-attenuation radius D, as depicted in Fig. 2-7. This will prove useful for both the projection and imaging cases that follow. We have that

$$
\begin{aligned}
\mathcal{E}_2(\boldsymbol{\rho}_2, \omega) = \quad & \frac{e^{i\frac{\omega_0+\omega}{c}(L_1+L_2)}}{-\lambda_0^2 L_1 L_2} \int \mathrm{d}^2\boldsymbol{\rho}_1\, e^{i\frac{\omega_0+\omega}{c}\frac{|\boldsymbol{\rho}_2-\boldsymbol{\rho}_1|^2}{2L_2}} e^{-i\frac{\omega_0+\omega}{c}\frac{|\boldsymbol{\rho}_1|^2}{2f}} e^{-\frac{|\boldsymbol{\rho}_1|^2}{2D^2}} \\
& \times \int \mathrm{d}^2\boldsymbol{\rho}_0\, \mathcal{E}_0(\boldsymbol{\rho}_0, \omega) e^{i\frac{\omega_0+\omega}{c}\frac{|\boldsymbol{\rho}_1-\boldsymbol{\rho}_0|^2}{2L_1}} e^{i\frac{\omega_0+\omega}{c}h_0(\boldsymbol{\rho}_0)} \quad (2.51)
\end{aligned}
$$

$$
\begin{aligned}
= \quad & \frac{e^{i\frac{\omega_0+\omega}{c}(L_1+L_2)}}{-\lambda_0^2 L_1 L_2} e^{i\frac{\omega_0+\omega}{c}\frac{|\boldsymbol{\rho}_2|^2}{2L_2}} \int \mathrm{d}^2\boldsymbol{\rho}_0\, \mathcal{E}_0(\boldsymbol{\rho}_0, \omega) e^{i\frac{\omega_0+\omega}{c}\frac{|\boldsymbol{\rho}_0|^2}{2L_1}} e^{i\frac{\omega_0+\omega}{c}h_0(\boldsymbol{\rho}_0)} \\
& \times \int \mathrm{d}^2\boldsymbol{\rho}_1\, e^{-i\frac{\omega_0+\omega}{c}\boldsymbol{\rho}_1\cdot\left(\frac{\boldsymbol{\rho}_0}{L_1}+\frac{\boldsymbol{\rho}_2}{L_2}\right)} e^{i\frac{\omega_0+\omega}{c}\frac{|\boldsymbol{\rho}_1|^2}{2}\left(\frac{1}{L_1}+\frac{1}{L_2}-\frac{1}{f}\right)} e^{-\frac{|\boldsymbol{\rho}_1|^2}{2D^2}} \quad (2.52)
\end{aligned}
$$

$$
\begin{aligned}
= \quad & \frac{e^{i\frac{\omega_0+\omega}{c}(L_1+L_2)}}{-\lambda_0^2 L_1 L_2} e^{i\frac{\omega_0+\omega}{c}\frac{|\boldsymbol{\rho}_2|^2}{2L_2}} \int \mathrm{d}^2\boldsymbol{\rho}_0\, \mathcal{E}_0(\boldsymbol{\rho}_0, \omega) e^{i\frac{\omega_0+\omega}{c}\frac{|\boldsymbol{\rho}_0|^2}{2L_1}} e^{i\frac{\omega_0+\omega}{c}h_0(\boldsymbol{\rho}_0)} \\
& \times \frac{2\pi}{\frac{1}{D^2}-i\frac{1}{\Pi(f,L_1,L_2)}\frac{\omega_0+\omega}{c}} e^{-\frac{\left|\frac{\boldsymbol{\rho}_0}{L_1}+\frac{\boldsymbol{\rho}_2}{L_2}\right|^2}{2}\frac{(\omega_0+\omega)^2}{c^2}\frac{\frac{1}{D^2}+i\frac{1}{\Pi(f,L_1,L_2)}\frac{\omega_0+\omega}{c}}{\frac{1}{D^4}+\left(\frac{1}{\Pi(f,L_1,L_2)}\frac{\omega_0+\omega}{c}\right)^2}}, \quad (2.53)
\end{aligned}
$$

where

$$
\Pi(f, L_1, L_2) \equiv \frac{1}{1/L_1 + 1/L_2 - 1/f} = \frac{f L_1 L_2}{f(L_1+L_2) - L_1 L_2} \quad (2.54)
$$

Similar to what was done before for plane-wave focusing, we assume
$D \gg \sqrt{\Pi(f, L_1, L_2)\frac{c}{\omega_0 + \omega}}$, which is satisfied in both the projecting and imaging scenarios to follow for parameter values similar to those chosen for the focusing case. With this assumption we have that

$$
\begin{aligned}
\mathcal{E}_2(\boldsymbol{\rho}_2, \omega) =& \frac{e^{i\frac{\omega_0+\omega}{c}(L_1+L_2)}}{-\lambda_0^2 L_1 L_2} e^{i\frac{\omega_0+\omega}{c}\frac{|\boldsymbol{\rho}_2|^2}{2L_2}} \int \mathrm{d}^2\boldsymbol{\rho}_0\, \mathcal{E}_0(\boldsymbol{\rho}_0, \omega) e^{i\frac{\omega_0+\omega}{c}\frac{|\boldsymbol{\rho}_0|^2}{2L_1}} e^{i\frac{\omega_0+\omega}{c}h_0(\boldsymbol{\rho}_0)} \\
& \times \frac{2\pi}{\frac{1}{D^2} - i\frac{1}{\Pi(f,L_1,L_2)}\frac{\omega_0+\omega}{c}} e^{-\frac{\left|\frac{\boldsymbol{\rho}_0}{L_1}+\frac{\boldsymbol{\rho}_2}{L_2}\right|^2}{2D^2}\Pi^2(f,L_1,L_2)} \\
& \times e^{-i\frac{\omega_0+\omega}{c}\frac{\left|\frac{\boldsymbol{\rho}_0}{L_1}+\frac{\boldsymbol{\rho}_2}{L_2}\right|^2}{2}\Pi(f,L_1,L_2)},
\end{aligned} \tag{2.55}
$$

from which it follows that

$$
\begin{aligned}
\mathcal{P}_2(\boldsymbol{\rho}_2, \omega_-) =& \left(\frac{\Pi(f, L_1, L_2)}{L_1 L_2}\right)^2 e^{i\frac{\omega_-}{c}(L_1+L_2)} e^{i\frac{\omega_-}{c}\frac{|\boldsymbol{\rho}_2|^2}{2L_2}} \\
& \times \int \mathrm{d}^2\boldsymbol{\rho}_0\, \mathcal{P}_0(\boldsymbol{\rho}_0, \omega_-) e^{i\frac{\omega_-}{c}\frac{|\boldsymbol{\rho}_0|^2}{2L_1}} e^{-\frac{\left|\frac{\boldsymbol{\rho}_0}{L_1}+\frac{\boldsymbol{\rho}_2}{L_2}\right|^2}{D^2}\Pi^2(f,L_1,L_2)} \\
& \times e^{-i\frac{\omega_-}{c}\frac{\left|\frac{\boldsymbol{\rho}_0}{L_1}+\frac{\boldsymbol{\rho}_2}{L_2}\right|^2}{2}\Pi(f,L_1,L_2)} \\
=& \left(\frac{\Pi(f, L_1, L_2)}{L_1 L_2}\right)^2 e^{i\frac{\omega_-}{c}(L_1+L_2)} e^{i\frac{\omega_-}{c}\frac{|\boldsymbol{\rho}_2|^2}{2L_2}\left(1-\frac{\Pi(f,L_1,L_2)}{L_2}\right)} \\
& \times \int \mathrm{d}^2\boldsymbol{\rho}_0\, \mathcal{P}_0(\boldsymbol{\rho}_0, \omega_-) e^{i\frac{\omega_-}{c}\frac{|\boldsymbol{\rho}_0|^2}{2L_1}\left(1-\frac{\Pi(f,L_1,L_2)}{L_1}\right)} e^{-\frac{\left|\frac{\boldsymbol{\rho}_0}{L_1}+\frac{\boldsymbol{\rho}_2}{L_2}\right|^2}{D^2}\Pi^2(f,L_1,L_2)} \\
& \times e^{-i\frac{\omega_-}{c}\frac{\Pi(f,L_1,L_2)}{L_1 L_2}\boldsymbol{\rho}_0\cdot\boldsymbol{\rho}_2}.
\end{aligned}
$$

$$\tag{2.56}$$

$$\tag{2.57}$$

2.4.4 Projecting

With the Eq. (2.57) primitive in hand, we turn our attention first to the task of projecting an arbitrary $\mathcal{P}$-field pattern onto a hidden target plane. Considering the Fig. 2-1 scenario, we imagine that the initial diffuser is preceded by an instance of the lens primitive depicted in Fig. 2-7, as shown in Fig. 2-8. To avoid confusion with the Fig. 2-7 scenario's preexisting notation, we will label the transverse coordinate of its input plane as $\boldsymbol{\rho}_{\mathrm{in}}$, its first distance as L_{in_1}, and its second distance as L_{in_2}. The output plane transverse coordinate remains as $\boldsymbol{\rho}_0$, leading into the same notation as Fig. 2-1

40
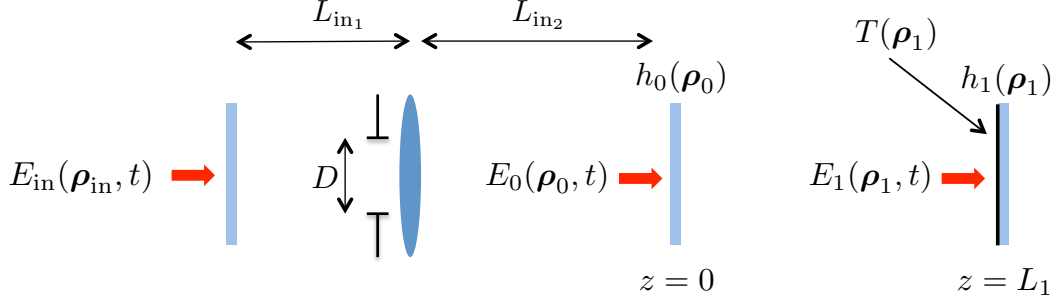
Figure 2-8: Geometry for projecting an arbitrary $\mathcal{P}$-field pattern onto a hidden target plane.

for the rest of the geometry. We take the lens to be configured to project the input $\mathcal{P}$ field onto the $z = L_1$ plane so that its focal length obeys $1/f = 1/L_{\text{in}_1} + 1/(L_{\text{in}_2} + L_1)$. For this configuration, $\Pi(f, L_{\text{in}_1}, L_{\text{in}_2}) = L_{\text{in}_2}(L_1 + L_{\text{in}_2})/L_1$, and so the lens primitive gives us

$$
\begin{aligned}
\mathcal{P}_0(\boldsymbol{\rho}_0, \omega_-) = & \left(\frac{L_1 + L_{\text{in}_2}}{L_1 L_{\text{in}_1}} \right)^2 e^{i\frac{\omega_-}{c}(L_{\text{in}_1} + L_{\text{in}_2})} e^{-i\frac{\omega_-}{c}\frac{|\boldsymbol{\rho}_0|^2}{2L_1}} \\
& \times \int d^2\boldsymbol{\rho}_{\text{in}} \, \mathcal{P}_{\text{in}}(\boldsymbol{\rho}_{\text{in}}, \omega_-) e^{i\frac{\omega_-}{c}\frac{|\boldsymbol{\rho}_{\text{in}}|^2}{2L_{\text{in}_1}}\left(1 - \frac{L_{\text{in}_2}(L_1 + L_{\text{in}_2})}{L_1 L_{\text{in}_1}}\right)} \\
& \times e^{-\frac{\left| \frac{\boldsymbol{\rho}_{\text{in}}}{L_{\text{in}_1}} + \frac{\boldsymbol{\rho}_0}{L_{\text{in}_2}} \right|^2}{D^2}\left(\frac{L_{\text{in}_2}(L_1 + L_{\text{in}_2})}{L_1} \right)^2} e^{-i\frac{\omega_-}{c}\frac{L_1 + L_{\text{in}_2}}{L_1 L_{\text{in}_1}}\boldsymbol{\rho}_{\text{in}}\cdot\boldsymbol{\rho}_0},
\end{aligned}
\tag{2.58}
$$

which, after Fresnel propagation, leads to

$$
\begin{aligned}
\mathcal{P}_1(\boldsymbol{\rho}_1, \omega_-) = & \left(\frac{L_1 + L_{\text{in}_2}}{L_1^2 L_{\text{in}_1}} \right)^2 e^{i\frac{\omega_-}{c}(L_{\text{in}_1} + L_{\text{in}_2} + L_1)} e^{i\frac{\omega_-}{c}\frac{|\boldsymbol{\rho}_1|^2}{2L_1}} \\
& \times \int d^2\boldsymbol{\rho}_{\text{in}} \, \mathcal{P}_{\text{in}}(\boldsymbol{\rho}_{\text{in}}, \omega_-) e^{i\frac{\omega_-}{c}\frac{|\boldsymbol{\rho}_{\text{in}}|^2}{2L_{\text{in}_1}}\left(1 - \frac{L_{\text{in}_2}(L_1 + L_{\text{in}_2})}{L_1 L_{\text{in}_1}}\right)} \\
& \times \int d^2\boldsymbol{\rho}_0 \, e^{-\frac{\left| \frac{\boldsymbol{\rho}_{\text{in}}}{L_{\text{in}_1}} + \frac{\boldsymbol{\rho}_0}{L_{\text{in}_2}} \right|^2}{D^2}\left(\frac{L_{\text{in}_2}(L_1 + L_{\text{in}_2})}{L_1} \right)^2} e^{-i\frac{\omega_-}{cL_1}\boldsymbol{\rho}_0\cdot\left(\boldsymbol{\rho}_1 + \frac{L_1 + L_{\text{in}_2}}{L_{\text{in}_1}}\boldsymbol{\rho}_{\text{in}} \right)}
\end{aligned}
\tag{2.59}
$$

$$
= \pi \left(\frac{D}{L_1 L_{\mathrm{in}_1}}\right)^2 e^{i\frac{\omega_-}{c}(L_{\mathrm{in}_1}+L_{\mathrm{in}_2}+L_1)} e^{i\frac{\omega_-}{c}\frac{|\boldsymbol{\rho}_1|^2}{2L_1}}
$$

$$
\times \int \mathrm{d}^2\boldsymbol{\rho}_{\mathrm{in}}\, \mathcal{P}_{\mathrm{in}}(\boldsymbol{\rho}_{\mathrm{in}},\omega_-) e^{i\frac{\omega_-}{c}\frac{|\boldsymbol{\rho}_{\mathrm{in}}|^2}{2L_{\mathrm{in}_1}}\left(1-\frac{L_{\mathrm{in}_2}(L_1+L_{\mathrm{in}_2})}{L_1 L_{\mathrm{in}_1}}\right)} e^{-\frac{\omega_-^2 D^2}{4c^2}\frac{\left|\boldsymbol{\rho}_1+\frac{L_1+L_{\mathrm{in}_2}}{L_{\mathrm{in}_1}}\boldsymbol{\rho}_{\mathrm{in}}\right|^2}{(L_1+L_{\mathrm{in}_2})^2}}
$$

$$
\times\, e^{i\frac{\omega_-}{c}\frac{L_{\mathrm{in}_2}}{L_1 L_{\mathrm{in}_1}}\boldsymbol{\rho}_{\mathrm{in}}\cdot\left(\boldsymbol{\rho}_1+\frac{L_1+L_{\mathrm{in}_2}}{L_{\mathrm{in}_1}}\boldsymbol{\rho}_{\mathrm{in}}\right)} \tag{2.60}
$$

$$
= \pi \left(\frac{D}{L_1 L_{\mathrm{in}_1}}\right)^2 e^{i\frac{\omega_-}{c}(L_{\mathrm{in}_1}+L_{\mathrm{in}_2}+L_1)} e^{i\frac{\omega_-|\boldsymbol{\rho}_1|^2}{2c(L_1+L_{\mathrm{in}_2})}}
$$

$$
\times \int \mathrm{d}^2\boldsymbol{\rho}_{\mathrm{in}}\, \mathcal{P}_{\mathrm{in}}(\boldsymbol{\rho}_{\mathrm{in}},\omega_-) e^{i\frac{\omega_-|\boldsymbol{\rho}_{\mathrm{in}}|^2}{2cL_{\mathrm{in}_1}}} e^{-\frac{\omega_-^2 D^2}{4c^2}\frac{\left|\boldsymbol{\rho}_1+\frac{L_1+L_{\mathrm{in}_2}}{L_{\mathrm{in}_1}}\boldsymbol{\rho}_{\mathrm{in}}\right|^2}{(L_1+L_{\mathrm{in}_2})^2}}
$$

$$
\times\, e^{i\frac{\omega_-}{2c}\frac{L_{\mathrm{in}_2}}{L_1(L_1+L_{\mathrm{in}_2})}\left|\boldsymbol{\rho}_1+\frac{L_1+L_{\mathrm{in}_2}}{L_{\mathrm{in}_1}}\boldsymbol{\rho}_{\mathrm{in}}\right|^2}. \tag{2.61}
$$

Now we assume a more stringent condition for D, in particular that $D \gg \sqrt{\frac{c}{\omega_-}\frac{L_{\mathrm{in}_2}(L_1+L_{\mathrm{in}_2})}{L_1}}$. For meter-scale distances and 10-GHz-scale modulation this reduces to approximately $D \gg 10\,\mathrm{cm}$ which, although likely difficult to meet in practice, is at least imaginable, perhaps by using a large concave mirror to function as the lens. Each order-of-magnitude increase of the modulation frequency reduces the requirement on D by half an order of magnitude, so THz-scale modulation—as implemented by the synthetic-wavelength-holography approach of Willomitzer *et al.* [14] that we discuss further in Appendix D—would reduce this condition to a more reasonable $D \gg 1\,\mathrm{cm}$. If we can achieve this condition, then the final phase term in Eq. (2.61) can be ignored and we get

$$
\mathcal{P}_1(\boldsymbol{\rho}_1,\omega_-) = \pi \left(\frac{D}{L_1 L_{\mathrm{in}_1}}\right)^2 e^{i\frac{\omega_-}{c}(L_{\mathrm{in}_1}+L_{\mathrm{in}_2}+L_1)} e^{i\frac{\omega_-|\boldsymbol{\rho}_1|^2}{2c(L_1+L_{\mathrm{in}_2})}}
$$

$$
\times \int \mathrm{d}^2\boldsymbol{\rho}_{\mathrm{in}}\, \mathcal{P}_{\mathrm{in}}(\boldsymbol{\rho}_{\mathrm{in}},\omega_-) e^{i\frac{\omega_-|\boldsymbol{\rho}_{\mathrm{in}}|^2}{2cL_{\mathrm{in}_1}}} e^{-\frac{\omega_-^2 D^2}{4c^2}\frac{\left|\boldsymbol{\rho}_1+\frac{L_1+L_{\mathrm{in}_2}}{L_{\mathrm{in}_1}}\boldsymbol{\rho}_{\mathrm{in}}\right|^2}{(L_1+L_{\mathrm{in}_2})^2}}. \tag{2.62}
$$

Defining $L_{\text{prj}} \equiv L_{\text{in}_2} + L_1$ and denoting the magnification/minification factor by $M \equiv L_{\text{prj}}/L_{\text{in}_1}$, this result simplifies to

$$
\begin{aligned}
\mathcal{P}_1(\boldsymbol{\rho}_1, \omega_-) =& \pi \left(\frac{D}{L_1 L_{\text{in}_1}} \right)^2 e^{i\omega_-(L_{\text{in}_1}+L_{\text{prj}})/c} e^{i\omega_-|\boldsymbol{\rho}_1|^2/2cL_{\text{prj}}} \\
& \times \int \mathrm{d}^2\boldsymbol{\rho}_{\text{in}} \, \mathcal{P}_{\text{in}}(\boldsymbol{\rho}_{\text{in}}, \omega_-) e^{i\omega_-|\boldsymbol{\rho}_{\text{in}}|^2/2cL_{\text{in}_1}} e^{-(\omega_- D/2cL_{\text{prj}})^2|\boldsymbol{\rho}_1+M\boldsymbol{\rho}_{\text{in}}|^2}.
\end{aligned} \tag{2.63}
$$

Ignoring inessential phase and scaling terms, this is a projected copy of the input $\mathcal{P}$ field,

$$
\mathcal{P}_{\text{in}}(\boldsymbol{\rho}_{\text{in}}, \omega_-) = \int \frac{\mathrm{d}\omega_+}{2\pi} \, \mathcal{E}_{\text{in}}(\boldsymbol{\rho}_{\text{in}}, \omega_+ + \omega_-/2) \mathcal{E}_{\text{in}}^*(\boldsymbol{\rho}_{\text{in}}, \omega_+ - \omega_-/2), \tag{2.64}
$$

subject to image inversion and magnification/minification, with resolution diffraction limited at the modulation wavelength.

2.4.5 Imaging
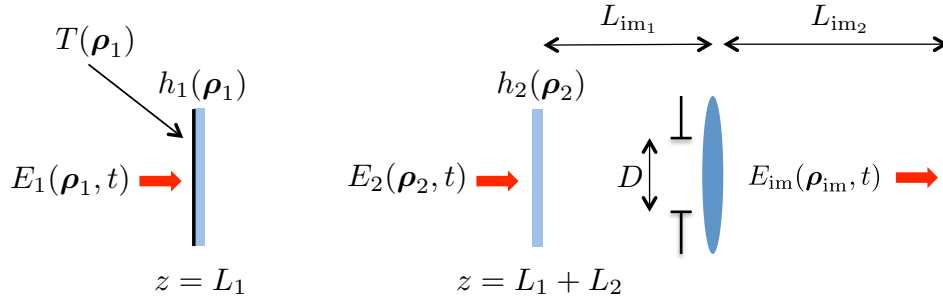
Figure 2-9: Geometry for directly imaging a hidden target plane.

We can obtain the same kind of result we've just exhibited for projection for imaging the hidden plane by placing the lens primitive behind Fig. 2-1's final diffuser so that the transverse coordinate of the first plane of the primitive is $\boldsymbol{\rho}_2$, as depicted in Fig. 2-9. We denote the lens primitive's two distances L_{im_1} and L_{im_2}, and we denote the transverse coordinate of the primitive's final plane as $\boldsymbol{\rho}_{\text{im}}$ with the intention in mind that a multipixel detector capable of measuring the $\mathcal{P}$ field will be present there. The hidden plane is imaged onto this hypothetical detector by taking the focal length of the lens to obey $1/f = 1/(L_2 + L_{\text{im}_1}) + 1/L_{\text{im}_2}$. For this configuration

43

$\Pi(f, L_{\text{im}_1}, L_{\text{im}_2}) = L_{\text{im}_1}(L_2 + L_{\text{im}_1})/L_2$, and so we have that

$$
\begin{aligned}
\mathcal{P}_{\text{im}}(\boldsymbol{\rho}_{\text{im}}, \omega_-) = \quad & \left(\frac{L_2 + L_{\text{im}_1}}{L_2 L_{\text{im}_2}}\right)^2 e^{i\frac{\omega_-}{c}(L_{\text{im}_1}+L_{\text{im}_2})} e^{i\frac{\omega_-}{c}\frac{|\boldsymbol{\rho}_{\text{im}}|^2}{2L_{\text{im}_2}}\left(1-\frac{L_{\text{im}_1}(L_2+L_{\text{im}_1})}{L_2 L_{\text{im}_2}}\right)} \\
& \times \int \mathrm{d}^2\boldsymbol{\rho}_2\, \mathcal{P}_2(\boldsymbol{\rho}_2, \omega_-) e^{-i\frac{\omega_-}{c}\frac{|\boldsymbol{\rho}_2|^2}{2L_2}} e^{-\frac{\left|\frac{\boldsymbol{\rho}_2}{L_{\text{im}_1}}+\frac{\boldsymbol{\rho}_{\text{im}}}{L_{\text{im}_2}}\right|^2}{D^2}\left(\frac{L_{\text{im}_1}(L_2+L_{\text{im}_1})}{L_2}\right)^2} \\
& \times e^{-i\frac{\omega_-}{c}\frac{L_2+L_{\text{im}_1}}{L_2 L_{\text{im}_2}}\boldsymbol{\rho}_{\text{im}}\cdot\boldsymbol{\rho}_2}
\end{aligned}
\tag{2.65}
$$

$$
\begin{aligned}
= \quad & \left(\frac{L_2 + L_{\text{im}_1}}{L_2^2 L_{\text{im}_2}}\right)^2 e^{i\frac{\omega_-}{c}(L_{\text{im}_1}+L_{\text{im}_2}+L_2)} e^{i\frac{\omega_-}{c}\frac{|\boldsymbol{\rho}_{\text{im}}|^2}{2L_{\text{im}_2}}\left(1-\frac{L_{\text{im}_1}(L_2+L_{\text{im}_1})}{L_2 L_{\text{im}_2}}\right)} \\
& \times \int \mathrm{d}^2\boldsymbol{\rho}_1\, T(\boldsymbol{\rho}_1)\mathcal{P}_1(\boldsymbol{\rho}_1, \omega_-) e^{i\frac{\omega_-}{c}\frac{|\boldsymbol{\rho}_1|^2}{2L_2}} \\
& \times \int \mathrm{d}^2\boldsymbol{\rho}_2\, e^{-\frac{\left|\frac{\boldsymbol{\rho}_2}{L_{\text{im}_1}}+\frac{\boldsymbol{\rho}_{\text{im}}}{L_{\text{im}_2}}\right|^2}{D^2}\left(\frac{L_{\text{im}_1}(L_2+L_{\text{im}_1})}{L_2}\right)^2} e^{-i\frac{\omega_-}{cL_2}\boldsymbol{\rho}_2\cdot\left(\boldsymbol{\rho}_1+\frac{L_2+L_{\text{im}_1}}{L_{\text{im}_2}}\boldsymbol{\rho}_{\text{im}}\right)}
\end{aligned}
\tag{2.66}
$$

$$
\begin{aligned}
= \quad & \pi\left(\frac{D}{L_2 L_{\text{im}_2}}\right)^2 e^{i\frac{\omega_-}{c}(L_{\text{im}_1}+L_{\text{im}_2}+L_2)} e^{i\frac{\omega_-}{c}\frac{|\boldsymbol{\rho}_{\text{im}}|^2}{2L_{\text{im}_2}}\left(1-\frac{L_{\text{im}_1}(L_2+L_{\text{im}_1})}{L_2 L_{\text{im}_2}}\right)} \\
& \times \int \mathrm{d}^2\boldsymbol{\rho}_1\, T(\boldsymbol{\rho}_1)\mathcal{P}_1(\boldsymbol{\rho}_1, \omega_-) e^{i\frac{\omega_-}{c}\frac{|\boldsymbol{\rho}_1|^2}{2L_2}} e^{-\frac{D^2\omega_-^2}{4c^2}\frac{\left|\boldsymbol{\rho}_1+\frac{L_2+L_{\text{im}_1}}{L_{\text{im}_2}}\boldsymbol{\rho}_{\text{im}}\right|^2}{(L_2+L_{\text{im}_1})^2}} \\
& \times e^{i\frac{\omega_-}{c}\frac{L_{\text{im}_1}}{L_{\text{im}_2}L_2}\boldsymbol{\rho}_{\text{im}}\cdot\left(\boldsymbol{\rho}_1+\frac{L_2+L_{\text{im}_1}}{L_{\text{im}_2}}\boldsymbol{\rho}_{\text{im}}\right)}
\end{aligned}
\tag{2.67}
$$

$$
\begin{aligned}
= \quad & \pi\left(\frac{D}{L_2 L_{\text{im}_2}}\right)^2 e^{i\frac{\omega_-}{c}(L_{\text{im}_1}+L_{\text{im}_2}+L_2)} e^{i\frac{\omega_-|\boldsymbol{\rho}_{\text{im}}|^2}{2cL_{\text{im}_2}}} \\
& \times \int \mathrm{d}^2\boldsymbol{\rho}_1\, T(\boldsymbol{\rho}_1)\mathcal{P}_1(\boldsymbol{\rho}_1, \omega_-) e^{i\frac{\omega_-|\boldsymbol{\rho}_1|^2}{2c(L_2+L_{\text{im}_1})}} e^{-\frac{D^2\omega_-^2}{4c^2}\frac{\left|\boldsymbol{\rho}_1+\frac{L_2+L_{\text{im}_1}}{L_{\text{im}_2}}\boldsymbol{\rho}_{\text{im}}\right|^2}{(L_2+L_{\text{im}_1})^2}} \\
& \times e^{i\frac{\omega_-}{2c}\frac{L_{\text{im}_1}}{L_2(L_2+L_{\text{im}_1})}\left|\boldsymbol{\rho}_1+\frac{L_2+L_{\text{im}_1}}{L_{\text{im}_2}}\boldsymbol{\rho}_{\text{im}}\right|^2}.
\end{aligned}
\tag{2.68}
$$

Similar to the projection case, we enforce the assumption $D \gg \sqrt{\frac{c}{\omega_-}\frac{L_{\text{im}_1}(L_2+L_{\text{im}_1})}{L_2}}$

so that we can ignore the final phase term which leaves us with

$$\mathcal{P}_{\text{im}}(\boldsymbol{\rho}_{\text{im}}, \omega_-) = \pi \left(\frac{D}{L_2 L_{\text{im}_2}} \right)^2 e^{i\frac{\omega_-}{c}(L_{\text{im}_1} + L_{\text{im}_2} + L_2)} e^{i\frac{\omega_- |\boldsymbol{\rho}_{\text{im}}|^2}{2cL_{\text{im}_2}}}$$

$$\times \int \mathrm{d}^2 \boldsymbol{\rho}_1 \, T(\boldsymbol{\rho}_1) \mathcal{P}_1(\boldsymbol{\rho}_1, \omega_-) e^{i\frac{\omega_- |\boldsymbol{\rho}_1|^2}{2c(L_2 + L_{\text{im}_1})}} e^{-\frac{D^2 \omega_-^2}{4c^2} \frac{\left| \boldsymbol{\rho}_1 + \frac{L_2 + L_{\text{im}_1}}{L_{\text{im}_2}} \boldsymbol{\rho}_{\text{im}} \right|^2}{(L_2 + L_{\text{im}_1})^2}}. \quad (2.69)$$

Defining $L_{\text{out}} \equiv L_2 + L_{\text{im}_1}$ and denoting the magnification/minification factor by $M \equiv L_{\text{out}}/L_{\text{im}_2}$, this result simplifies to

$$\mathcal{P}_{\text{im}}(\boldsymbol{\rho}_{\text{im}}, \omega_-) = \pi \left(\frac{D}{L_2 L_{\text{im}_2}} \right)^2 e^{i\omega_-(L_{\text{out}} + L_{\text{im}_2})/c} e^{i\omega_- |\boldsymbol{\rho}_{\text{im}}|^2/2cL_{\text{im}_2}}$$

$$\times \int \mathrm{d}^2 \boldsymbol{\rho}_1 \, T(\boldsymbol{\rho}_1) \mathcal{P}_1(\boldsymbol{\rho}_1, \omega_-) e^{i\omega_- |\boldsymbol{\rho}_1|^2/2cL_{\text{out}}} e^{-(\omega_- D/2cL_{\text{out}})^2 |\boldsymbol{\rho}_1 + M\boldsymbol{\rho}_{\text{im}}|^2}.$$

$$(2.70)$$

Again ignoring inessential terms, this is an inverted and magnified/minified $\mathcal{P}$-field image of the hidden target plane with resolution diffraction limited at the modulation wavelength. Although it may prove difficult to implement in practice with existing technology, this offers the potential to directly image NLoS scenes with little to no computational overhead.

Chapter 3

Two-Frequency Spatial Wigner Distribution and Occlusion-Aided Imaging

In this chapter, we consider a generalized version of our paraxial, transmissive geometry that allows for the presence of deterministic occluders in the light's path and a more general target transmissivity mask. The $\mathcal{P}$ field alone does not suffice to track the evolution of the light through all intermediate planes of this geometry, so we go beyond this quantity to define a more comprehensive one: the two-frequency spatial Wigner distribution. We demonstrate how the two-frequency spatial Wigner distribution relates to other better-known quantities for characterizing propagation through random media, and we present a set of propagation primitives for it that are relevant to our transmissive geometry. We use these propagation primitives to analyze occlusion-aided imaging scenarios and demonstrate that the presence of intervening occluders has the potential to improve performance, as seen previously in Xu *et al.* [11] and Thrampoulidis *et al.* [12]. Finally, we isolate the key component of such scenarios to derive a concise, general $\mathcal{P}$-field propagation primitive and demonstrate that its behavior is intuitive in the geometric-optics limit.

3.1 Setup for Paraxial Propagation through Multiple Diffusers with Occlusion

Figure 3-1 shows a generalized setup for transmissive $\mathcal{P}$-field imaging. Here, two occluders, having field-transmission functions $P(\boldsymbol{\rho}_d)$ and $P'(\boldsymbol{\rho}'_d)$, have been introduced in the $z = L_1 - L_d$ and $z = L_1 + L'_d$ planes, and the $z = L_1$ plane contains a field-transmission mask $F(\boldsymbol{\rho}_1)$ that has both specular and diffuse components. In the NLoS analogy, the two occluders represent objects in the hidden space—encountered by the light as it propagates towards and returns from the hidden wall, respectively—and the generalized field-transmission mask accounts for more general, non-Lambertian hidden walls. This configuration—if $F(\boldsymbol{\rho}_1)$ is purely diffuse with a space-varying albedo that is to be imaged, i.e., equivalent to the stacked intensity-transmission mask and thin diffuser from Fig. 2-1—is our unfolded proxy for Xu *et al.*'s experiments [11].

The ultimate goal of a phasor-field transport model is to provide the diffuser-averaged STA irradiance at the output of some system—or equivalently, its Fourier transform: the $\mathcal{P}$ field—given the STA irradiance[1], or its associated $\mathcal{P}$ field, at the input of the system. This is possible in NLoS or diffuse transmissive-imaging scenarios—provided that the system can be summarized by a linear transformation of the underlying electromagnetic field—when the input and output facets of the systems in question are Lambertian walls (NLoS case) or diffusers (transmissive case). Such facets destroy all directionality information, viz., all spatial coherence, so that $\mathcal{P}$-fields fully characterize the light they reflect (NLoS case) or transmit (transmissive case). Free-space propagation increases spatial coherence, but provided we only care about relating the STA irradiance at the input plane to the diffuser-averaged STA irradiance at the output plane when those planes contain pure diffusers, a $\mathcal{P}$-field input-output model propagation is possible as those diffusers will, respectively, destroy the initial and propagation-created coherence. If, however, as at $z = L_1 - L_d$, $z = L_1$, or $z = L_1 + L'_d$ in Fig. 3-1, we are interested in planes that do *not* contain pure diffusers, the $\mathcal{P}$ field is insufficient to fully characterize the electromagnetic field

---

[1]For laser illumination at the system's input, diffuser averaging is unnecessary.

emerging from them. Thus, owing to what can be viewed as a lack of directionality information, the $\mathcal{P}$ field at those output planes fails to provide enough information to determine the increased spatial coherence that will accrue from subsequent free-space diffraction. Accordingly, we find the $\mathcal{P}$ field insufficient for the task of building a complete light-transport model for scenarios including occluders and specular-plus-diffuser masks. Indeed, although omitted for brevity, carrying out a Fig. 3-1 propagation analysis—like that done for Fig. 2-1—confirms that a $\mathcal{P}$-field input-output relation built up from propagating the $\mathcal{P}$ field from each plane containing an optical element to the next such plane is impossible. A simple demonstration of the underlying issue is presented in Appendix B, where we show that even free-space propagation cannot be cascaded for the $\mathcal{P}$ field.
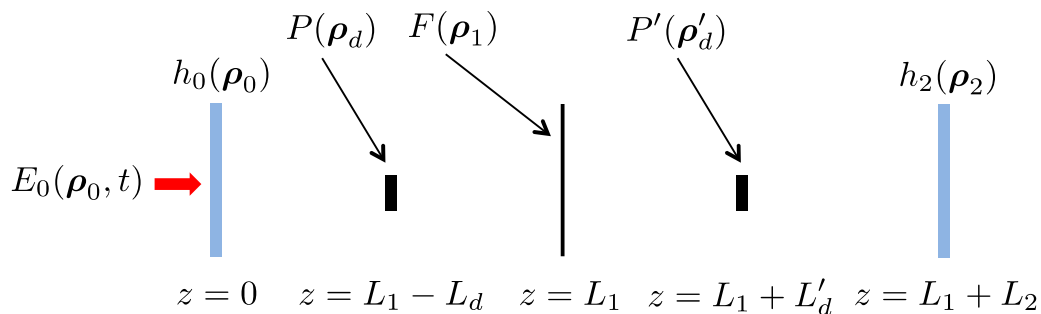
Figure 3-1: Unfolded geometry for three-bounce, occlusion-aided NLoS active imaging. Scalar, paraxial diffraction theory is assumed, with $E_0(\boldsymbol{\rho}_0, t)$ being the baseband complex field envelope illuminating the $z = 0$ plane and $E'_2(\boldsymbol{\rho}_2, t)$ being the baseband complex field envelope emerging from the $z = L_1 + L_2$ plane. These fields are written as functions of their transverse spatial coordinates, $\{\boldsymbol{\rho}_k = (x_k, y_k) : k = 0, 2\}$, in their respective planes and time, t. The blue rectangles represent thin transmissive diffusers, and the black line at $z = L_1$ represents a thin specular-plus-diffuser transmission mask with field-transmission function $F(\boldsymbol{\rho}_1)$, whose associated intensity-transmission pattern is to be imaged using the light that emerges from the $z = L_1 + L_2$ plane. That imaging process is aided by the presence of occluders in the $z = L_1 - L_d$ and $z = L_1 + L'_d$ planes, whose field-transmission functions are $P(\boldsymbol{\rho}_d)$ and $P'(\boldsymbol{\rho}'_d)$, respectively.

To tackle these scenarios, we start from the beginning, and instead of considering the STA irradiance we consider a variant with directionality information—the time-dependent specific irradiance from small-angle-approximation linear transport

theory [15]:

$$I_z(\boldsymbol{\rho}_+, \mathbf{s}, t) \equiv \int \frac{\mathrm{d}^2 \boldsymbol{\rho}_-}{\lambda_0^2} \langle E_z(\boldsymbol{\rho}_+ + \boldsymbol{\rho}_-/2, t) E_z^*(\boldsymbol{\rho}_+ - \boldsymbol{\rho}_-/2, t) \rangle e^{-i2\pi\mathbf{s}\cdot\boldsymbol{\rho}_-/\lambda_0}, \qquad (3.1)$$

where $\mathbf{s}$ is the transverse component of the propagation direction, i.e., a normalized copy of the transverse wave vector $\mathbf{k}$. In computer vision, this quantity is known as the 5D light field [16–18]. By replacing $2\pi\mathbf{s}/\lambda_0$ with $\mathbf{k}$, the time-dependent specific irradiance can be seen to be a time-indexed spatial Wigner distribution, cf. the spatial Wigner distribution of a monochromatic scalar wave, viz.,

$$W(\boldsymbol{\rho}_+, \mathbf{k}) \equiv \int \mathrm{d}^2 \boldsymbol{\rho}_- \, E_z(\boldsymbol{\rho}_+ + \boldsymbol{\rho}_-/2) E_z^*(\boldsymbol{\rho}_+ - \boldsymbol{\rho}_-/2) e^{-i\mathbf{k}\cdot\boldsymbol{\rho}_-}, \qquad (3.2)$$

which has long been recognized as a useful tool in optics, see, e.g., [19–21]. The diffuser-averaged STA irradiance is obtained from $I_z(\boldsymbol{\rho}_+, \mathbf{s}, t)$ by integrating out its directionality information,

$$\langle I_z(\boldsymbol{\rho}_+, t) \rangle = \int \mathrm{d}^2 \mathbf{s} \, I_z(\boldsymbol{\rho}_+, \mathbf{s}, t), \qquad (3.3)$$

and the $\mathcal{P}$ field is then obtained by time-domain Fourier transformation.

As before, we find it convenient to carry out our analysis in the temporal-frequency domain. Paralleling the development in Eqs. (2.7)–(2.9) we have:

$$I_z(\boldsymbol{\rho}_+, \mathbf{s}, t)$$
$$= \int \frac{\mathrm{d}\omega}{2\pi} \int \frac{\mathrm{d}\omega'}{2\pi} \int \frac{\mathrm{d}^2 \boldsymbol{\rho}_-}{\lambda_0^2} \langle \mathcal{E}_z(\boldsymbol{\rho}_+ + \boldsymbol{\rho}_-/2, \omega) \mathcal{E}_z^*(\boldsymbol{\rho}_+ - \boldsymbol{\rho}_-/2, \omega') \rangle e^{-i\frac{2\pi\mathbf{s}}{\lambda_0}\cdot\boldsymbol{\rho}_-} e^{-i(\omega-\omega')t}$$
$$\tag{3.4}$$
$$= \int \frac{\mathrm{d}\omega_-}{2\pi} \left[\int \frac{\mathrm{d}\omega_+}{2\pi} \left(\int \frac{\mathrm{d}^2 \boldsymbol{\rho}_-}{\lambda_0^2} \langle \mathcal{E}_z(\boldsymbol{\rho}_+ + \boldsymbol{\rho}_-/2, \omega) \mathcal{E}_z^*(\boldsymbol{\rho}_+ - \boldsymbol{\rho}_-/2, \omega') \rangle e^{-i\frac{2\pi\mathbf{s}}{\lambda_0}\cdot\boldsymbol{\rho}_-} \right) \right] e^{-i\omega_- t},$$
$$\tag{3.5}$$

where $\omega_+ \equiv (\omega + \omega')/2$ and $\omega_- \equiv \omega - \omega'$ as we employed in Chapter 2. The bracketed quantity in Eq. (3.5) is the Fourier transform of the time-dependent specific irradiance,

so it contains equivalent information. Comparing to our Chapter 2 analysis, this quantity is the directionality-augmented analog of the $\mathcal{P}$ field, and as it turns out would be sufficient to build a transport model for the Fig. 3-1 scenario. Out of prudence though, having learned from the insufficient generality of the $\mathcal{P}$ field, we feel it is wise to build our Fig. 3-1 analysis on the quantity in parentheses within Eq. (3.5), the two-frequency spatial Wigner distribution (TFSWD):

$$
\begin{aligned}
&W_{\mathcal{E}_z}(\boldsymbol{\rho}_+, \mathbf{k}, \omega_+, \omega_-) \\
&\equiv \int \mathrm{d}^2\boldsymbol{\rho}_- \, \langle \mathcal{E}_z(\boldsymbol{\rho}_+ + \boldsymbol{\rho}_-/2, \omega_+ + \omega_-/2)\mathcal{E}_z^*(\boldsymbol{\rho}_+ - \boldsymbol{\rho}_-/2, \omega_+ - \omega_-/2)\rangle e^{-i\mathbf{k}\cdot\boldsymbol{\rho}_-}, \quad (3.6)
\end{aligned}
$$

from which the time-dependent specific irradiance can be obtained via

$$
I_z(\boldsymbol{\rho}_+, \mathbf{s}, t) = \frac{1}{\lambda_0^2} \int \frac{\mathrm{d}\omega_-}{2\pi} \int \frac{\mathrm{d}\omega_+}{2\pi} \, W_{\mathcal{E}_z}(\boldsymbol{\rho}_+, 2\pi\mathbf{s}/\lambda_0, \omega_+, \omega_-) e^{-i\omega_- t}. \quad (3.7)
$$

The merit of the TFSWD's added generality can be seen by considering the space-time autocorrelation function,

$$
\Gamma_z(\boldsymbol{\rho}_1, \boldsymbol{\rho}_2, t_1, t_2) \equiv \langle E_z(\boldsymbol{\rho}_1, t_1)E_z^*(\boldsymbol{\rho}_2, t_2)\rangle, \quad (3.8)
$$

that is used in parabolic-approximation propagation theory through random media [22]. The time-dependent specific irradiance can be found from the space-time autocorrelation function, viz., we have that

$$
I_z(\boldsymbol{\rho}_+, \mathbf{s}, t) = \int \frac{\mathrm{d}^2\boldsymbol{\rho}_-}{\lambda_0^2} \, \Gamma_z(\boldsymbol{\rho}_+ + \boldsymbol{\rho}_-/2, \boldsymbol{\rho}_+ - \boldsymbol{\rho}_-/2, t, t) e^{-i2\pi\mathbf{s}\cdot\boldsymbol{\rho}_-/\lambda_0}, \quad (3.9)
$$

but the converse is not true, i.e., the space-time autocorrelation function cannot in general be found from knowledge of the time-dependent specific irradiance alone. However, the space-time autocorrelation function is equivalent to the TFSWD because

we have that

$$W_{\mathcal{E}_z}(\boldsymbol{\rho}_+, \mathbf{k}, \omega_+, \omega_-) = \int d^2\boldsymbol{\rho}_- \int dt_1 \int dt_2 \, e^{i(\omega_+ t_- + \omega_- t_+ - \mathbf{k} \cdot \boldsymbol{\rho}_-)}$$

$$\times \, \Gamma_z(\boldsymbol{\rho}_+ + \boldsymbol{\rho}_-/2, \boldsymbol{\rho}_+ - \boldsymbol{\rho}_-/2, t_+ + t_-/2, t_+ - t_-/2), \quad (3.10)$$

where $t_+ \equiv (t_1 + t_2)/2$, $t_- \equiv t_1 - t_2$, and

$$\Gamma_z(\boldsymbol{\rho}_+ + \boldsymbol{\rho}_-/2, \boldsymbol{\rho}_+ - \boldsymbol{\rho}_-/2, t_+ + t_-/2, t_+ - t_-/2)$$
$$= \int \frac{d^2\mathbf{k}}{(2\pi)^2} \int \frac{d\omega_+}{2\pi} \int \frac{d\omega_-}{2\pi} \, W_{\mathcal{E}_z}(\boldsymbol{\rho}_+, \mathbf{k}, \omega_+, \omega_-) e^{-i(\omega_+ t_- + \omega_- t_+ - \mathbf{k} \cdot \boldsymbol{\rho}_-)}. \quad (3.11)$$

For E-field propagation through an arbitrary linear transformation of the form

$$E_{z'}(\boldsymbol{\rho}', t) = \int d\tau \int d^2\boldsymbol{\rho} \, E_z(\boldsymbol{\rho}, \tau) h(\boldsymbol{\rho}', \boldsymbol{\rho}; t, \tau), \quad (3.12)$$

the input's space-time autocorrelation function suffices to determine the output's space-time autocorrelation function, and hence the output-plane $\mathcal{P}$ field. Moreover, the same must be true for the TFSWD. Because knowledge of the time-dependent specific irradiance alone does not in general determine the space-time autocorrelation function, it does *not* suffice to characterize second-moment propagation through an arbitrary linear transformation of the form given in Eq. (3.12), i.e., it cannot determine the output $\mathcal{P}$ field. For example, the time-dependent specific irradiance cannot account for propagation that involves a linear time-invariant filtering in time, e.g., through a transparency that has a frequency-dependent transmissivity. So, although this capability is not fully exploited in this thesis, by building our theory around the TFSWD we are prepared to handle arbitrary linear transformations of the E field, rather than just those that can be characterized by the time-dependent specific irradiance. Note that the 6D light field,

$$I_z(\boldsymbol{\rho}_+, \mathbf{s}, \omega_+, t) \equiv \frac{1}{\lambda_0^2} \int \frac{d\omega_-}{2\pi} \, W(\boldsymbol{\rho}_+, 2\pi\mathbf{s}/\lambda_0, \omega_+, \omega_-) e^{-i\omega_- t}, \quad (3.13)$$

would also suffice in this regard, as it is the time-domain inverse Fourier transform of the TFSWD.

The z-plane $\mathcal{P}$ field can be found from that plane's TFSWD as follows:

$$\mathcal{P}_z(\boldsymbol{\rho}_+, \omega_-) = \int \frac{\mathrm{d}\omega_+}{2\pi} \int \frac{\mathrm{d}^2 \mathbf{k}}{(2\pi)^2}\, W_{\mathcal{E}_z}(\boldsymbol{\rho}_+, \mathbf{k}, \omega_+, \omega_-). \tag{3.14}$$

From this result we see that the TFSWD allows us to realize the goal of analyzing occluded phasor-field imaging if we can: (1) propagate $W_{\mathcal{E}_z}(\boldsymbol{\rho}_+, \mathbf{k}, \omega_+, \omega_-)$ through a z-plane field-transmission mask, whether that be a diffuser, deterministic occluder, or specular-plus-diffuser mask; and (2) propagate $W_{\mathcal{E}_z}(\boldsymbol{\rho}_+, \mathbf{k}, \omega_+, \omega_-)$ through a distance L of Fresnel diffraction. All of these propagation calculations are done Appendix C. For convenience, we summarize these results below:

Propagation through a diffuser:

For propagation through a diffuser characterized by the impulse approximation in Eq. (2.13), we have

$$W_{\mathcal{E}_0'}(\boldsymbol{\rho}_+, \mathbf{k}, \omega_+, \omega_-) = \lambda_0^2 \int \frac{\mathrm{d}^2 \mathbf{k}'}{(2\pi)^2}\, W_{\mathcal{E}_0}(\boldsymbol{\rho}_+, \mathbf{k}', \omega_+, \omega_-). \tag{3.15}$$

Propagation through a deterministic occluder:

With $W_P(\boldsymbol{\rho}_+, \mathbf{k}) \equiv \int \mathrm{d}^2 \boldsymbol{\rho}_-\, P(\boldsymbol{\rho}_+ + \boldsymbol{\rho}_-/2) P^*(\boldsymbol{\rho}_+ - \boldsymbol{\rho}_-/2) e^{-i\mathbf{k}\cdot\boldsymbol{\rho}_-}$, we have

$$W_{\mathcal{E}_{L_1-L_d}'}(\boldsymbol{\rho}_+, \mathbf{k}, \omega_+, \omega_-) = \int \frac{\mathrm{d}^2 \mathbf{k}'}{(2\pi)^2}\, W_{\mathcal{E}_{L_1-L_d}}(\boldsymbol{\rho}_+, \mathbf{k}', \omega_+, \omega_-) W_P(\boldsymbol{\rho}_+, \mathbf{k} - \mathbf{k}'). \tag{3.16}$$

Propagation through a specular-plus-diffuser mask:

With $F(\boldsymbol{\rho}_1)$ having nonzero mean $\langle F(\boldsymbol{\rho}_1)\rangle \neq 0$ and covariance $\langle \Delta F(\boldsymbol{\rho}_+ + \boldsymbol{\rho}_-/2) \Delta F^*(\boldsymbol{\rho}_+ - \boldsymbol{\rho}_-/2)\rangle \approx \lambda_0^2 \mathcal{F}(\boldsymbol{\rho}_+)\delta(\boldsymbol{\rho}_-)$ where $0 \leq \mathcal{F}(\boldsymbol{\rho}_+) \leq 1$, we get

$$\begin{aligned}
W_{\mathcal{E}_{L_1}'}(\boldsymbol{\rho}_+, \mathbf{k}, \omega_+, \omega_-) = \ & \int \frac{\mathrm{d}^2 \mathbf{k}'}{(2\pi)^2}\, W_{\mathcal{E}_{L_1}}(\boldsymbol{\rho}_+, \mathbf{k}', \omega_+, \omega_-) W_{\langle F\rangle}(\boldsymbol{\rho}_+, \mathbf{k} - \mathbf{k}') \\
& + \ \lambda_0^2 \mathcal{F}(\boldsymbol{\rho}_+) \int \frac{\mathrm{d}^2 \mathbf{k}'}{(2\pi)^2}\, W_{\mathcal{E}_{L_1}}(\boldsymbol{\rho}_+, \mathbf{k}', \omega_+, \omega_-). \tag{3.17}
\end{aligned}$$

Fresnel diffraction:

For Fresnel diffraction from the $z = 0_+$ plane to the $z = L_1 - L_d$ plane, we get

$$W_{\mathcal{E}_{L_1-L_d}}(\boldsymbol{\rho}_+, \mathbf{k}, \omega_+, \omega_-) = W_{\mathcal{E}_0'}\left(\boldsymbol{\rho}_+ - \frac{c(L_1 - L_d)\mathbf{k}}{\omega_0}, \mathbf{k}, \omega_+, \omega_-\right) e^{i\frac{\omega_-(L_1-L_d)}{c}\left(1+\frac{c^2|\mathbf{k}|^2}{2\omega_0^2}\right)} \tag{3.18}$$

3.2   Occlusion-Aided Imaging

In Chapter 2 we noted that, in the paraxial limit, unoccluded imaging configurations without modulated light are unconditioned with respect to reconstructing the target mask's albedo. Moreover, we showed that the addition of modulation enabled reconstruction of the target mask's albedo at a resolution limited by the bandwidth of that modulation. What remains then is to examine the unmodulated and modulated cases for occluded geometries. For clarity and convenience, we will consider a simplified version of Fig. 3-1 in which the first occluder is absent, the screen at $z = L_1$ is purely diffuse, and the occluder that is present at $z = L_1 + L_d'$ is denoted $P(\cdot)$ instead of $P'(\cdot)$. In the NLoS analogy, this corresponds to a geometry in which a single occluding object is encountered in the hidden space only on the light's return trip from a Lambertian hidden wall. Further convenience, without appreciable loss of generality, is afforded by our assuming that the laser light incident on the $z = 0$ plane is a $+z$-going plane wave of STA irradiance $I_0(t)$, and that the distances in Fig. 3-1 satisfy $L_1 = L_2 = L$, and $L_d' = L/2$.

The TFSWD of the plane-wave laser light is easily shown to be

$$W_{\mathcal{E}_0}(\boldsymbol{\rho}_+, \mathbf{k}, \omega_+, \omega_-) = W_{\text{in}}(\omega_+, \omega_-)(2\pi/\lambda_0)^2 \delta(\mathbf{k}), \tag{3.19}$$

where

$$W_{\text{in}}(\omega_+, \omega_-) \equiv \lambda_0^2 \int dt\, \sqrt{I_0(t)} e^{i(\omega_+ + \omega_-/2)t} \int du\, \sqrt{I_0(u)} e^{-i(\omega_+ - \omega_-/2)u}. \tag{3.20}$$

After the diffuser in the $z = 0$ plane we get

$$W_{\mathcal{E}_0'}(\boldsymbol{\rho}_+, \mathbf{k}, \omega_+, \omega_-) = W_{\mathrm{in}}(\omega_+, \omega_-), \qquad (3.21)$$

and after propagation to the $z = L$ plane, we find

$$W_{\mathcal{E}_L}(\boldsymbol{\rho}_+, \mathbf{k}, \omega_+, \omega_-) = W_{\mathrm{in}}(\omega_+, \omega_-)e^{i(\omega_- L/c)(1+c^2|\mathbf{k}|^2/2\omega_0^2)}. \qquad (3.22)$$

At $z = L_1$ this Wigner distribution encounters a diffuse target mask, i.e., one whose field-transmission function $F(\boldsymbol{\rho}_1)$ has zero mean and covariance

$$\langle \Delta F(\boldsymbol{\rho}_1) \Delta F^*(\boldsymbol{\rho}_2) \rangle = \lambda_0^2 \mathcal{F}[(\boldsymbol{\rho}_1 + \boldsymbol{\rho}_2)/2]\delta(\boldsymbol{\rho}_1 - \boldsymbol{\rho}_2), \qquad (3.23)$$

which results in

$$W_{\mathcal{E}_L'}(\boldsymbol{\rho}_+, \mathbf{k}, \omega_+, \omega_-) = \mathcal{F}(\boldsymbol{\rho}_+)W_{\mathrm{in}}(\omega_+, \omega_-)e^{i\omega_- L/c}\, 2\pi i c/\omega_- L. \qquad (3.24)$$

Fresnel propagation to $z = 3L/2$ now gives us

$$\begin{aligned}
W_{\mathcal{E}_{3L/2}}(\boldsymbol{\rho}_+, \mathbf{k}, \omega_+, \omega_-) = & \mathcal{F}(\boldsymbol{\rho}_+ - cL\mathbf{k}/2\omega_0)W_{\mathrm{in}}(\omega_+, \omega_-) \\
& \times e^{i\omega_- 3L/2c}e^{i\omega_- cL|\mathbf{k}|^2/4\omega_0^2}\, 2\pi i c/\omega_- L,
\end{aligned} \qquad (3.25)$$

and passage through the occluder in that plane leads to

$$\begin{aligned}
W_{\mathcal{E}_{3L/2}'}(\boldsymbol{\rho}_+, \mathbf{k}, \omega_+, \omega_-) = & W_{\mathrm{in}}(\omega_+, \omega_-)\int \frac{\mathrm{d}^2\mathbf{k}'}{(2\pi)^2}\, \mathcal{F}(\boldsymbol{\rho}_+ - cL\mathbf{k}'/2\omega_0)e^{i\omega_- 3L/2c}e^{i\omega_- cL|\mathbf{k}'|^2/4\omega_0^2} \\
& \times W_P(\boldsymbol{\rho}_+, \mathbf{k} - \mathbf{k}')2\pi i c/\omega_- L.
\end{aligned} \qquad (3.26)$$

Fresnel propagation over another $L/2$ distance then gives

$$W_{\mathcal{E}_{2L}}(\boldsymbol{\rho}_+, \mathbf{k}, \omega_+, \omega_-) = W_{\text{in}}(\omega_+, \omega_-) \int \frac{\mathrm{d}^2\mathbf{k}'}{(2\pi)^2} \mathcal{F}(\boldsymbol{\rho}_+ - cL(\mathbf{k}' + \mathbf{k})/2\omega_0) e^{i\omega_- 2L/c}$$

$$\times\, e^{i\omega_- cL(|\mathbf{k}|^2 + |\mathbf{k}'|^2)/4\omega_0^2} W_P(\boldsymbol{\rho}_+ - cL\mathbf{k}/2\omega_0, \mathbf{k} - \mathbf{k}') 2\pi i c/\omega_- L, \tag{3.27}$$

from which we get

$$\mathcal{P}_{2L}(\boldsymbol{\rho}_+, \omega_-) = \int \frac{\mathrm{d}\omega_+}{2\pi} W_{\text{in}}(\omega_+, \omega_-) \int \frac{\mathrm{d}^2\mathbf{k}}{(2\pi)^2} \int \frac{\mathrm{d}^2\mathbf{k}'}{(2\pi)^2} \mathcal{F}(\boldsymbol{\rho}_+ - cL(\mathbf{k}' + \mathbf{k})/2\omega_0) e^{i\omega_- 2L/c}$$

$$\times\, e^{i\omega_- cL(|\mathbf{k}|^2 + |\mathbf{k}'|^2)/4\omega_0^2} W_P(\boldsymbol{\rho}_+ - cL\mathbf{k}/2\omega_0, \mathbf{k} - \mathbf{k}') 2\pi i c/\omega_- L. \tag{3.28}$$

Now, using

$$\mathcal{P}_0(\boldsymbol{\rho}_+, \omega_-) = \int \frac{\mathrm{d}\omega_+}{2\pi} \int \frac{\mathrm{d}^2\mathbf{k}}{(2\pi)^2} W_{\mathcal{E}_0}(\boldsymbol{\rho}_+, \mathbf{k}, \omega_+, \omega_-) = \int \mathrm{d}t\, I_0(t) e^{i\omega_- t}, \tag{3.29}$$

and changing variables to $\mathbf{k}_- = \mathbf{k} - \mathbf{k}'$ and $\mathbf{k}_+ = (\mathbf{k} + \mathbf{k}')/2$ we have

$$\mathcal{P}_{2L}(\boldsymbol{\rho}_+, \omega_-) = \lambda_0^2 \mathcal{P}_0(\omega_-) e^{i\omega_- 2L/c} \int \frac{\mathrm{d}^2\mathbf{k}_+}{(2\pi)^2} \int \frac{\mathrm{d}^2\mathbf{k}_-}{(2\pi)^2} \mathcal{F}(\boldsymbol{\rho}_+ - cL\mathbf{k}_+/\omega_0)$$

$$\times\, e^{i\omega_- cL(2|\mathbf{k}_+|^2 + |\mathbf{k}_-|^2/2)/4\omega_0^2} W_P(\boldsymbol{\rho}_+ - cL(\mathbf{k}_+/2 + \mathbf{k}_-/4)/\omega_0, \mathbf{k}_-) 2\pi i c/\omega_- L, \tag{3.30}$$

where we have suppressed the $\boldsymbol{\rho}_+$ argument of $\mathcal{P}_0(\boldsymbol{\rho}_+, \omega_-)$ because that field has no such dependence for the plane-wave source we have assumed. We define a new function

$$G(\boldsymbol{\rho}, \omega_-) = \int \frac{\mathrm{d}^2\mathbf{k}_-}{(2\pi)^2} e^{i\omega_- cL|\mathbf{k}_-|^2/8\omega_0^2} W_P(-\boldsymbol{\rho}/2 - cL\mathbf{k}_-/4\omega_0, \mathbf{k}_-) 2\pi i c/\omega_- L. \tag{3.31}$$

56

With this definition we have

$$\mathcal{P}_{2L}(\boldsymbol{\rho}_+, \omega_-) = \lambda_0^2 \mathcal{P}_0(\omega_-) e^{i\omega_- 2L/c} \int \frac{\mathrm{d}^2\mathbf{k}_+}{(2\pi)^2} \, \mathcal{F}(\boldsymbol{\rho}_+ - cL\mathbf{k}_+/\omega_0)$$

$$\times \, G(-2\boldsymbol{\rho}_+ + cL\mathbf{k}_+/\omega_0, \omega_-) e^{i\omega_- cL|\mathbf{k}_+|^2/2\omega_0^2}. \tag{3.32}$$

Changing variables again, $\tilde{\boldsymbol{\rho}} = \boldsymbol{\rho}_+ - cL\mathbf{k}_+/\omega_0$, we get our final result

$$\mathcal{P}_{2L}(\boldsymbol{\rho}_+, \omega_-) = \mathcal{P}_0(\omega_-) e^{i\omega_- 2L/c} \int \mathrm{d}^2\tilde{\boldsymbol{\rho}} \, \mathcal{F}(\tilde{\boldsymbol{\rho}}) G(-\boldsymbol{\rho}_+ - \tilde{\boldsymbol{\rho}}, \omega_-) \frac{e^{i\omega_- |\boldsymbol{\rho}_+ - \tilde{\boldsymbol{\rho}}|^2/2cL}}{L^2}. \tag{3.33}$$

Owing to the Fresnel-propagation kernel in Eq. (3.33), this result is a superposition integral with image inversion, rather than a convolution integral with image inversion.

To get to a simpler result that will afford us insight into the advantage of occlusion-aided imaging, we shall assume that the initial laser illumination is monochromatic, i.e., the optical-frequency field that illuminates the $z = 0$ plane is $\mathrm{Re}[E_0(\boldsymbol{\rho}_0) e^{-i\omega_0 t}]$. In this unmodulated case we can use the usual spatial Wigner distribution, i.e.,

$$W_{E_0}(\boldsymbol{\rho}_+, \mathbf{k}) \equiv \int \mathrm{d}^2\boldsymbol{\rho}_- \, E_0(\boldsymbol{\rho}_+ + \boldsymbol{\rho}_-/2) E_0^*(\boldsymbol{\rho}_+ - \boldsymbol{\rho}_-/2) e^{-i\mathbf{k}\cdot\boldsymbol{\rho}_-}, \tag{3.34}$$

of the $z = 0$-plane field, in lieu of the TFSWD. The propagation primitives given earlier for the TFSWD all apply to the spatial Wigner distribution function for the unmodulated case with the only difference being that we set $\omega_- = 0$ in the Fresnel-diffraction primitive. Paralleling the development that led to Eq. (3.33) assuming that $E_0(\boldsymbol{\rho}_0) = \sqrt{I_0}$ is a constant, we get

$$\langle I_{2L}(\boldsymbol{\rho}_+) \rangle \equiv \langle |E_{2L}(\boldsymbol{\rho}_+)|^2 \rangle = I_0 \int \mathrm{d}^2\tilde{\boldsymbol{\rho}} \, \mathcal{F}(\tilde{\boldsymbol{\rho}}) G(-\boldsymbol{\rho}_+ - \tilde{\boldsymbol{\rho}}), \tag{3.35}$$

where

$$G(\boldsymbol{\rho}) \equiv \frac{\pi}{L^2} \int \frac{\mathrm{d}^2\mathbf{k}_-}{(2\pi)^2} \, W_P(-\boldsymbol{\rho}/2 - cL\mathbf{k}_-/4\omega_0, \mathbf{k}_-), \tag{3.36}$$

and we have used the evanescence cutoff, $|\mathbf{k}| \leq 2\pi/\lambda_0$, to justify replacing $\int \mathrm{d}^2\mathbf{k} \, I_0/(2\pi)^2$ with $\pi I_0/\lambda_0^2$.

Equations (3.35) and (3.36) show that this unmodulated case offers no spatial information about $\mathcal{F}(\boldsymbol{\rho})$ in the absence of an occluder, i.e., we get $G(\boldsymbol{\rho}) = \pi/L^2$ when $P(\boldsymbol{\rho}) = 1$, as seen previously in Eq. (2.22). To quantify the spatial information afforded by the presence of an occluder in the unmodulated scenario, we consider two simple cases: the Gaussian pinhole

$$P_{\mathrm{ph}}(\boldsymbol{\rho}) = \exp\left(-|\boldsymbol{\rho}|^2/2\rho_0^2\right), \tag{3.37}$$

and the Gaussian pinspeck,

$$P_{\mathrm{ps}}(\boldsymbol{\rho}) = 1 - \exp\left(-|\boldsymbol{\rho}|^2/2\rho_0^2\right), \tag{3.38}$$

where ρ_0 is the $e^{-1/2}$-attenuation radius of the Gaussian functions. The Gaussian-pinhole camera can be analyzed with far less complication than our approach to obtaining Eqs. (3.35) and (3.36), but (after accounting for image inversion) its point-spread function (psf) $G_{\mathrm{ph}}(\boldsymbol{\rho})$ is revealing. The Gaussian-pinspeck camera, on the other hand, is more relevant to the experiments of Xu *et al.* [11], but its psf $G_{\mathrm{ph}}(\boldsymbol{\rho})$ is more complicated. In both cases, however, the Gaussian functions involved enable us to get closed-form psf results.

For the Gaussian pinhole, we find that

$$G_{\mathrm{ph}}(\boldsymbol{\rho}) = \frac{\pi\Omega^2}{L^2(1+\Omega^2)} \exp\left[-\frac{\Omega^2}{1+\Omega^2}\frac{|\boldsymbol{\rho}|^2}{4\rho_0^2}\right], \tag{3.39}$$

where $k_0 \equiv \omega_0/c = 2\pi/\lambda_0$ is the wave number at the optical frequency and $\Omega \equiv 4k_0\rho_0^2/L$ is the Fresnel number for the pinhole's propagation geometry. The spatial resolution of $G_{\mathrm{ph}}(\boldsymbol{\rho})$ improves with decreasing ρ_0 when $\Omega > 1$, and degrades with decreasing ρ_0 when $\Omega < 1$. Thus the Gaussian pinhole's resolution-optimized psf,

$$G_{\mathrm{ph}}^{\mathrm{opt}}(\boldsymbol{\rho}) = \frac{\pi\exp(-\pi|\boldsymbol{\rho}|^2/\lambda_0 L)}{2L^2}, \tag{3.40}$$

is obtained when $\rho_0 = \sqrt{L/4k_0} = \sqrt{\lambda_0 L/8\pi}$. The optimized psf's spatial resolution—

taken to be its $e^{-\pi}$-attenuation radius—is then $\sqrt{\lambda_0 L}$, which is far superior to the $1.22\Delta\lambda L/D'$ for the unoccluded, modulated case governed by Eq. (2.36). For example, with $\lambda_0 = 1\,\mu\mathrm{m}$ and $L = 1\,\mathrm{m}$ the optimum spatial resolution of occlusion-aided unmodulated imaging is $1\,\mathrm{mm}$, while that of unoccluded modulated imaging, with $\Delta\lambda = 3\,\mathrm{cm}$ $(\Delta\omega/2\pi = 10\,\mathrm{GHz})$ and $D' = 10\,\mathrm{cm}$, is $37\,\mathrm{cm}$ at $L = 1\,\mathrm{m}$. For comparison with the Gaussian pinspeck's psf, it is worth noting that the Gaussian pinhole's psf maintains its Gaussian shape for all values of its Fresnel number Ω, with only its overall amplitude $G_{\mathrm{ph}}(\mathbf{0})$ and its spatial resolution $\rho_{\mathrm{res}}(\Omega) \equiv \sqrt{4\pi(1 + \Omega^2)}\,\rho_0/\Omega$ changing, i.e., we have that

$$G_{\mathrm{ph}}(\boldsymbol{\rho})/G_{\mathrm{ph}}(\mathbf{0}) = \exp[-\pi|\boldsymbol{\rho}^2|/\rho_{\mathrm{res}}^2(\Omega)], \tag{3.41}$$

for the Gaussian pinhole, as shown in Fig. 3-2(a).

For the Gaussian pinspeck, we get

$$G_{\mathrm{ps}}(\boldsymbol{\rho}) = \frac{\pi}{L^2}\left| 1 - \frac{\Omega}{\sqrt{1 + \Omega^2}}\exp\left[-\frac{\Omega}{1 + \Omega^2}\frac{|\boldsymbol{\rho}|^2}{8\rho_0^2}(\Omega - i) - i\tan^{-1}(1/\Omega) \right] \right|^2. \tag{3.42}$$

This psf is a bit more complicated than what we found for the Gaussian pinhole. Nevertheless, it shows the expected result for a pinspeck camera, viz., that the image-bearing part of the psf is embedded in a uniform background term whose presence creates photodetection shot noise that degrades signal-to-noise ratio. As was the case for the Gaussian pinhole, we see that optimum spatial resolution occurs when $\Omega = 1$, in which case we get

$$G_{\mathrm{ps}}^{\mathrm{opt}}(\boldsymbol{\rho}) = \frac{\pi}{L^2}\left| 1 - \frac{\exp(-\pi|\boldsymbol{\rho}|^2(1 - i)/2\lambda_0 L - i\pi/4)}{\sqrt{2}} \right|^2. \tag{3.43}$$

On the other hand, unlike the Gaussian pinhole's psf, the Gaussian pinspeck's psf does *not* preserve its shape as the Fresnel number is varied. This is illustrated in Fig. 3-2(b), where we have plotted $G_{\mathrm{ps}}(\boldsymbol{\rho})/G_{\mathrm{ps}}(\boldsymbol{\infty})$ versus $\boldsymbol{\rho}/\rho_{\mathrm{res}}(\Omega)$ for $\boldsymbol{\rho} = (x, 0)$ and $\Omega = 0.1, 1$, and 10, where $\rho_{\mathrm{res}}(\Omega)$ is the Gaussian pinhole's spatial resolution.

Note that in the near-field region, wherein $\Omega \gg 1$, Eq. (3.42) reduces to the

(a) Gaussian pinhole

(b) Gaussian pinspeck
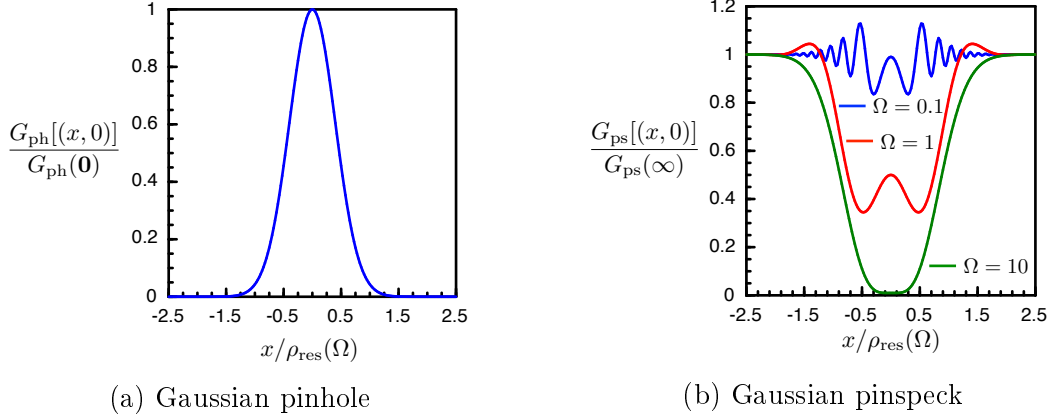
Figure 3-2: (a) Plot of $G_{\mathrm{ph}}(\boldsymbol{\rho})/G_{\mathrm{ph}}(\mathbf{0})$ for the Gaussian pinhole versus $\boldsymbol{\rho}/\rho_{\mathrm{res}}(\Omega)$ for $\boldsymbol{\rho} = (x, 0)$. (b) Plots of $G_{\mathrm{ps}}(\boldsymbol{\rho})/G_{\mathrm{ps}}(\infty)$ for the Gaussian pinspeck versus $\boldsymbol{\rho}/\rho_{\mathrm{res}}(\Omega)$ for $\boldsymbol{\rho} = (x, 0)$ and $\Omega = 0.1, 1$, and 10.

geometric-optics result,

$$G_{\mathrm{ps}}(\boldsymbol{\rho})/G_{\mathrm{ps}}(\infty) = [1 - \exp(-|\boldsymbol{\rho}|^2/8\rho_0^2)]^2, \tag{3.44}$$

which is analogous to the geometric-optics treatment used by Xu *et al.* [11] and Thrampoulidis *et al.* [12] for the hard-aperture, circular occluder

$$P(\boldsymbol{\rho}) = \mathrm{circ}(2\boldsymbol{\rho}/d) \equiv \begin{cases} 1, & \text{for } |\boldsymbol{\rho}| \leq d/2 \\ 0, & \text{otherwise.} \end{cases} \tag{3.45}$$

In fact, the geometric-optics approach can be shown to be valid more generally, as we will discuss in Sec. 3.4.

3.3   A General $\mathcal{P}$-Field Propagation Primitive

In this section, we use our results so far to derive the $\mathcal{P}$-field input-output relation for propagation through a transmissive paraxial system characterized by: transmission through a diffuser at plane $z = 0$, Fresnel diffraction over a distance L_1, transmission through a specular-plus-diffuser mask, and Fresnel diffraction over a distance L_2 such that the total distance propagated is $L_T = L_1 + L_2$. This scenario is depicted in Fig. 3-
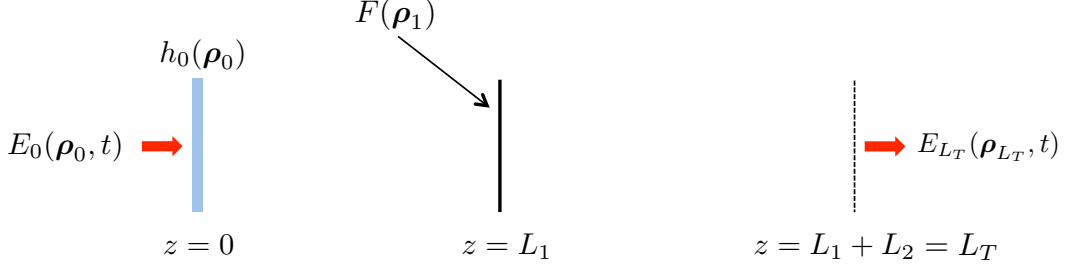
Figure 3-3: Fresnel propagation with an intervening specular-plus-diffuser mask.

3. This is the key component of our Sec. 3.2 analysis, and abstracting it suffices to analyze a broad variety of scenarios relevant to transmissive $\mathcal{P}$-field imaging. The Fresnel propagation primitive derived in Chapter 2 can be seen as the special case in which $F(\boldsymbol{\rho}) = 1$ for all $\boldsymbol{\rho}$. The unoccluded imaging scenario we analyzed there can be seen as a single instance of this primitive in which F is purely diffuse. The simplified occluded scenario analyzed in Sec. 3.2 can be seen as a concatenation of two of these primitives, both with strictly deterministic F functions and the first with $L_2 = 0$. Our treatment even allows for the deterministic portion of F to be complex valued, enabling analysis of propagation through phase masks. The thin lenses in Chapter 2 were modeled as phase masks but must be treated more carefully owing to the imposed phase shift being dependent on the underlying radiation frequency. One could, however, imagine deriving a new TFSWD primitive for propagation though frequency-dependent transmissivity masks, which would enable modifying Eq. (3.53) to deal with this even broader class of scenarios.

Starting at the input plane, the TFSWD after the initial diffuser is

$$W_{\mathcal{E}_0'}(\boldsymbol{\rho}_+, \mathbf{k}, \omega_+, \omega_-) = \lambda_0^2 \int \frac{\mathrm{d}^2 \mathbf{k}'}{(2\pi)^2} W_{\mathcal{E}_0}(\boldsymbol{\rho}_+, \mathbf{k}', \omega_+, \omega_-). \tag{3.46}$$

After L_1-distance Fresnel propagation, we have

$$W_{\mathcal{E}_{L_1}}(\boldsymbol{\rho}_+, \mathbf{k}, \omega_+, \omega_-) = \lambda_0^2 e^{i\frac{\omega_-}{c}L_1} e^{i\frac{\omega_-}{c}L_1 \frac{|\mathbf{k}|^2}{2k_0^2}} \int \frac{\mathrm{d}^2 \mathbf{k}'}{(2\pi)^2} W_{\mathcal{E}_0}(\boldsymbol{\rho}_+ - L_1 \mathbf{k}/k_0, \mathbf{k}', \omega_+, \omega_-), \tag{3.47}$$

where $k_0 = 2\pi/\lambda_0 = \omega_0/c$ is the wavenumber for the optical-frequency field. At $z = L_1$ the field encounters a transmissivity mask $F(\boldsymbol{\rho}_+)$ with both deterministic and

61

random (diffuse) components, resulting in

$$W_{\mathcal{E}_{L_1'}}(\boldsymbol{\rho}_+, \mathbf{k}, \omega_+, \omega_-) = \lambda_0^2 e^{i\frac{\omega_-}{c}L_1} \int \frac{\mathrm{d}^2 \mathbf{k}'}{(2\pi)^2} e^{i\frac{\omega_-}{c}L_1 \frac{|\mathbf{k}'|^2}{2k_0^2}} \left(W_{\langle F\rangle}(\boldsymbol{\rho}_+, \mathbf{k} - \mathbf{k}') + \lambda_0^2 \mathcal{F}(\boldsymbol{\rho}_+)\right)$$

$$\times \int \frac{\mathrm{d}^2 \mathbf{k}''}{(2\pi)^2} W_{\mathcal{E}_0}(\boldsymbol{\rho}_+ - L_1 \mathbf{k}'/k_0, \mathbf{k}'', \omega_+, \omega_-). \qquad (3.48)$$

Finally, after L_2-distance Fresnel propagation, the output TFSWD is given by

$$W_{\mathcal{E}_{L_T}}(\boldsymbol{\rho}_+, \mathbf{k}, \omega_+, \omega_-) = \lambda_0^2 e^{i\frac{\omega_-}{c}L_T} e^{i\frac{\omega_-}{c}L_2 \frac{|\mathbf{k}|^2}{2k_0^2}} \int \frac{\mathrm{d}^2 \mathbf{k}'}{(2\pi)^2} e^{i\frac{\omega_-}{c}L_1 \frac{|\mathbf{k}'|^2}{2k_0^2}} \int \frac{\mathrm{d}^2 \mathbf{k}''}{(2\pi)^2}$$

$$\times \left(W_{\langle F\rangle}(\boldsymbol{\rho}_+ - L_2 \mathbf{k}/k_0, \mathbf{k} - \mathbf{k}') + \lambda_0^2 \mathcal{F}(\boldsymbol{\rho}_+ - L_2 \mathbf{k}/k_0)\right)$$

$$\times W_{\mathcal{E}_0}(\boldsymbol{\rho}_+ - L_1 \mathbf{k}'/k_0 - L_2 \mathbf{k}/k_0, \mathbf{k}'', \omega_+, \omega_-). \qquad (3.49)$$

Now, to get a $\mathcal{P}$-field input-output relation we use Eq. (3.14) and, after rearranging terms, we have

$$\mathcal{P}_{L_T}(\boldsymbol{\rho}_+, \omega_-) = \lambda_0^2 e^{i\frac{\omega_-}{c}L_T} \int \frac{\mathrm{d}^2 \mathbf{k}}{(2\pi)^2} \int \frac{\mathrm{d}^2 \mathbf{k}'}{(2\pi)^2} e^{i\frac{\omega_-}{c} \frac{L_1|\mathbf{k}'|^2 + L_2|\mathbf{k}|^2}{2k_0^2}}$$

$$\times \left(W_{\langle F\rangle}(\boldsymbol{\rho}_+ - L_2 \mathbf{k}/k_0, \mathbf{k} - \mathbf{k}') + \lambda_0^2 \mathcal{F}(\boldsymbol{\rho}_+ - L_2 \mathbf{k}/k_0)\right)$$

$$\times \mathcal{P}_0(\boldsymbol{\rho}_+ - (L_1 \mathbf{k}' + L_2 \mathbf{k})/k_0, \omega_-). \qquad (3.50)$$

Changing variables to $\mathbf{k}_+ = (L_1 \mathbf{k}' + L_2 \mathbf{k})/L_T$ and $\mathbf{k}_- = \mathbf{k} - \mathbf{k}'$ yields

$$\mathcal{P}_{L_T}(\boldsymbol{\rho}_+, \omega_-)$$

$$= \lambda_0^2 e^{i\frac{\omega_-}{c}L_T} \int \frac{\mathrm{d}^2 \mathbf{k}_+}{(2\pi)^2} \int \frac{\mathrm{d}^2 \mathbf{k}_-}{(2\pi)^2} e^{i\frac{\omega_-}{c}L_T \frac{|\mathbf{k}_+|^2}{2k_0^2}} e^{i\frac{\omega_-}{c} \frac{L_1 L_2}{L_T} \frac{|\mathbf{k}_-|^2}{2k_0^2}} \mathcal{P}_0(\boldsymbol{\rho}_+ - L_T \mathbf{k}_+/k_0, \omega_-)$$

$$\left(W_{\langle F\rangle}\left(\boldsymbol{\rho}_+ - \frac{L_2 \mathbf{k}_+}{k_0} - \frac{L_1 L_2}{L_T} \frac{\mathbf{k}_-}{k_0}, \mathbf{k}_-\right) + \lambda_0^2 \mathcal{F}\left(\boldsymbol{\rho}_+ - \frac{L_2 \mathbf{k}_+}{k_0} - \frac{L_1 L_2}{L_T} \frac{\mathbf{k}_-}{k_0}\right)\right). \qquad (3.51)$$

Then, after changing variables to $\tilde{\boldsymbol{\rho}} = \boldsymbol{\rho}_+ - L_T \mathbf{k}_+/k_0$ and defining

$$
g(\boldsymbol{\rho}, \omega_-)
$$
$$
\equiv \int \frac{\mathrm{d}^2 \mathbf{k}_-}{(2\pi)^2} e^{i\frac{\omega_-}{c} \frac{L_1 L_2}{L_T} \frac{|\mathbf{k}_-|^2}{2k_0^2}} \left(W_{\langle F \rangle} \left(\boldsymbol{\rho} - \frac{L_1 L_2}{L_T} \frac{\mathbf{k}_-}{k_0}, \mathbf{k}_- \right) + \lambda_0^2 \mathcal{F} \left(\boldsymbol{\rho} - \frac{L_1 L_2}{L_T} \frac{\mathbf{k}_-}{k_0} \right) \right),
$$
(3.52)

we have

$$
\mathcal{P}_{L_T}(\boldsymbol{\rho}_+, \omega_-) = \frac{e^{i\omega_- L_T/c}}{L_T^2} \int \mathrm{d}^2 \tilde{\boldsymbol{\rho}}\, e^{i\frac{\omega_-}{2cL_T}|\boldsymbol{\rho}_+ - \tilde{\boldsymbol{\rho}}|^2} \mathcal{P}_0(\tilde{\boldsymbol{\rho}}, \omega_-) g((L_1\boldsymbol{\rho}_+ + L_2\tilde{\boldsymbol{\rho}})/L_T, \omega_-). \quad (3.53)
$$

Although Eq. (3.53) seems difficult to evaluate, in particular because of the cumbersome form of g, a much simpler form can be applied in the geometric-optics limit.

3.4   Geometric-Optics Limit for $\mathcal{P}$-Field Propagation Through Occluders
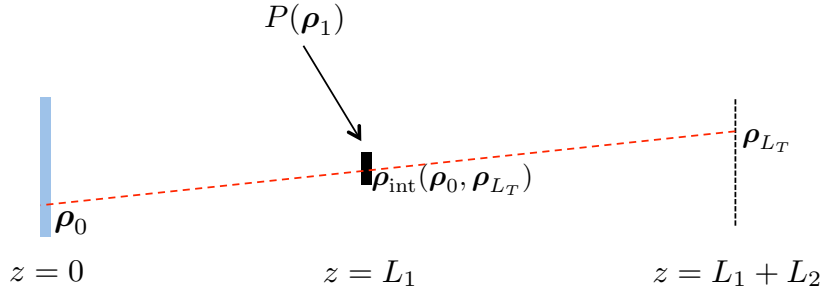
Figure 3-4: Fresnel propagation with an intervening occluder. A hypothetical ray in the geometric-optics sense is depicted as a dashed red line together with labels for the transverse spatial coordinates at which it intersects each of the planes of interest.

Consider the scenario from Sec. 3.3 with a deterministic occluder specified by $P(\boldsymbol{\rho})$, as depicted in Fig. 3-4. Geometric-optics intuition would suggest that the input $\mathcal{P}$ field at $\boldsymbol{\rho}_0$ would make a differential contribution

$$
\mathrm{d}^2 \boldsymbol{\rho}_0 \frac{1}{L^2} e^{i\frac{\omega_-}{c}(L_T + |\boldsymbol{\rho}_{L_T} - \boldsymbol{\rho}_0|^2/2L_T)} \mathcal{P}_0(\boldsymbol{\rho}_0, \omega_-) |P(\boldsymbol{\rho}_{\text{int}}(\boldsymbol{\rho}_0, \boldsymbol{\rho}_{L_T}))|^2 \tag{3.54}
$$

to the output $\mathcal{P}$ field at $\boldsymbol{\rho}_{L_T}$, where $\boldsymbol{\rho}_{\mathrm{int}}(\boldsymbol{\rho}_0, \boldsymbol{\rho}_{L_T})$ is the transverse position at which the ray connecting $\boldsymbol{\rho}_0$ to $\boldsymbol{\rho}_{L_T}$ intersects the $z = L_1$ plane, where the occluder lies, viz., $\boldsymbol{\rho}_{\mathrm{int}}(\boldsymbol{\rho}_0, \boldsymbol{\rho}_{L_T}) = \boldsymbol{\rho}_0 + L_1(\boldsymbol{\rho}_{L_T} - \boldsymbol{\rho}_0)/L_T = (L_1\boldsymbol{\rho}_{L_T} + L_2\boldsymbol{\rho}_0)/L_T$. The $\mathrm{d}^2\boldsymbol{\rho}_0$ term characterizes the differential area of the source contribution. The $1/L^2$ term accounts for the attenuation of the overall (paraxial) propagation. The $e^{i\frac{\omega_-}{c}(L_T + |\boldsymbol{\rho}_{L_T} - \boldsymbol{\rho}_0|^2/2L_T)}$ term accounts for the phase delay associated with the paraxial propagation distance. The $\mathcal{P}_0(\boldsymbol{\rho}_0, \omega_-)$ term is the source strength at the input location of interest, and the $|P(\boldsymbol{\rho}_{\mathrm{int}}(\boldsymbol{\rho}_0, \boldsymbol{\rho}_{L_T}))|^2$ term accounts for the attenuation this ray experiences due to the intervening occluder. Integrating over all differential contributions we have

$$\mathcal{P}_{L_T}(\boldsymbol{\rho}_{L_T}, \omega_-) = \frac{e^{i\omega_- L_T/c}}{L^2} \int \mathrm{d}^2\boldsymbol{\rho}_0 \, e^{i\frac{\omega_-}{2cL_T}|\boldsymbol{\rho}_{L_T} - \boldsymbol{\rho}_0|^2} \mathcal{P}_0(\boldsymbol{\rho}_0, \omega_-)|P((L_1\boldsymbol{\rho}_{L_T} + L_2\boldsymbol{\rho}_0)/L_T)|^2. \tag{3.55}$$

Does this intuition ever provide the right answer? In fact, this result is identical to Eq. (3.53) if $g(\boldsymbol{\rho}, \omega_-) = |P(\boldsymbol{\rho})|^2$. Examining Eq. (3.52), taking $\langle F \rangle = P$ and $\mathcal{F} = 0$, we see that it would suffice if we could neglect both the phase term in that integral and the $\mathbf{k}_-$-dependent offset to the spatial coordinate, as we would then have

$$g(\boldsymbol{\rho}, \omega_-) = \int \frac{\mathrm{d}^2\mathbf{k}_-}{(2\pi)^2} e^{i\frac{\omega_-}{c}\frac{L_1 L_2}{L_T}\frac{|\mathbf{k}_-|^2}{2k_0^2}} W_P(\boldsymbol{\rho} - (L_1 L_2/L_T)\mathbf{k}_-/k_0, \mathbf{k}_-) \tag{3.56}$$

$$= \int \frac{\mathrm{d}^2\mathbf{k}_-}{(2\pi)^2} W_P(\boldsymbol{\rho}, \mathbf{k}_-) \tag{3.57}$$

$$= |P(\boldsymbol{\rho})|^2 \tag{3.58}$$

by the properties of spatial Wigner distributions. This happens trivially when either L_1 or L_2 are identically zero. This also happens when λ_0 is taken to approach zero mathematically, as in traditional derivations of the geometric-optics limit. It is clearly nonphysical to have $\lambda_0 = 0$, though the limit is intended to represent the physical scenario of λ_0 being sufficiently small that diffraction can be neglected. These cases are more generally captured by the limit in which either of L_1/k_0 or L_2/k_0 approach zero. Still, it is unclear when this is physically meaningful outside of the trivial examples. These are dimensioned quantities that are likely to take finite values in

practice, and so it doesn't make sense to say they approach zero in an absolute sense—saying they become small compared to some other quantity with the same dimensions would be preferable. A more physically insightful argument, if not entirely formal here, can be made as follows. Suppose that the occluder in question has a finite spatial bandwidth $1/\sigma$ so that its spatial Wigner distribution $W_P(\boldsymbol{\rho}, \mathbf{k})$ is negligible for $|\mathbf{k}| > 1/\sigma$, as can be shown to be the case for Gaussian pinspecks and pinholes and can reasonably be assumed to hold true for most occluders of interest. In that case, taking $\mathbf{k}_-$ to be as large as possible, the conditions to neglect the two terms from above are

$$\frac{\omega_-}{c} \frac{L_1 L_2}{L_T} \frac{1}{2k_0^2 \sigma^2} \ll 1 \tag{3.59}$$

$$|\boldsymbol{\rho}| \gg \frac{L_1 L_2}{L_T \sigma k_0}. \tag{3.60}$$

Defining Fresnel numbers for this geometry, $\Omega_1 = \sigma^2 k_0 / L_1$ and $\Omega_2 = \sigma^2 k_0 / L_2$, these can be written as

$$\frac{\omega_-}{\omega_0} \ll \Omega_1 + \Omega_2 \tag{3.61}$$

$$|\boldsymbol{\rho}| \gg \frac{\sigma}{\Omega_1 + \Omega_2}. \tag{3.62}$$

In the first of these conditions, we already have $\omega_- \ll \omega_0$, so it can easily be fulfilled by taking either of the Fresnel numbers to be at least 1. The second condition then implies that g will behave like $|P|^2$ except for at worst a small region in the center which can be made arbitrarily small by making either Fresnel number sufficiently large. Considering the case in which the effect of the occlusion is primarily multiplicative instead of convolutional, i.e., $L_1 \gg L_2$, this predicts that deviations from geometric optics visible at the output plane will be confined to a small region about the center, which is evocative of the well-known Poisson's spot [23]. The Fresnel numbers can be made large enough so that this region is much smaller than the resolution limit of whatever measuring optics are being used, at which point the geometric-optics description is functionally accurate. When g acts convolutionally, the deviations from

geometric optics are confined to the center of a convolution kernel and thus may show up anywhere in the final result, but it seems their impact should be minimal in the high-Fresnel-number limit.

An alternative approach to the second condition is to consider when the spatial offset term is small compared to the spatial feature size of W_P. Having taken the spatial bandwidth to be $1/\sigma$, this feature size is σ. The resulting condition reads $\Omega_1 + \Omega_2 \gg 1$, which is consistent with the above analysis.

Chapter 4

Nonparaxial Propagation

In this chapter, we extend the paraxial $\mathcal{P}$-field propagation framework we've developed so far to nonparaxial operation. In particular, we replace our assumption of Fresnel diffraction of the underlying field with that of Rayleigh–Sommerfeld diffraction. First we derive, from the complex-field-envelope diffraction integral, the appropriate $\mathcal{P}$-field propagation integral for free space propagation following a diffuser. Then we show the equivalent implication for the propagation of the diffuser-averaged STA irradiance. Next we review the paraxial free-space propagation primitive for the TFSWD and show its equivalent formulation in terms of the 6D light field. Using geometric intuition we propose a replacement procedure for the paraxial terms of the primitive with nonparaxial equivalents. This provides us with a proposed nonparaxial free-space propagation primitive for the 6D light field. We verify this proposal implies the correct behavior for the diffuser-averaged STA irradiance, and then show its equivalent formulation in terms of the TFSWD. We provide a more formal derivation of the TFSWD equivalent that is valid under certain conditions. Finally, we provide a set of differential equations that govern the TFSWD more generally.

4.1 Rayleigh–Sommerfeld $\mathcal{P}$-Field Propagation

Our development of a Rayleigh–Sommerfeld propagation primitive for the $\mathcal{P}$ field parallels that for Fresnel propagation as in Chapter 2. We consider propagation first

through a diffuser and then through a free-space distance L_1, as depicted in the first portion of Fig. 2-1. The key difference in the derivation is to replace Eq. (2.3)—the Fresnel diffraction integral for the complex field envelope—with the Rayleigh–Sommerfeld diffraction integral [24]

$$\mathcal{E}_1(\boldsymbol{\rho}_1,\omega) = \int \mathrm{d}^2\boldsymbol{\rho}_0\, \mathcal{E}_0'(\boldsymbol{\rho}_0,\omega) \frac{\exp\left[i(\omega_0+\omega)\sqrt{L_1^2+|\boldsymbol{\rho}_1-\boldsymbol{\rho}_0|^2}/c\right](\omega_0+\omega)L_1}{i2\pi c(L_1^2+|\boldsymbol{\rho}_1-\boldsymbol{\rho}_0|^2)}, \quad (4.1)$$

where we have substituted $L_1/\sqrt{L_1^2+|\boldsymbol{\rho}_1-\boldsymbol{\rho}_0|^2}$ in place of the cosine obliquity factor. The derivation then proceeds as in the Fresnel case, utilizing the same assumptions regarding the diffuser statistics and modulation frequency:

$$\mathcal{P}_1(\boldsymbol{\rho}_1,\omega_-) = \int \frac{\mathrm{d}\omega_+}{2\pi} \langle \mathcal{E}_1(\boldsymbol{\rho}_1,\omega_++\omega_-/2)\mathcal{E}_1^*(\boldsymbol{\rho}_1,\omega_+-\omega_-/2)\rangle \qquad (4.2)$$

$$= \int \frac{\mathrm{d}\omega_+}{2\pi} \int \mathrm{d}^2\boldsymbol{\rho}_0 \int \mathrm{d}^2\tilde{\boldsymbol{\rho}}_0\, \mathcal{E}_0(\boldsymbol{\rho}_0,\omega_++\omega_-/2)\mathcal{E}_0^*(\tilde{\boldsymbol{\rho}}_0,\omega_+-\omega_-/2)$$

$$\times \langle e^{i\frac{\omega_0}{c}(h_0(\boldsymbol{\rho}_0)-h_0(\tilde{\boldsymbol{\rho}}_0))}\rangle \frac{\omega_0^2 e^{i\frac{\omega_0+\omega_++\omega_-/2}{c}\sqrt{L_1^2+|\boldsymbol{\rho}_1-\boldsymbol{\rho}_0|^2}-i\frac{\omega_0+\omega_+-\omega_-/2}{c}\sqrt{L_1^2+|\boldsymbol{\rho}_1-\tilde{\boldsymbol{\rho}}_0|^2}}}{(2\pi c)^2(L_1^2+|\boldsymbol{\rho}_1-\boldsymbol{\rho}_0|^2)(L_1^2+|\boldsymbol{\rho}_1-\tilde{\boldsymbol{\rho}}_0|^2)}$$

$$(4.3)$$

$$= \int \mathrm{d}^2\boldsymbol{\rho}_0\, \mathcal{P}_0(\boldsymbol{\rho}_0,\omega_-) \frac{\exp\left(i\omega_-\sqrt{L_1^2+|\boldsymbol{\rho}_1-\boldsymbol{\rho}_0|^2}/c\right)L_1^2}{(L_1^2+|\boldsymbol{\rho}_1-\boldsymbol{\rho}_0|^2)^2}. \qquad (4.4)$$

Now, remembering that the $\mathcal{P}$ field is the Fourier transform of the diffuser-averaged STA irradiance, so that

$$\langle I_1(\boldsymbol{\rho}_1,t)\rangle \equiv \langle |E_1(\boldsymbol{\rho}_1,t)|^2\rangle = \int \frac{\mathrm{d}\omega_-}{2\pi} \mathcal{P}_1(\boldsymbol{\rho}_1,\omega_-)e^{-i\omega_-t}, \qquad (4.5)$$

it immediately follows that

$$\langle I_1(\boldsymbol{\rho}_1,t)\rangle = \int \mathrm{d}^2\boldsymbol{\rho}_0\, I_0\left(\boldsymbol{\rho}_0,t-\sqrt{L_1^2+|\boldsymbol{\rho}_1-\boldsymbol{\rho}_0|^2}/c\right)L_1^2/(L_1^2+|\boldsymbol{\rho}_1-\boldsymbol{\rho}_0|^2)^2, \quad (4.6)$$

where

$$I_0(\boldsymbol{\rho}_0,t) \equiv |E_0(\boldsymbol{\rho}_0,t)|^2 \qquad (4.7)$$

68

is the STA irradiance illuminating the $z = 0$ plane and $\langle I_1(\boldsymbol{\rho}_1, t) \rangle$ is the diffuser-averaged STA irradiance illuminating the $z = L_1$ plane. This accords perfectly with our intuition: each point on the diffuser contributes incoherently to the final irradiance, is delayed according to the distance it travels, is scaled by the inverse square of said distance, and is scaled by the cosine-squared obliquity factor.

4.2 The 6D Light Field and TFSWD

Next we turn our attention to the TFSWD. As discussed in Chapter 3, the $\mathcal{P}$ field alone will not suffice to analyze all of the scenarios of interest to NLoS imaging. The TFSWD by contrast provides a complete characterization of the relevant properties of the underlying field, and so it is desirable to have propagation primitives for it from which $\mathcal{P}$-field input-output relations can be constructed. Fortunately, most of the TFSWD primitives derived in Chapter 3 suffice for nonparaxial propagation as they only describe interactions that occur at a single plane. So, to extend the TFSWD formalism to the nonparaxial regime, it suffices for us to derive a Rayleigh–Sommerfeld propagation primitive to replace the previously-derived Fresnel propagation primitive, which for convenience we reproduce here:

$$W_{\mathcal{E}_1}(\boldsymbol{\rho}_+, \mathbf{k}, \omega_+, \omega_-) = W_{\mathcal{E}_{0_+}}(\boldsymbol{\rho}_+ - L_1 \mathbf{k}/k_0, \mathbf{k}, \omega_+, \omega_-) e^{i \frac{\omega_- L_1}{c} \left(1 + \frac{|\mathbf{k}|^2}{2k_0^2}\right)}, \tag{4.8}$$

where $k_0 = \omega_0/c$ is the wavenumber of the optical carrier. In terms of the 6D light field—i.e., the inverse Fourier transform of the TFSWD, similar to the time-dependent specific irradiance albeit augmented by a frequency coordinate—we have that

$$I_1(\boldsymbol{\rho}_+, \mathbf{s}, \omega_+, t) = \frac{1}{\lambda_0^2} \int \frac{\mathrm{d}\omega_-}{2\pi} W_{\mathcal{E}_1}(\boldsymbol{\rho}_+, 2\pi \mathbf{s}/\lambda_0, \omega_+, \omega_-) e^{-i\omega_- t} \tag{4.9}$$

$$= \frac{1}{\lambda_0^2} \int \frac{\mathrm{d}\omega_-}{2\pi} W_{\mathcal{E}_{0_+}}(\boldsymbol{\rho}_+ - L_1 \mathbf{s}, k_0 \mathbf{s}, \omega_+, \omega_-) e^{i \frac{\omega_- L_1}{c} \left(1 + \frac{|\mathbf{s}|^2}{2}\right)} e^{-i\omega_- t} \tag{4.10}$$

$$= I_{0_+}(\boldsymbol{\rho}_+ - L_1 \mathbf{s}, \mathbf{s}, \omega_+, t - L_1/c - |\mathbf{s}|^2 L_1/2c), \tag{4.11}$$

where $\mathbf{s} = 2\pi \mathbf{k}/\lambda_0 = \mathbf{k}/k_0$ is the transverse component of the unit vector pointing in the nominal propagation direction.

Let's take a moment to interpret this result for the 6D light field. If we take the first argument of I_{0_+} to be a transverse spatial coordinate for the initial plane $\boldsymbol{\rho}_0$, we see that $\mathbf{s} = (\boldsymbol{\rho}_+ - \boldsymbol{\rho}_0)/L_1$. This makes perfect sense in the paraxial regime: $\mathbf{s}$ represents the transverse component of the propagation direction, and this says that it equals the ratio of the transverse spatial offset to the approximate propagation distance. So, the spatial profile of the 6D light field is merely sheared according to the propagation direction. The propagation direction itself doesn't change, nor does the frequency, and we see that the time dependence is delayed by an effective distance $L_1 + |\mathbf{s}|^2 L_1/2 = L_1 + |\boldsymbol{\rho}_+ - \boldsymbol{\rho}_0|^2/2L_1$, which is precisely the paraxial propagation distance. This interpretation confirms that the 6D light field formalizes the ray optics intuition for light propagation.

This interpretation also immediately exposes the imprecision of the Fresnel approach. Neither L_1, as in the denominator of our interpretation for $\mathbf{s}$, nor $L_1 + |\boldsymbol{\rho}_+ - \boldsymbol{\rho}_0|^2/2L_1$, as in the time delay, are really the propagation distance of such a hypothetical ray. That distance would be $\sqrt{L_1^2 + |\boldsymbol{\rho}_+ - \boldsymbol{\rho}_0|^2}$. Say then we take $\mathbf{s} = (\boldsymbol{\rho}_+ - \boldsymbol{\rho}_0)/\sqrt{L_1^2 + |\boldsymbol{\rho}_+ - \boldsymbol{\rho}_0|^2}$. What then would $\boldsymbol{\rho}_0$ be? We have that

$$\boldsymbol{\rho}_+ - \boldsymbol{\rho}_0 = \mathbf{s}\sqrt{L_1^2 + |\boldsymbol{\rho}_+ - \boldsymbol{\rho}_0|^2} \tag{4.12}$$

$$|\boldsymbol{\rho}_+ - \boldsymbol{\rho}_0|^2 = |\mathbf{s}|^2 L_1^2 + |\mathbf{s}|^2 |\boldsymbol{\rho}_+ - \boldsymbol{\rho}_0|^2 \tag{4.13}$$

$$|\boldsymbol{\rho}_+ - \boldsymbol{\rho}_0|^2 = \frac{|\mathbf{s}|^2 L_1^2}{1 - |\mathbf{s}|^2} \tag{4.14}$$

$$\boldsymbol{\rho}_0 = \boldsymbol{\rho}_+ + \frac{L_1 \mathbf{s}}{\sqrt{1 - |\mathbf{s}|^2}}, \tag{4.15}$$

where Eq. (4.15) follows from substituting Eq. (4.14) into Eq. (4.12). Equation (4.15) makes perfect, intuitive sense. Define θ to be the angle the propagation direction makes with the z axis, as depicted in Fig. 4-1. Trigonometrically, L_1 represents the adjacent propagation distance. Since the propagation direction is a unit vector, and $\mathbf{s}$ is its transverse component, we have $|\mathbf{s}| = \sin\theta$, $\sqrt{1 - |\mathbf{s}|^2} = \cos\theta$, and

$|\mathbf{s}| / \sqrt{1 - |\mathbf{s}|^2} = \tan\theta$, opposite over adjacent. So $L_1 |\mathbf{s}| / \sqrt{1 - |\mathbf{s}|^2}$ is the opposite, i.e., transverse, propagation distance. Removing the absolute value from $\mathbf{s}$ gives the vector-valued transverse displacement in the correct direction. The total propagation distance is then $\sqrt{L_1^2 + |\boldsymbol{\rho}_+ - \boldsymbol{\rho}_0|^2} = L_1 / \sqrt{1 - |\mathbf{s}|^2}$.
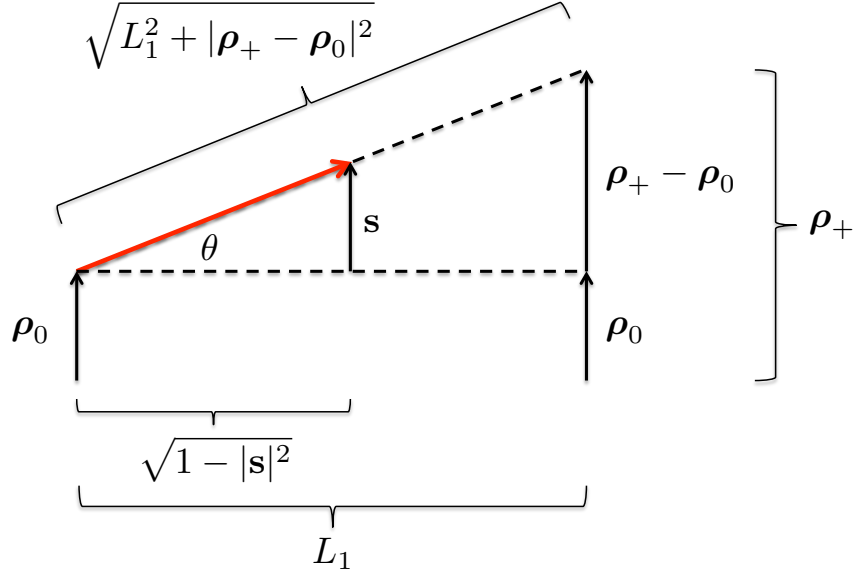
Figure 4-1: Trigonometry for Rayleigh–Sommerfeld propagation of the 6D light field. The red arrow represents a unit vector pointing in the propagation direction of a hypothetical ray propagating from $(\boldsymbol{\rho}_0, 0)$ to $(\boldsymbol{\rho}_+, L_1)$.

Taking the appropriately corrected values for the transverse offset and the total time delay, this suggests that the correct free-space propagation primitive for the 6D light field is

$$I_1(\boldsymbol{\rho}_+, \mathbf{s}, \omega_+, t) = I_{0_+}\left(\boldsymbol{\rho}_+ - \frac{L_1 \mathbf{s}}{\sqrt{1 - |\mathbf{s}|^2}}, \mathbf{s}, \omega_+, t - \frac{L_1}{c\sqrt{1 - |\mathbf{s}|^2}}\right). \tag{4.16}$$

To check this result, we can ask what it implies about the propagation of the diffuser-averaged STA irradiance following a diffuser. It follows from the diffuser TFSWD primitive that

$$I_{0_+}(\boldsymbol{\rho}_+, \mathbf{s}, \omega_+, t) = \int d^2\mathbf{s}' \, I_0(\boldsymbol{\rho}_+, \mathbf{s}', \omega_+, t). \tag{4.17}$$

So, we have that

$$\langle I_1(\boldsymbol{\rho}_1, t) \rangle = \int \frac{d\omega_+}{2\pi} \int d^2 \mathbf{s} \, I_1(\boldsymbol{\rho}_1, \mathbf{s}, \omega_+, t) \tag{4.18}$$

$$= \int \frac{d\omega_+}{2\pi} \int d^2 \mathbf{s} \int d^2 \mathbf{s}' \, I_0 \left(\boldsymbol{\rho}_1 - \frac{L_1 \mathbf{s}}{\sqrt{1 - |\mathbf{s}|^2}}, \mathbf{s}', \omega_+, t - \frac{L_1}{c\sqrt{1 - |\mathbf{s}|^2}} \right). \tag{4.19}$$

Now we change variables so that $\mathbf{s} = (\boldsymbol{\rho}_1 - \boldsymbol{\rho}_0) / \sqrt{L_1^2 + |\boldsymbol{\rho}_1 - \boldsymbol{\rho}_0|^2}$. Computing the appropriate Jacobian determinant we find $\int d^2 \mathbf{s} = \int d^2 \boldsymbol{\rho}_0 \, L_1^2 / \left(L_1^2 + |\boldsymbol{\rho}_1 - \boldsymbol{\rho}_0|^2 \right)^2$, so we now have

$$\langle I_1(\boldsymbol{\rho}_1, t) \rangle = \int \frac{d\omega_+}{2\pi} \int d^2 \boldsymbol{\rho}_0 \, \frac{L_1^2}{\left(L_1^2 + |\boldsymbol{\rho}_1 - \boldsymbol{\rho}_0|^2 \right)^2}$$

$$\times \int d^2 \mathbf{s}' \, I_0 \left(\boldsymbol{\rho}_0, \mathbf{s}', \omega_+, t - \frac{\sqrt{L_1^2 + |\boldsymbol{\rho}_1 - \boldsymbol{\rho}_0|^2}}{c} \right) \tag{4.20}$$

$$= \int d^2 \boldsymbol{\rho}_0 \, I_0 \left(\boldsymbol{\rho}_0, t - \frac{\sqrt{L_1^2 + |\boldsymbol{\rho}_1 - \boldsymbol{\rho}_0|^2}}{c} \right) \frac{L_1^2}{\left(L_1^2 + |\boldsymbol{\rho}_1 - \boldsymbol{\rho}_0|^2 \right)^2}, \tag{4.21}$$

which is precisely our result for Rayleigh–Sommerfeld propagation of the diffuser-averaged STA irradiance after a diffuser. Moreover, note how the cosine-squared obliquity factor is automatically accounted for by this approach.

Inspired by this success, we propose the equivalent nonparaxial free-space propagation primitive for the TFSWD

$$W_{\mathcal{E}_1}(\boldsymbol{\rho}_+, \mathbf{k}, \omega_+, \omega_-) = W_{\mathcal{E}_{0_+}} \left(\boldsymbol{\rho}_+ - \frac{L_1 \mathbf{k}}{\sqrt{k_0^2 - |\mathbf{k}|^2}}, \mathbf{k}, \omega_+, \omega_- \right) e^{\frac{i\omega_- L_1 k_0}{c\sqrt{k_0^2 - |\mathbf{k}|^2}}}, \tag{4.22}$$

which can be obtained by Fourier transforming Eq. (4.16). In principle, one would hope to derive this formula directly from substituting the Rayleigh–Sommerfeld diffraction integral for the complex field envelope into the definition of the TFSWD. Unfortunately, we find this approach untenable. However, this result can be derived under

special circumstances by adapting a technique developed elsewhere for the traditional optical Wigner distribution [21].

We shift our attention to the angular spectrum representation, whereby the optical field is expressed as a superposition of propagating plane waves and all evanescent components are ignored. The implications for the complex field envelope $\mathcal{E}(\boldsymbol{\rho}, \omega)$ and its propagation are summarized by the equations below, which define a new quantity $\tilde{\mathcal{E}}(\mathbf{s}, \omega)$, its angular spectrum:

$$\mathcal{E}_z(\boldsymbol{\rho}, \omega) = \int \frac{\mathrm{d}^2 \mathbf{s}}{(2\pi)^2} \, \tilde{\mathcal{E}}_z(\mathbf{s}, \omega) \exp\left(i\left(\omega_0 + \omega\right) \boldsymbol{\rho} \cdot \mathbf{s}/c\right) \tag{4.23}$$

$$\tilde{\mathcal{E}}_z(\mathbf{s}, \omega) = \tilde{\mathcal{E}}_0(\mathbf{s}, \omega) \exp\left(i\left(\omega_0 + \omega\right) z s_z(\mathbf{s})/c\right), \tag{4.24}$$

where $|\mathbf{s}| < 1$ and $s_z(\mathbf{s}) = \sqrt{1 - |\mathbf{s}|^2}$. Substituting these into the definition of the TFSWD we have that

$$
\begin{aligned}
&W_z(\boldsymbol{\rho}_+, \mathbf{k}, \omega_+, \omega_-) \\
&= \int \mathrm{d}^2 \boldsymbol{\rho}_- \, e^{-i\mathbf{k}\cdot\boldsymbol{\rho}_-} \langle \mathcal{E}_z(\boldsymbol{\rho}_+ + \boldsymbol{\rho}_-/2, \omega_+ + \omega_-/2) \mathcal{E}_z^*(\boldsymbol{\rho}_+ - \boldsymbol{\rho}_-/2, \omega_+ - \omega_-/2) \rangle \quad (4.25) \\
&= \int \mathrm{d}^2 \boldsymbol{\rho}_- \int \frac{\mathrm{d}^2 \mathbf{s}_1}{(2\pi)^2} \int \frac{\mathrm{d}^2 \mathbf{s}_2}{(2\pi)^2} \, e^{-i\mathbf{k}\cdot\boldsymbol{\rho}_-} e^{i\frac{\omega_0 + \omega_+ + \omega_-/2}{c}\left((\boldsymbol{\rho}_+ + \boldsymbol{\rho}_-/2)\cdot\mathbf{s}_1 + z s_z(\mathbf{s}_1)\right)} \\
&\quad \times e^{-i\frac{\omega_0 + \omega_+ - \omega_-/2}{c}\left((\boldsymbol{\rho}_+ - \boldsymbol{\rho}_-/2)\cdot\mathbf{s}_2 + z s_z(\mathbf{s}_2)\right)} \langle \tilde{\mathcal{E}}_0(\mathbf{s}_1, \omega_+ + \omega_-/2) \tilde{\mathcal{E}}_0^*(\mathbf{s}_2, \omega_+ - \omega_-/2) \rangle. \quad (4.26)
\end{aligned}
$$

Now we switch to sum and difference coordinates, $\mathbf{s}_+ = (\mathbf{s}_1 + \mathbf{s}_2)/2$ and $\mathbf{s}_- = \mathbf{s}_1 - \mathbf{s}_2$. After reorganizing some terms we have that

$$
\begin{aligned}
W_z(\boldsymbol{\rho}_+, \mathbf{k}, \omega_+, \omega_-) = \int \mathrm{d}^2 \boldsymbol{\rho}_- \int \frac{\mathrm{d}^2 \mathbf{s}_+}{(2\pi)^2} \int \frac{\mathrm{d}^2 \mathbf{s}_-}{(2\pi)^2} \\
\times e^{i\boldsymbol{\rho}_-\cdot\left(\frac{\omega_0 + \omega_+}{c}\mathbf{s}_+ + \frac{\omega_-}{4c}\mathbf{s}_- - \mathbf{k}\right)} e^{i\boldsymbol{\rho}_+\cdot\left(\frac{\omega_0 + \omega_+}{c}\mathbf{s}_- + \frac{\omega_-}{c}\mathbf{s}_+\right)} \\
\times e^{i\frac{\omega_0 + \omega_+}{c} z(s_z(\mathbf{s}_+ + \mathbf{s}_-/2) - s_z(\mathbf{s}_+ + \mathbf{s}_-/2))} e^{i\frac{\omega_-}{c} z(s_z(\mathbf{s}_+ + \mathbf{s}_-/2) + s_z(\mathbf{s}_+ - \mathbf{s}_-/2))/2} \\
\times \langle \tilde{\mathcal{E}}_0(\mathbf{s}_+ + \mathbf{s}_-/2, \omega_+ + \omega_-/2) \tilde{\mathcal{E}}_0^*(\mathbf{s}_+ - \mathbf{s}_-/2, \omega_+ - \omega_-/2) \rangle.
\end{aligned}
$$

$$\tag{4.27}$$

Performing the $\boldsymbol{\rho}_-$ integral yields

$$\int \mathrm{d}^2\boldsymbol{\rho}_- \, e^{i\boldsymbol{\rho}_-\cdot\left(\frac{\omega_0+\omega_+}{c}\mathbf{s}_+ + \frac{\omega_-}{4c}\mathbf{s}_- - \mathbf{k}\right)} = \left(\frac{c}{\omega_0+\omega_+}\right)^2 \delta\left(\mathbf{s}_+ - \frac{c\mathbf{k}}{\omega_0+\omega_+} + \frac{\omega_-\mathbf{s}_-}{4\left(\omega_0+\omega_+\right)}\right),$$

(4.28)

where the last term in the argument of the delta function can be ignored owing to our quasimonochromatic assumption. Defining $\tilde{k}_0 \equiv (\omega_0+\omega_+)/c$ and completing the $\mathbf{s}_+$ integral then gives us

$$W_z(\boldsymbol{\rho}_+, \mathbf{k}, \omega_+, \omega_-) = \int \frac{\mathrm{d}^2\mathbf{s}_-}{(2\pi)^2} \, e^{i\boldsymbol{\rho}_+\cdot\left(\tilde{k}_0\mathbf{s}_- + \omega_-\mathbf{k}/c\tilde{k}_0\right)} e^{i\tilde{k}_0 z\left(s_z(\mathbf{k}/\tilde{k}_0+\mathbf{s}_-/2) - s_z(\mathbf{k}/\tilde{k}_0+\mathbf{s}_-/2)\right)}$$

$$\times \, e^{i\frac{\omega_-}{c}z\left(s_z(\mathbf{k}/\tilde{k}_0+\mathbf{s}_-/2) + s_z(\mathbf{k}/\tilde{k}_0-\mathbf{s}_-/2)\right)/2}$$

$$\times \, \langle \tilde{\mathcal{E}}_0(\mathbf{k}/\tilde{k}_0 + \mathbf{s}_-/2, \omega_+ + \omega_-/2)\tilde{\mathcal{E}}_0^*(\mathbf{k}/\tilde{k}_0 - \mathbf{s}_-/2, \omega_+ - \omega_-/2)\rangle.$$

(4.29)

Next we introduce the first of our two key assumptions. Consider the case in which the angular-spectrum correlation $\langle \tilde{\mathcal{E}}_0(\mathbf{s}_+ + \mathbf{s}_-/2, \omega_+ + \omega_-/2)\tilde{\mathcal{E}}_0^*(\mathbf{s}_+ - \mathbf{s}_-/2, \omega_+ - \omega_-/2)\rangle$ differs from 0 only when $|\mathbf{s}_-| \ll 1$. In that case, we can approximate s_z by its first-order expansion in $\mathbf{s}_-$, i.e., $s_z(\mathbf{s}_+ \pm \mathbf{s}_-/2) \approx s_z(\mathbf{s}_+) \pm \nabla s_z(\mathbf{s}_+) \cdot \mathbf{s}_-/2$ where $\nabla s_z(\mathbf{s}_+) = -\mathbf{s}_+/s_z(\mathbf{s}_+)$. Using this approximation and reorganizing terms we now have

$$W_z(\boldsymbol{\rho}_+, \mathbf{k}, \omega_+, \omega_-) = \int \frac{\mathrm{d}^2\mathbf{s}_-}{(2\pi)^2} \, \frac{1}{\tilde{k}_0^2} e^{i\tilde{k}_0\mathbf{s}_-\cdot\left(z\nabla s_z(\mathbf{k}/\tilde{k}_0)+\boldsymbol{\rho}_+\right)} e^{i\frac{\omega_-}{c}\left(zs_z(\mathbf{k}/\tilde{k}_0)+\boldsymbol{\rho}_+\cdot\mathbf{k}/\tilde{k}_0\right)}$$

$$\langle \tilde{\mathcal{E}}_0(\mathbf{k}/\tilde{k}_0 + \mathbf{s}_-/2, \omega_+ + \omega_-/2)\tilde{\mathcal{E}}_0^*(\mathbf{k}/\tilde{k}_0 - \mathbf{s}_-/2, \omega_+ - \omega_-/2)\rangle.$$

(4.30)

Because the angular spectrum can be obtained from the complex field envelope via

$$\tilde{\mathcal{E}}_0(\mathbf{s}, \omega) = \int \mathrm{d}^2\boldsymbol{\rho} \, \mathcal{E}_0(\boldsymbol{\rho}, \omega) \exp\left(-i\left(\omega_0 + \omega\right)\boldsymbol{\rho}\cdot\mathbf{s}/c\right),$$

(4.31)

we find that

$$
W_z(\boldsymbol{\rho}_+,\mathbf{k},\omega_+,\omega_-) = \int \mathrm{d}^2\tilde{\boldsymbol{\rho}}_1 \int \mathrm{d}^2\tilde{\boldsymbol{\rho}}_2 \int \frac{\mathrm{d}^2\mathbf{s}_-}{(2\pi)^2} \frac{1}{\tilde{k}_0^2}
$$

$$
e^{i\tilde{k}_0\mathbf{s}_-\cdot\left(z\nabla s_z(\mathbf{k}/\tilde{k}_0)+\boldsymbol{\rho}_+\right)} e^{i\frac{\omega_-}{c}\left(zs_z(\mathbf{k}/\tilde{k}_0)+\boldsymbol{\rho}_+\cdot\mathbf{k}/\tilde{k}_0\right)}
$$

$$
e^{-i\frac{\omega_0+\omega_++\omega_-/2}{c}\tilde{\boldsymbol{\rho}}_1\cdot\left(\mathbf{k}/\tilde{k}_0+\mathbf{s}_-/2\right)} e^{i\frac{\omega_0+\omega_+-\omega_-/2}{c}\tilde{\boldsymbol{\rho}}_2\cdot\left(\mathbf{k}/\tilde{k}_0-\mathbf{s}_-/2\right)}
$$

$$
\langle \mathcal{E}_0(\tilde{\boldsymbol{\rho}}_1,\omega_++\omega_-/2)\mathcal{E}_0^*(\tilde{\boldsymbol{\rho}}_2,\omega_+-\omega_-/2)\rangle. \tag{4.32}
$$

Changing to sum and difference coordinates again and reorganizing terms we have

$$
W_z(\boldsymbol{\rho}_+,\mathbf{k},\omega_+,\omega_-) = \int \mathrm{d}^2\tilde{\boldsymbol{\rho}}_+ \int \mathrm{d}^2\tilde{\boldsymbol{\rho}}_- \int \frac{\mathrm{d}^2\mathbf{s}_-}{(2\pi)^2} \frac{1}{\tilde{k}_0^2} e^{-i\tilde{k}_0\mathbf{s}_-\cdot\left(\tilde{\boldsymbol{\rho}}_+-\left(\boldsymbol{\rho}_++z\nabla s_z(\mathbf{k}/\tilde{k}_0)\right)+\frac{\omega_-\tilde{\boldsymbol{\rho}}_-}{4(\omega_0+\omega_+)}\right)}
$$

$$
\times\, e^{-i\mathbf{k}\cdot\tilde{\boldsymbol{\rho}}_-} e^{i\frac{\omega_-}{c}\left(zs_z(\mathbf{k}/\tilde{k}_0)+(\boldsymbol{\rho}_+-\tilde{\boldsymbol{\rho}}_+)\cdot\mathbf{k}/\tilde{k}_0\right)}
$$

$$
\times\, \langle \mathcal{E}_0(\tilde{\boldsymbol{\rho}}_++\tilde{\boldsymbol{\rho}}_-/2,\omega_++\omega_-/2)\mathcal{E}_0^*(\tilde{\boldsymbol{\rho}}_+-\tilde{\boldsymbol{\rho}}_-/2,\omega_+-\omega_-/2)\rangle. \tag{4.33}
$$

Now the $\mathbf{s}_-$ integral can be done to yield a delta function:

$$
\int \frac{\mathrm{d}^2\mathbf{s}_-}{(2\pi)^2} \frac{1}{\tilde{k}_0^2} e^{-i\tilde{k}_0\mathbf{s}_-\cdot\left(\tilde{\boldsymbol{\rho}}_+-\left(\boldsymbol{\rho}_++z\nabla s_z(\mathbf{k}/\tilde{k}_0)\right)+\frac{\omega_-\tilde{\boldsymbol{\rho}}_-}{4(\omega_0+\omega_+)}\right)}
$$

$$
= \delta\left(\tilde{\boldsymbol{\rho}}_+-\left(\boldsymbol{\rho}_++z\nabla s_z(\mathbf{k}/\tilde{k}_0)\right)+\frac{\omega_-\tilde{\boldsymbol{\rho}}_-}{4(\omega_0+\omega_+)}\right). \tag{4.34}
$$

Here we introduce the second of our key assumptions, that the complex-field-envelope correlation $\langle \mathcal{E}_0(\boldsymbol{\rho}_++\boldsymbol{\rho}_-/2,\omega_++\omega_-/2)\mathcal{E}_0^*(\boldsymbol{\rho}_+-\boldsymbol{\rho}_-/2,\omega_+-\omega_-/2)\rangle$ differs significantly from 0 only for $\left|\boldsymbol{\rho}_-\right|$ small enough that our quasimonochromatic assumption suffices for us to neglect the final term in the argument of the preceding delta function. In this case, we carry out the $\tilde{\boldsymbol{\rho}}_+$ with the help of the delta function and get

$$
W_z(\boldsymbol{\rho}_+,\mathbf{k},\omega_+,\omega_-) = \int \mathrm{d}^2\tilde{\boldsymbol{\rho}}_-\, e^{-i\mathbf{k}\cdot\tilde{\boldsymbol{\rho}}_-} e^{i\frac{\omega_-z}{c}\left(s_z(\mathbf{k}/\tilde{k}_0)+\nabla s_z(\mathbf{k}/\tilde{k}_0)\cdot\mathbf{k}/\tilde{k}_0\right)}
$$

$$
\times\, \langle \mathcal{E}_0(\boldsymbol{\rho}_++z\nabla s_z(\mathbf{k}/\tilde{k}_0)+\tilde{\boldsymbol{\rho}}_-/2,\omega_++\omega_-/2)
$$

$$
\times\, \mathcal{E}_0^*(\boldsymbol{\rho}_++z\nabla s_z(\mathbf{k}/\tilde{k}_0)-\tilde{\boldsymbol{\rho}}_-/2,\omega_+-\omega_-/2)\rangle \tag{4.35}
$$

$$=W_0(\boldsymbol{\rho}_+ + z\nabla s_z(\mathbf{k}/\tilde{k}_0), \mathbf{k}, \omega_+, \omega_-)e^{i\frac{\omega_- z}{c}\left(s_z(\mathbf{k}/\tilde{k}_0) + \nabla s_z(\mathbf{k}/\tilde{k}_0)\cdot\mathbf{k}/\tilde{k}_0\right)} \tag{4.36}$$

$$=W_0\left(\boldsymbol{\rho}_+ - \frac{z\mathbf{k}}{\sqrt{\tilde{k}_0^2 - |\mathbf{k}|^2}}, \mathbf{k}, \omega_+, \omega_-\right)e^{i\frac{\omega_- z}{c}\left(\frac{\sqrt{\tilde{k}_0^2 - |\mathbf{k}|^2}}{\tilde{k}_0} + \frac{|\mathbf{k}|^2}{\tilde{k}_0\sqrt{\tilde{k}_0^2 - |\mathbf{k}|^2}}\right)} \tag{4.37}$$

$$=W_0\left(\boldsymbol{\rho}_+ - \frac{z\mathbf{k}}{\sqrt{\tilde{k}_0^2 - |\mathbf{k}|^2}}, \mathbf{k}, \omega_+, \omega_-\right)e^{i\frac{\omega_- z\tilde{k}_0}{c\sqrt{\tilde{k}_0^2 - |\mathbf{k}|^2}}}. \tag{4.38}$$

Finally, we make use of our quasimonochromatic assumption one more time to say $\tilde{k}_0 \approx k_0$ which gives us the final result we desire:

$$W_z(\boldsymbol{\rho}_+, \mathbf{k}, \omega_+, \omega_-) = W_0\left(\boldsymbol{\rho}_+ - \frac{z\mathbf{k}}{\sqrt{k_0^2 - |\mathbf{k}|^2}}, \mathbf{k}, \omega_+, \omega_-\right)e^{i\frac{\omega_- z k_0}{c\sqrt{k_0^2 - |\mathbf{k}|^2}}}. \tag{4.39}$$

Before moving on, let's take a moment to consider our two assumptions more carefully: (1) that $\langle\tilde{\mathcal{E}}_0(\mathbf{s}_1, \omega_1)\tilde{\mathcal{E}}_0^*(\mathbf{s}_2, \omega_2)\rangle$ differs from 0 only when $|\mathbf{s}_-| \ll 1$ and (2) that $\langle\mathcal{E}_0(\boldsymbol{\rho}_1, \omega_1)\mathcal{E}_0^*(\boldsymbol{\rho}_2, \omega_2)\rangle$ differs significantly from 0 only for $|\boldsymbol{\rho}_-|$ small enough that $\left|\boldsymbol{\rho}_+ - z\mathbf{k}/\sqrt{k_0^2 - |\mathbf{k}|^2}\right| \gg \omega_-|\boldsymbol{\rho}_-|/4(\omega_0 + \omega_+)$. First let's assume that the complex field envelopes at the $z = 0$ plane can be factored into spatial and temporal components:

$$E_0(\boldsymbol{\rho}_0, t) = E_0(\boldsymbol{\rho}_0)S(t) \tag{4.40}$$

$$\mathcal{E}_0(\boldsymbol{\rho}_0, \omega) = E_0(\boldsymbol{\rho}_0)\mathcal{S}(\omega). \tag{4.41}$$

Then we have that

$$\langle\tilde{\mathcal{E}}_0(\mathbf{s}_1, \omega_1)\tilde{\mathcal{E}}_0^*(\mathbf{s}_2, \omega_2)\rangle = \mathcal{S}(\omega_1)\mathcal{S}^*(\omega_2)\int d^2\boldsymbol{\rho}_+ \int d^2\boldsymbol{\rho}_- \langle E_0(\boldsymbol{\rho}_1)E_0^*(\boldsymbol{\rho}_2)\rangle$$
$$\times e^{-i\boldsymbol{\rho}_+\cdot(\omega_-\mathbf{s}_+ + (\omega_0 + \omega_+)\mathbf{s}_-)/c}e^{-i\boldsymbol{\rho}_-\cdot(\omega_-\mathbf{s}_-/4 + (\omega_0 + \omega_+)\mathbf{s}_+)/c} \tag{4.42}$$

and

$$\langle\mathcal{E}_0(\boldsymbol{\rho}_1, \omega_1)\mathcal{E}_0^*(\boldsymbol{\rho}_2, \omega_2)\rangle = \mathcal{S}(\omega_1)\mathcal{S}^*(\omega_2)\langle E_0(\boldsymbol{\rho}_1)E_0^*(\boldsymbol{\rho}_2)\rangle. \tag{4.43}$$

76

Next, let's assume that the spatial correlation function has a Schell model, viz.,

$$\langle E_0(\boldsymbol{\rho}_1)E_0^*(\boldsymbol{\rho}_2)\rangle = I(\boldsymbol{\rho}_+)R(\boldsymbol{\rho}_-), \tag{4.44}$$

for some functions $I(\cdot)$ and $R(\cdot)$.[1] In this case,

$$
\begin{aligned}
\langle \tilde{\mathcal{E}}_0(\mathbf{s}_1,\omega_1)\tilde{\mathcal{E}}_0^*(\mathbf{s}_2,\omega_2)\rangle =& \mathcal{S}(\omega_1)\mathcal{S}^*(\omega_2)\int \mathrm{d}^2\boldsymbol{\rho}_+ \int \mathrm{d}^2\boldsymbol{\rho}_-\, I(\boldsymbol{\rho}_+)R(\boldsymbol{\rho}_-)\\
&\times e^{-i\boldsymbol{\rho}_+\cdot(\omega_-\mathbf{s}_+ +(\omega_0+\omega_+)\mathbf{s}_-)/c}e^{-i\boldsymbol{\rho}_-\cdot(\omega_-\mathbf{s}_-/4+(\omega_0+\omega_+)\mathbf{s}_+)/c} \tag{4.45}\\
=& \mathcal{S}(\omega_1)\mathcal{S}^*(\omega_2)\mathcal{I}((\omega_-\mathbf{s}_+ +(\omega_0+\omega_+)\mathbf{s}_-)/c)\\
&\times \mathcal{R}((\omega_-\mathbf{s}_-/4+(\omega_0+\omega_+)\mathbf{s}_+)/c) \tag{4.46}\\
\approx& \mathcal{S}(\omega_1)\mathcal{S}^*(\omega_2)\mathcal{I}(k_0\mathbf{s}_-)\mathcal{R}(k_0\mathbf{s}_+), \tag{4.47}
\end{aligned}
$$

where

$$\mathcal{I}(\mathbf{k}) \equiv \int \mathrm{d}^2\boldsymbol{\rho}\, I(\boldsymbol{\rho})\exp(-i\boldsymbol{\rho}\cdot\mathbf{k}) \tag{4.48}$$

$$\mathcal{R}(\mathbf{k}) \equiv \int \mathrm{d}^2\boldsymbol{\rho}\, R(\boldsymbol{\rho})\exp(-i\boldsymbol{\rho}\cdot\mathbf{k}). \tag{4.49}$$

So, our two assumptions then amount to (1) $I(\boldsymbol{\rho}_+)$ being broad enough and (2) $R(\boldsymbol{\rho}_-)$ being narrow enough. A pure diffuser at the $z = 0$ plane, as we've analyzed in Chapters 2 and 3, will trivially suffice for our second assumption, as $R(\boldsymbol{\rho}_-) \propto \delta(\boldsymbol{\rho}_-)$ for that case, but propagation from such planes is already characterized by our $\mathcal{P}$ field primitive in Eq. (4.4). However, these assumptions allow us to consider propagation from planes containing partial diffusers with relaxed homogeneity assumptions and larger coherence lengths. To gain further insight, let's assume that the Schell model is Gaussian so that

$$I(\boldsymbol{\rho}_+) = A_I \exp(-\left|\boldsymbol{\rho}_+ - \boldsymbol{\mu}\right|^2/2\rho_I^2) \tag{4.50}$$

$$R(\boldsymbol{\rho}_-) = A_R \exp(-\left|\boldsymbol{\rho}_-\right|^2/2\rho_R^2), \tag{4.51}$$

---

[1]Not to be confused with other uses of I and R in this thesis. Though we will generally have $I(\boldsymbol{\rho}_+) = \langle I_0(\boldsymbol{\rho}_+)\rangle = \langle |E_0(\boldsymbol{\rho}_+)|^2\rangle$ and hence $R(\mathbf{0}) = 1$.

where A_I and A_R represent scaling coefficients, ρ_I and ρ_R represent the functions' $e^{-1/2}$-attenuation radii, and we permit $I(\boldsymbol{\rho}_+)$ to have a nonzero spatial offset $\boldsymbol{\mu}$. Then we have that

$$\mathcal{I}(\mathbf{k}) = 2\pi\rho_I^2 A_I \exp(-\rho_I^2 \left|\mathbf{k}\right|^2/2 - i\mathbf{k}\cdot\boldsymbol{\mu}) \tag{4.52}$$

$$\mathcal{R}(\mathbf{k}) = 2\pi\rho_R^2 A_R \exp(-\rho_R^2 \left|\mathbf{k}\right|^2/2). \tag{4.53}$$

From these expressions it follows that our assumptions will be satisfied if (1) $\rho_I \gg \lambda_0$ and (2) $\left|\boldsymbol{\rho}_+ - z\mathbf{k}/\sqrt{k_0^2 - \left|\mathbf{k}\right|^2}\right| \gg \omega_-\rho_R/\omega_0$. The first constraint will be easily satisfied for any $z = 0$-plane configuration of interest. The second constraint is more interesting. Recalling our geometric interpretation, it follows from Eq. (4.15) that $\left|\boldsymbol{\rho}_+ - z\mathbf{k}/\sqrt{k_0^2 - \left|\mathbf{k}\right|^2}\right| = \left|\boldsymbol{\rho}_0\right|$. Thus, the second constraint is $\left|\boldsymbol{\rho}_0\right| \gg \omega_-\rho_R/\omega_0$, which implies that Eq. (4.39) is valid except for rays—i.e., $\boldsymbol{\rho}_+,\mathbf{k}$ pairs—that originate at the $z = 0$ plane within a small radius about the origin. For the case of a partial diffuser, this radius is given by a small fraction of its coherence length. Taking $\omega_-/2\pi = 10\,\mathrm{GHz}$ and $\lambda_0 = 532\,\mathrm{nm}$, we have $\omega_-/\omega_0 \approx 1.8 \times 10^{-5}$. So, our results should be valid for any rays that originate outside $\left|\boldsymbol{\rho}_0\right| \gg \rho_R/56000$.

We can also handle propagation from occluders within this framework. In particular, let's consider the Gaussian pinhole occluder analyzed in Chapter 3, modified to permit a nonzero spatial offset:

$$P_{\mathrm{ph}}(\boldsymbol{\rho}) = \exp\left(-\left|\boldsymbol{\rho} - \boldsymbol{\mu}\right|^2/2\rho_0^2\right). \tag{4.54}$$

Assuming that this occluder is broadly illuminated, such that we can ignore the spatial profile of the incident field, it is not hard to see that the correlation function at the plane of the occluder will have a Gaussian Schell model with $I(\boldsymbol{\rho}_+) = \exp(-\left|\boldsymbol{\rho}_+ - \boldsymbol{\mu}\right|^2/\rho_0^2)$ and $R(\boldsymbol{\rho}_-) = \exp(-\left|\boldsymbol{\rho}_-\right|^2/4\rho_0^2)$. In this case, $\rho_I = \rho_0/\sqrt{2}$ and $\rho_R = \sqrt{2}\rho_0$. Our first constraint will be easily satisfied by any physical pinhole, and second constraint will be satisfied by $\left|\boldsymbol{\rho}_0\right| \geq \rho_0/2000$. For realistic pinholes, it seems that the second constraint should be easily satisfied by almost all rays of interest.

Even if we take $\rho_0 = 1\,\text{m}$, our result should be valid for all rays propagating from outside $|\boldsymbol{\rho}_0| \geq 0.5\,\text{mm}$. For a pinhole centered about the origin, the excluded rays comprise a very small fraction of the most significant ones. Curiously, this constraint doesn't depend on $\boldsymbol{\mu}$, and so the issue is of even less concern for off-center pinholes, whose most significant rays will originate from a region displaced from the origin.

4.3   The Helmholtz Equation

From this chapter's last result, it seems that even to reproduce the nonparaxial Rayleigh–Sommerfeld behavior of the $\mathcal{P}$ field from the TFSWD requires copious approximation. So, it is worth considering whether a more generally applicable description of TFSWD behavior is obtainable. In terms of the underlying positive-frequency optical field—which, in the time domain we'll denote $U_z(\boldsymbol{\rho}, t) = E_z(\boldsymbol{\rho}, t)e^{-i\omega_0 t}$—the most general description we can provide is the wave equation:

$$\left(\nabla_{\boldsymbol{\rho}}^2 + \partial_z^2 - \frac{1}{c^2}\partial_t^2 \right) U_z(\boldsymbol{\rho}, t) = 0, \tag{4.55}$$

where $\nabla_{\boldsymbol{\rho}}$ is the 2D gradient with respect to the transverse coordinate $\boldsymbol{\rho}$ and $\nabla_{\boldsymbol{\rho}}^2$ is the associated Laplacian. The implication for the frequency-domain complex field envelope then is that it satisfies the Helmholtz equation with a frequency offset:

$$\left(\nabla_{\boldsymbol{\rho}}^2 + \partial_z^2 - \frac{(\omega_0 + \omega)^2}{c^2} \right) \mathcal{E}_z(\boldsymbol{\rho}, \omega) = 0. \tag{4.56}$$

One might expect that the Rayleigh–Sommerfeld diffraction integral, Eq. (4.1), would satisfy this equation with $\mathcal{E}_0$ as a boundary condition. However, it does not, as the Rayleigh–Sommerfeld integral as we've presented it is in fact an approximation of a

more formal diffraction integral we'll call the Rayleigh diffraction integral [25]:

$$\mathcal{E}_z(\boldsymbol{\rho}_1, \omega) = \int d^2\boldsymbol{\rho}_0 \, \mathcal{E}_0(\boldsymbol{\rho}_0, \omega) \frac{1}{2\pi} \left(\frac{1}{\sqrt{z^2 + |\boldsymbol{\rho}_1 - \boldsymbol{\rho}_0|^2}} - i\frac{\omega_0 + \omega}{c} \right)$$
$$\times \frac{z}{z^2 + |\boldsymbol{\rho}_1 - \boldsymbol{\rho}_0|^2} e^{i\frac{\omega_0 + \omega}{c}\sqrt{z^2 + |\boldsymbol{\rho}_1 - \boldsymbol{\rho}_0|^2}}, \tag{4.57}$$

which, as it turns out, *does* satisfy Eq (4.56) with $\mathcal{E}_0$ as a boundary condition. Equation (4.1) is obtained from Eq. (4.57) in the limit of $\lambda_0 \ll z$, which is trivially true for any scenario of practical interest. Though more formally valid, the Rayleigh diffraction integral is even more cumbersome to manage, and it doesn't lend itself as readily to intuitive physical interpretation. Accordingly, we are at a loss to find an appropriate TFSWD primitive for its behavior. Nevertheless, it is not hard to see that the implied $\mathcal{P}$-field post-diffuser propagation is given by

$$\mathcal{P}_1(\boldsymbol{\rho}_1, \omega_-) = \int d^2\boldsymbol{\rho}_0 \, \mathcal{P}_0(\boldsymbol{\rho}_0, \omega_-) \left(1 + \frac{\lambda_0^2}{4\pi^2 \left(L_1^2 + |\boldsymbol{\rho}_1 - \boldsymbol{\rho}_0|^2 \right)} \right)$$
$$\times \frac{L_1^2}{\left(L_1^2 + |\boldsymbol{\rho}_1 - \boldsymbol{\rho}_0|^2 \right)^2} e^{i\frac{\omega_-}{c}\sqrt{L_1^2 + |\boldsymbol{\rho}_1 - \boldsymbol{\rho}_0|^2}}, \tag{4.58}$$

which implies the following result for the diffuser-averaged STA irradiance,

$$\langle I_1(\boldsymbol{\rho}_1, t) \rangle = \int d^2\boldsymbol{\rho}_0 \, I_0 \left(\boldsymbol{\rho}_0, t - \sqrt{L_1^2 + |\boldsymbol{\rho}_1 - \boldsymbol{\rho}_0|^2} \right) \left(1 + \frac{\lambda_0^2}{4\pi^2 \left(L_1^2 + |\boldsymbol{\rho}_1 - \boldsymbol{\rho}_0|^2 \right)} \right)$$
$$\times \frac{L_1^2}{\left(L_1^2 + |\boldsymbol{\rho}_1 - \boldsymbol{\rho}_0|^2 \right)^2}. \tag{4.59}$$

Despite it not being clear what the appropriate TFSWD free-space propagation primitive would be, we *can* characterize its behavior quite generally. First we note that the TFSWD is a Fourier transform of the complex-field-envelope correlation $\langle \mathcal{E}_z(\boldsymbol{\rho}_1, \omega_1)\mathcal{E}_z^*(\boldsymbol{\rho}_2, \omega_2) \rangle$. It is not hard to see that this correlation must obey two Helmholtz equations, one for the first transverse spatial coordinate and frequency, and another for the second pair of coordinates. Following from the chain rule and the fact that the Fourier transform of 0 is 0, we can easily derive a pair of differential

equations for the TFSWD which can be summarized by

$$\left(\frac{1}{4}\nabla^2_{\boldsymbol{\rho}_+} + \partial^2_z \pm i\mathbf{k}\cdot\nabla_{\boldsymbol{\rho}_+} + \frac{(\omega_0 + \omega_+ \pm \omega_-/2)^2}{c^2} - |\mathbf{k}|^2\right)W_z(\boldsymbol{\rho}_+, \mathbf{k}, \omega_+, \omega_-) = 0.$$
(4.60)

If we define an angular spectrum for the TFSWD by Fourier transforming its transverse spatial coordinate, i.e.

$$\tilde{W}_z(\mathbf{k}_+, \mathbf{k}_-, \omega_+, \omega_-) = \int \mathrm{d}^2\boldsymbol{\rho}_+\, W_z(\boldsymbol{\rho}_+, \mathbf{k}_+, \omega_+, \omega_-)e^{-i\mathbf{k}_-\cdot\boldsymbol{\rho}_+},$$
(4.61)

then the equivalent pair of equations are given by

$$\left(\partial^2_z + \frac{(\omega_0 + \omega_+ \pm \omega_-/2)^2}{c^2} - |\mathbf{k}_+ \pm \mathbf{k}_-/2|^2\right)\tilde{W}_z(\mathbf{k}_+, \mathbf{k}_-, \omega_+, \omega_-) = 0.$$
(4.62)

Not surprisingly, Eq. (4.22) doesn't satisfy these differential equations. After all, it only suffices to reproduce the approximate Rayleigh–Sommerfeld behavior of the $\mathcal{P}$ field and not the full Rayleigh-diffraction behavior. However, it seems unlikely that any clean propagation primitive will satisfy these equations exactly, as all our propagation derivations thus far have made copious use of the quasimonochromatic assumption, which is of course not captured by the Helmholtz equation. Still, it is intellectually satisfying to have a general description in terms of such differential equations, and they may prove useful for some presently unforeseen circumstances.

Chapter 5

Speckle

In this chapter, we provide an analysis of speckle as it pertains to the task of NLoS active imaging. We begin by considering the continuous-wave (CW) case and analyze transmissive third-order speckle—i.e., speckled speckled speckle—as an analog to the received irradiance in 3-diffuse-bounce NLoS imaging scenarios. There, using Gaussian assumptions for statistics and transverse spatial profiles, we are able to find closed-form results that indicate the final speckle can be as bad as seven times stronger than ordinary[1] (first-order) speckle. However, we also find that this speckle can be mitigated by a time-averaging illumination technique or naturally minimized by the geometry of the problem. We conclude that the geometry of expected NLoS imaging scenarios in fact reduces the strength of third-order speckle to that of ordinary speckle and that these remaining variations will be automatically averaged out by any reasonable detector area.

Next we move on to consider speckle as it impacts modulated illumination in the $\mathcal{P}$-field framework. Here, our analysis is limited to first-order speckle. We establish a bound on the zero-frequency-component speckle for space-time factorable illumination patterns, finding that such speckle at worst is of ordinary strength and in general is weaker than that. We then remark on the result of Teichman [27] for factorable, single-frequency modulation, which finds the modulation-frequency-component speckle to

---

[1]Ordinary speckle is characterized by the STA irradiance measured at a single location and moment in time being exponentially distributed with $\mathrm{var}(I(\boldsymbol{\rho},t)) = \langle I(\boldsymbol{\rho},t)\rangle^2$ [26]. This is the speckle associated with propagation through a single pure diffuser.

be stronger than ordinary speckle in general. We analyze a concrete test signal in an effectively single-frequency-modulation limiting case that establishes the applicability of Teichman's result to our $\mathcal{P}$-field framework and demonstrates our bound for the zero-frequency component. Using realistic values for NLoS imaging scenarios, we conclude that the speckle enhancement effect reported by Teichman is likely to be minimal in practice.

Moving further, we analyze the first-order-speckle size for the modulated case and find it to be quite small, suggesting that speckle in the modulated case may well be integrated out by the spatial extent of a realistic detector. Moreover, we find this size to be comparable with the first-order-speckle size of the CW case, and note that if this correspondence holds in the multi-bounce cases that the situation is likely to only improve for typical geometries.

To demonstrate the impact of detector spatial integration, we analyze the implied photodetection statistics. We demonstrate that speckle arises as an excess noise term beyond the fundamental shot-noise limit, which has the effect of bounding the maximum attainable signal-to-noise ratio. For typical parameter values, we find this upper bound to be generous, and thus conclude that the impact of speckle is unlikely to be significant in practice.

Finally, to push past our first-bounce restriction on analyzing the modulated case, we consider the small-reflector limit as an alternative geometry. In this limit we find it possible to derive the full irradiance distribution together with all its moments for nth-order speckle in the CW case and both the first and second moments of the modulated-component nth-order speckle of quasimonochromatic illumination in the modulated case.

5.1 Continuous-Wave Speckle

We begin by considering multi-bounce speckle for CW illumination. As before we use a paraxial, transmissive geometry, with, for simplicity, no albedo pattern on the hidden plane. The geometry for our speckle analysis is depicted in Fig. 5-1. Illumination
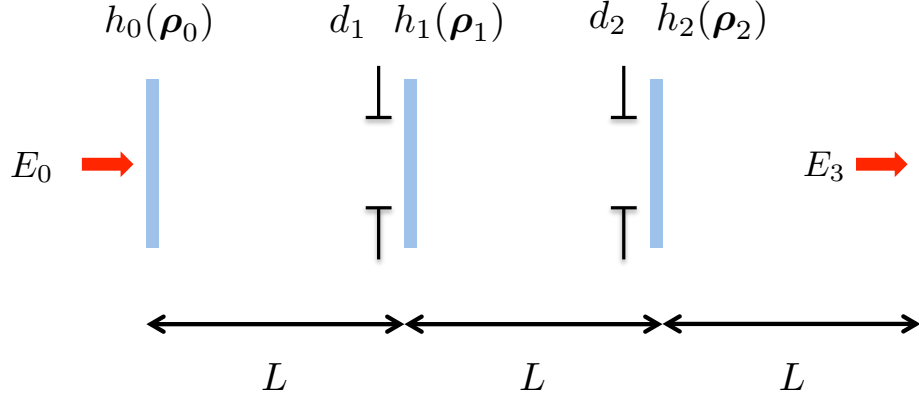
Figure 5-1: Geometry for multi-bounce speckle analysis. Thin blue rectangles represent idealized, thin diffusers. The black frames in front of the diffusers in planes 1 and 2 represent Gaussian pupils that capture the essence of the target and wall sizes respectively. The dashed line represents the detection plane.

is incident at plane 0 which contains a diffuser representing the first bounce at the visible wall in the standard NLoS imaging configuration. Plane 1 contains a diffuser and a Gaussian pupil, representing light reflecting off a finite-sized diffuse object in the hidden scene. Plane 2 contains another diffuser and Gaussian pupil pair, representing the final, return bounce off the visible wall. Here the pupil represents the finite size of the wall and allows us to obtain closed-form, convergent results in the paraxial regime. This aperture is not necessary at plane 0 as we assume the initial illumination will be self-limited to within the boundaries of the wall. Finally, plane 3 represents the standoff from the visible wall to the detection plane.

We assume a Gaussian illumination pattern at the first plane whose field envelope is given by

$$E_0(\boldsymbol{\rho}_0; \boldsymbol{\mu}) = \sqrt{8P/\pi d_0^2} \exp\left(-4\left|\boldsymbol{\rho}_0 - \boldsymbol{\mu}\right|^2 / d_0^2\right),\tag{5.1}$$

where d_0 represents the transverse extent of the illumination and $\boldsymbol{\mu}$ denotes a transverse offset that will prove useful later. Following Fresnel propagation, the field envelope at plane 1 is given by

$$E_1(\boldsymbol{\rho}_1; \boldsymbol{\mu}) = \frac{e^{i\frac{\omega_0 L}{c}}}{i\lambda_0 L} \int \mathrm{d}^2\boldsymbol{\rho}_0 \, E_0(\boldsymbol{\rho}_0; \boldsymbol{\mu}) e^{i\frac{\omega_0}{2cL}\left|\boldsymbol{\rho}_1 - \boldsymbol{\rho}_0\right|^2} e^{i\frac{\omega_0}{c}h_0(\boldsymbol{\rho}_0)},\tag{5.2}$$

and the field envelope at plane 2 is given by

$$E_2(\boldsymbol{\rho}_2; \boldsymbol{\mu}) = \frac{e^{i\frac{\omega_0 L}{c}}}{i\lambda_0 L} \int \mathrm{d}^2\boldsymbol{\rho}_1 \, E_1(\boldsymbol{\rho}_1; \boldsymbol{\mu}) e^{i\frac{\omega_0}{2cL}|\boldsymbol{\rho}_2 - \boldsymbol{\rho}_1|^2} e^{i\frac{\omega_0}{c}h_1(\boldsymbol{\rho}_1)} e^{-\frac{4}{d_1^2}|\boldsymbol{\rho}_1|^2}, \qquad (5.3)$$

where we've included the effect of the pupil at plane 1. The envelope at plane 3 can be obtained by a similar formula, changing subscripts as appropriate. We make the same diffuser assumptions as in Chapter 2, so that the diffuser thicknesses at planes 0, 1, and 2 are statistically independent Gaussian random processes satisfying

$$\langle e^{i\omega_0(h_k(\boldsymbol{\rho}) - h_k(\tilde{\boldsymbol{\rho}}))/c} \rangle = \lambda_0^2 \delta(\boldsymbol{\rho} - \tilde{\boldsymbol{\rho}}) \qquad (5.4)$$

$$\langle e^{i\omega_0(h_k(\boldsymbol{\rho}) + h_k(\tilde{\boldsymbol{\rho}}))/c} \rangle = 0, \qquad (5.5)$$

for $k = 0, 1, 2$.

From the preceding field envelopes, the STA irradiances can be obtained from $I(\boldsymbol{\rho}) = |E(\boldsymbol{\rho})|^2$. Averaged over the diffusers, these irradiances incident at each plane are given by

$$\langle I_1(\boldsymbol{\rho}_1; \boldsymbol{\mu}) \rangle_0 = \langle I_1 \rangle \equiv \frac{P}{L^2} \qquad (5.6)$$

$$\langle I_2(\boldsymbol{\rho}_2; \boldsymbol{\mu}) \rangle_{0,1} = \langle I_2 \rangle \equiv \frac{\pi d_1^2}{8L^2} \langle I_1 \rangle \qquad (5.7)$$

$$\langle I_3(\boldsymbol{\rho}_3; \boldsymbol{\mu}) \rangle_{0,1,2} = \langle I_3 \rangle \equiv \frac{\pi d_2^2}{8L^2} \langle I_2 \rangle, \qquad (5.8)$$

where angle brackets represent ensemble averaging over the diffusers at the planes listed in the subscripts. Note that these diffuser-averaged irradiances do not depend on the transverse spatial coordinates, nor the offset of the initial illumination.

Since we take the diffuser phase shifts—$e^{i\omega_0 h_k(\boldsymbol{\rho}_k)/c}$—to be random at each transverse position with correlation widths on the order of the optical wavelength, the integrals in Eqs. (5.2) and (5.3) imply that the field envelopes at planes 1 and 2 (and analogously, 3) are sums of a large number of independent random contributions. Accordingly, by the central limit theorem, we can take these field envelopes to be Gaussian random processes conditioned on knowledge of the previous plane's

field envelope. In doing so, we can evaluate fourth moments of these envelopes by Gaussian moment factoring. In particular, we have

$$
\begin{aligned}
\langle I_2(\boldsymbol{\rho}_2;\boldsymbol{\mu})I_2(\tilde{\boldsymbol{\rho}}_2;\tilde{\boldsymbol{\mu}})\rangle_1 =\ & \langle E_2(\boldsymbol{\rho}_2;\boldsymbol{\mu})E_2^*(\boldsymbol{\rho}_2;\boldsymbol{\mu})E_2(\tilde{\boldsymbol{\rho}}_2;\tilde{\boldsymbol{\mu}})E_2^*(\tilde{\boldsymbol{\rho}}_2;\tilde{\boldsymbol{\mu}})\rangle_1 \qquad (5.9)\\
=\ & \langle E_2(\boldsymbol{\rho}_2;\boldsymbol{\mu})E_2^*(\boldsymbol{\rho}_2;\boldsymbol{\mu})\rangle_1\langle E_2(\tilde{\boldsymbol{\rho}}_2;\tilde{\boldsymbol{\mu}})E_2^*(\tilde{\boldsymbol{\rho}}_2;\tilde{\boldsymbol{\mu}})\rangle_1 \\
& + |\langle E_2(\boldsymbol{\rho}_2;\boldsymbol{\mu})E_2(\tilde{\boldsymbol{\rho}}_2;\tilde{\boldsymbol{\mu}})\rangle_1|^2 + |\langle E_2(\boldsymbol{\rho}_2;\boldsymbol{\mu})E_2^*(\tilde{\boldsymbol{\rho}}_2;\tilde{\boldsymbol{\mu}})\rangle_1|^2.
\end{aligned}
$$
$$(5.10)$$

Note, here we are taking a conditional mean where we've assumed a known field envelope at plane 0. The second term in this sum is 0 due to the diffuser statistics. Using Fresnel propagation the remaining terms expand to give

$$
\begin{aligned}
\langle I_2(\boldsymbol{\rho}_2;\boldsymbol{\mu})I_2(\tilde{\boldsymbol{\rho}}_2;\tilde{\boldsymbol{\mu}})\rangle_1 = \frac{1}{L^4}\Bigg[& \int \mathrm{d}^2\boldsymbol{\rho}_1 \int \mathrm{d}^2\tilde{\boldsymbol{\rho}}_1\, I_1(\boldsymbol{\rho}_1;\boldsymbol{\mu})I_1(\tilde{\boldsymbol{\rho}}_1;\tilde{\boldsymbol{\mu}})e^{-\frac{8}{d_1^2}(|\boldsymbol{\rho}_1|^2+|\tilde{\boldsymbol{\rho}}_1|^2)} \\
& + \int \mathrm{d}^2\boldsymbol{\rho}_1 \int \mathrm{d}^2\tilde{\boldsymbol{\rho}}_1\, E_1(\boldsymbol{\rho}_1;\boldsymbol{\mu})E_1^*(\boldsymbol{\rho}_1;\tilde{\boldsymbol{\mu}})E_1^*(\tilde{\boldsymbol{\rho}}_1;\boldsymbol{\mu})E_1(\tilde{\boldsymbol{\rho}}_1;\tilde{\boldsymbol{\mu}}) \\
& \times e^{-\frac{8}{d_1^2}(|\boldsymbol{\rho}_1|^2+|\tilde{\boldsymbol{\rho}}_1|^2)}e^{-i\frac{\omega_0}{cL}(\boldsymbol{\rho}_1-\tilde{\boldsymbol{\rho}}_1)\cdot(\boldsymbol{\rho}_2-\tilde{\boldsymbol{\rho}}_2)}\Bigg]. \qquad (5.11)
\end{aligned}
$$

Now, using the law of iterated expectation and taking advantage of the linearity of expectation, we can average over the statistics of the first diffuser yielding

$$
\begin{aligned}
\langle I_2(\boldsymbol{\rho}_2;\boldsymbol{\mu})I_2(\tilde{\boldsymbol{\rho}}_2;\tilde{\boldsymbol{\mu}})\rangle_{0,1} = \frac{1}{L^4}\Bigg[& \int \mathrm{d}^2\boldsymbol{\rho}_1 \int \mathrm{d}^2\tilde{\boldsymbol{\rho}}_1\, \langle I_1(\boldsymbol{\rho}_1;\boldsymbol{\mu})I_1(\tilde{\boldsymbol{\rho}}_1;\tilde{\boldsymbol{\mu}})\rangle_0 e^{-\frac{8}{d_1^2}(|\boldsymbol{\rho}_1|^2+|\tilde{\boldsymbol{\rho}}_1|^2)} \\
& + \int \mathrm{d}^2\boldsymbol{\rho}_1 \int \mathrm{d}^2\tilde{\boldsymbol{\rho}}_1\, \langle E_1(\boldsymbol{\rho}_1;\boldsymbol{\mu})E_1^*(\boldsymbol{\rho}_1;\tilde{\boldsymbol{\mu}})E_1^*(\tilde{\boldsymbol{\rho}}_1;\boldsymbol{\mu})E_1(\tilde{\boldsymbol{\rho}}_1;\tilde{\boldsymbol{\mu}})\rangle_0 \\
& \times e^{-\frac{8}{d_1^2}(|\boldsymbol{\rho}_1|^2+|\tilde{\boldsymbol{\rho}}_1|^2)}e^{-i\frac{\omega_0}{cL}(\boldsymbol{\rho}_1-\tilde{\boldsymbol{\rho}}_1)\cdot(\boldsymbol{\rho}_2-\tilde{\boldsymbol{\rho}}_2)}\Bigg]. \qquad (5.12)
\end{aligned}
$$

A similar analysis provides similar formulas for this moment at planes 1 and 3, which differ only in the subscripts and the presence of the pupil term. As is clear from this result, the moment at each plane depends on that for the one prior. This allows us to cascade these results from plane to plane, provided however that we also

have a result for one other fourth-order moment, namely

$$
\langle E_2(\boldsymbol{\rho}_2; \boldsymbol{\mu}) E_2^*(\boldsymbol{\rho}_2; \tilde{\boldsymbol{\mu}}) E_2^*(\tilde{\boldsymbol{\rho}}_2; \boldsymbol{\mu}) E_2(\tilde{\boldsymbol{\rho}}_2; \tilde{\boldsymbol{\mu}}) \rangle_{0,1}
$$

$$
= \frac{1}{L^4} \left[\int \mathrm{d}^2 \boldsymbol{\rho}_1 \int \mathrm{d}^2 \tilde{\boldsymbol{\rho}}_1 \, \langle E_1(\boldsymbol{\rho}_1; \boldsymbol{\mu}) E_1^*(\boldsymbol{\rho}_1; \tilde{\boldsymbol{\mu}}) E_1^*(\tilde{\boldsymbol{\rho}}_1; \boldsymbol{\mu}) E_1(\tilde{\boldsymbol{\rho}}_1; \tilde{\boldsymbol{\mu}}) \rangle_0 e^{-\frac{8}{d_1^2}(|\boldsymbol{\rho}_1|^2 + |\tilde{\boldsymbol{\rho}}_1|^2)} \right.
$$

$$
\left. + \int \mathrm{d}^2 \boldsymbol{\rho}_1 \int \mathrm{d}^2 \tilde{\boldsymbol{\rho}}_1 \, \langle I_1(\boldsymbol{\rho}_1; \boldsymbol{\mu}) I_1(\tilde{\boldsymbol{\rho}}_1; \tilde{\boldsymbol{\mu}}) \rangle_0 e^{-\frac{8}{d_1^2}(|\boldsymbol{\rho}_1|^2 + |\tilde{\boldsymbol{\rho}}_1|^2)} e^{-i\frac{\omega_0}{cL}(\boldsymbol{\rho}_1 - \tilde{\boldsymbol{\rho}}_1)\cdot(\boldsymbol{\rho}_2 - \tilde{\boldsymbol{\rho}}_2)} \right], \quad (5.13)
$$

which follows from a similar analysis and which can be further extended to similar results for planes 1 and 3.

Given our initial, Gaussian illumination envelope, each of these integrals can be evaluated in closed form. We find

$$
\langle I_1(\boldsymbol{\rho}_1; \boldsymbol{\mu}) I_1(\tilde{\boldsymbol{\rho}}_1; \tilde{\boldsymbol{\mu}}) \rangle_0 = \langle I_1 \rangle^2 \left[1 + e^{-\frac{4}{d_1^2}\Omega_{01}^2 |\boldsymbol{\rho}_1 - \tilde{\boldsymbol{\rho}}_1|^2} e^{-\frac{4}{d_0^2}|\boldsymbol{\mu} - \tilde{\boldsymbol{\mu}}|^2} \right], \quad (5.14)
$$

$$
\langle I_2(\boldsymbol{\rho}_2; \boldsymbol{\mu}) I_2(\tilde{\boldsymbol{\rho}}_2; \tilde{\boldsymbol{\mu}}) \rangle_{0,1} = \langle I_2 \rangle^2 \left[1 + e^{-\frac{4}{d_0^2}\Omega_{01}^2 |\boldsymbol{\rho}_2 - \tilde{\boldsymbol{\rho}}_2|^2} e^{-\frac{4}{d_0^2}|\boldsymbol{\mu} - \tilde{\boldsymbol{\mu}}|^2} + \frac{1}{1 + \Omega_{01}^2} e^{-\frac{4}{d_0^2}|\boldsymbol{\mu} - \tilde{\boldsymbol{\mu}}|^2} \right.
$$

$$
\left. + \frac{1}{1 + \Omega_{01}^2} e^{-\frac{4}{d_0^2}\frac{\Omega_{01}^2}{1 + \Omega_{01}^2}|\boldsymbol{\rho}_2 - \tilde{\boldsymbol{\rho}}_2 + \boldsymbol{\mu} - \tilde{\boldsymbol{\mu}}|^2} \right], \quad (5.15)
$$

and

$$
\langle I_3(\boldsymbol{\rho}_3; \boldsymbol{\mu}) I_3(\tilde{\boldsymbol{\rho}}_3; \tilde{\boldsymbol{\mu}}) \rangle_{0,1,2}
$$

$$
= \langle I_3 \rangle^2 \left[1 + e^{-\frac{4}{d_1^2}\Omega_{12}^2 |\boldsymbol{\rho}_3 - \tilde{\boldsymbol{\rho}}_3|^2} e^{-\frac{4}{d_0^2}|\boldsymbol{\mu} - \tilde{\boldsymbol{\mu}}|^2} + \frac{1}{1 + \Omega_{01}^2} e^{-\frac{4}{d_0^2}|\boldsymbol{\mu} - \tilde{\boldsymbol{\mu}}|^2} + \frac{1}{1 + \Omega_{12}^2} e^{-\frac{4}{d_0^2}|\boldsymbol{\mu} - \tilde{\boldsymbol{\mu}}|^2} \right.
$$

$$
+ \frac{1}{1 + \Omega_{01}^2} e^{-\frac{4}{d_1^2}\Omega_{12}^2 |\boldsymbol{\rho}_3 - \tilde{\boldsymbol{\rho}}_3|^2} e^{-\frac{4}{d_0^2}\frac{\Omega_{01}^2}{1 + \Omega_{01}^2}|\boldsymbol{\mu} - \tilde{\boldsymbol{\mu}}|^2} + \frac{1}{1 + \Omega_{12}^2} e^{-\frac{4}{d_1^2}\frac{\Omega_{12}^2}{1 + \Omega_{12}^2}|\boldsymbol{\rho}_3 - \tilde{\boldsymbol{\rho}}_3|^2}
$$

$$
+ \frac{1}{1 + \Omega_{01}^2 + \Omega_{12}^2} e^{-\frac{4}{d_0^2}\frac{\Omega_{01}^2}{1 + \Omega_{01}^2 + \Omega_{12}^2}|\boldsymbol{\mu} - \tilde{\boldsymbol{\mu}}|^2}
$$

$$
\left. + \frac{1}{1 + \Omega_{01}^2 + \Omega_{12}^2} e^{-\frac{4}{d_1^2}\Omega_{12}^2 \frac{1 + \Omega_{01}^2}{1 + \Omega_{01}^2 + \Omega_{12}^2}|\boldsymbol{\rho}_3 - \tilde{\boldsymbol{\rho}}_3|^2} e^{-\frac{4}{d_0^2}|\boldsymbol{\mu} - \tilde{\boldsymbol{\mu}}|^2} \right], \quad (5.16)
$$

where for notational convenience we have defined mixed Fresnel numbers $\Omega_{ij} \equiv$

88

$\omega_0 d_i d_j / 8cL$. Ordinary speckle has an irradiance variance that equals the square of the mean irradiance. Observing Eq. (5.16) then, subtracting the squared-mean irradiance from both sides and evaluating at $\boldsymbol{\rho}_3 = \tilde{\boldsymbol{\rho}}_3$ and $\boldsymbol{\mu} = \tilde{\boldsymbol{\mu}}$, reveals that the plane 3 speckle strength can be as bad as 7 times that of ordinary speckle. However, we propose two methods that can reduce this a great deal.

Stating our results as we have in terms of an offset in the initial illumination now allows us to ask whether we can reduce speckle by varying the center of the initial illumination and integrating over time. We imagine varying the initial illumination's center about a small circle with radius r and integrating over one full revolution which occurs in some time t_0 slow enough that this variation doesn't modify the unmodulated Fresnel diffraction formula we've been using but fast enough that we need not worry about the scene changing appreciably. Accordingly, the offset is given by

$$\boldsymbol{\mu} = \boldsymbol{\mu}(t) = r \begin{bmatrix} \cos(2\pi t/t_0) \\ \sin(2\pi t/t_0) \end{bmatrix}. \tag{5.17}$$

Focusing our attention on the plane 3 speckle, we see that the effect of the offset appears only in Gaussian factors present in some of the terms. In particular, to find the result of this temporal variation and averaging, we need only evaluate one integral:

$$\int_0^{t_0} \mathrm{d}t \int_0^{t_0} \mathrm{d}\tilde{t} e^{-\alpha |\boldsymbol{\mu}(t) - \boldsymbol{\mu}(\tilde{t})|^2} = t_0^2 e^{-2\alpha r^2} \mathrm{BI}_0(2\alpha r^2) \tag{5.18}$$

where α takes on values as dictated by the various terms of Eq. (5.16) and BI_0 denotes the zeroth-order modified Bessel function of the first kind. That this temporal washing out actually helps is demonstrated by

$$\lim_{r \to \infty} e^{-2\alpha r^2} \mathrm{BI}_0(2\alpha r^2) = 0, \tag{5.19}$$

i.e., as the radius of the variation gets large, the terms of the plane 3 speckle that contain the offset factors vanish completely after averaging. However, in practice we will want to keep r small so as to not lose spatial resolution. The question is

how quickly this tradeoff occurs. Looking at those terms for which $\alpha = 4/d_0^2$ (which amounts to all the relevant terms when $\Omega_{01} \gg 1$), by numerical evaluation we find that

$$e^{-2\alpha r^2}\text{BI}_0(2\alpha r^2) \approx 0.14d_0/r \qquad (5.20)$$

for r/d_0 in the range 1 to 100.

The tradeoff between resolution and speckle reduction afforded by our time variation method may not prove sufficient in practice. However, another method for reducing speckle is found in manipulating the mixed Fresnel numbers. Ignoring the initial term of Eq. (5.16), all but one of the remaining terms fall off as Ω_{01} and Ω_{12} get large, vanishing entirely in the infinite limit. Taking values close to what we might expect in practice—$\lambda_0 = 532\,\text{nm}$ optical wavelength, $L = 1\,\text{m}$ to $10\,\text{m}$ scene depth and standoff, $d_0 = 1\,\text{mm}$ to $1\,\text{cm}$ spot size, $d_1 = 3\,\text{cm}$ to $2\,\text{m}$ target size, and $d_2 = 1\,\text{m}$ to $10\,\text{m}$ wall size—we find that $\Omega_{01} \approx 4.43$ to 2.95×10^4 and $\Omega_{12} \approx 4.43\times 10^4$ to 2.95×10^7. Even the least favorable attenuation factor implied by this is $1/(1 + \Omega_{01}^2) \approx 0.05$. So in practice, we can expect this Fresnel-number attenuation effect to make most of the terms in Eq. (5.16) insignificant.

Before proceeding, it's worth considering the extent to which temporal-averaging and Fresnel-number attenuation effects reduce the speckle at each plane. Their behaviors are summarized in Table 5.1. The table assumes that each form of help is strong enough to make the terms they attenuate insignificant. For plane 3, we can see that either form of help is sufficient to reduce the speckle to ordinary strength. Moreover, we can eliminate speckle entirely by employing both methods simultaneously.

The preceding results indicate that the Fresnel-number attenuation effect seems very promising in practice, whereas the temporal-averaging attenuation is perhaps less so. In fact, we argue that speckle will not be a concern for this CW case. Considering the Fresnel-number attenuation effect alone, the remaining ordinary speckle is accounted for by the second term in Eq. (5.16). This term's value at $\boldsymbol{\rho}_3 = \tilde{\boldsymbol{\rho}}_3$ is the usual ordinary speckle strength, but its nominal spatial extent is only

Plane	No help	Ω help	t help	both
1	ordinary	ordinary	none	none
2	3×	ordinary	none	none
3	7×	ordinary	ordinary	none

Table 5.1: Speckle strength as measured by the peak irradiance variance relative to the squared-mean irradiance. The first column lists the unmitigated speckle strengths for each plane. The second column lists the strengths for the case in which $\Omega_{01}, \Omega_{12} \gg 1$ but no temporal averaging is employed. The third column lists the strengths for the case in which revolving illumination and temporal averaging is successfully employed but the Fresnel numbers are not large enough to significantly attenuate any terms. The last column lists the strengths for the case in which both the temporal-averaging technique is employed and $\Omega_{01}, \Omega_{12} \gg 1$.

$|\boldsymbol{\rho}_3 - \tilde{\boldsymbol{\rho}}_3| = 4L\lambda_0/2\pi d_2$, which in practice will be of the order of an optical wavelength. So, for any reasonable detector size, we can expect these speckles to be averaged out.

5.2   Modulated Speckle

In this section we turn our attention to modulated speckle, i.e., the case of relevance to $\mathcal{P}$-field imaging.

5.2.1   Speckle Strength

Unfortunately, although we found quantitative—even favorable—results for CW speckle, the modulated case proves more challenging to analyze. Accordingly, our analysis will be limited to the speckle at plane 1, i.e., the speckle shining on the hidden target in the NLoS analogy. We begin by introducing

$$\tilde{\mathcal{P}}_z(\boldsymbol{\rho}_z, \omega_-) \equiv \int \frac{d\omega_+}{2\pi} \, \mathcal{E}_z(\boldsymbol{\rho}_z, \omega_+ + \omega_-/2)\mathcal{E}_z^*(\boldsymbol{\rho}_z, \omega_+ - \omega_-/2), \qquad (5.21)$$

whose ensemble average over any relevant diffusers is the $\mathcal{P}$ field, i.e., $\langle \tilde{\mathcal{P}}_z(\boldsymbol{\rho}_z, \omega_-) \rangle = \mathcal{P}_z(\boldsymbol{\rho}_z, \omega_-)$.

In general, at the first plane we have

$$
\langle |\tilde{\mathcal{P}}_1(\boldsymbol{\rho}_1, \omega_-)|^2 \rangle_0
$$

$$
= \int \frac{d\omega_+}{2\pi} \int \frac{d\tilde{\omega}_+}{2\pi}
$$

$$
\langle \mathcal{E}_1(\boldsymbol{\rho}_1, \omega_+ + \omega_-/2)\mathcal{E}_1^*(\boldsymbol{\rho}_1, \omega_+ - \omega_-/2)\mathcal{E}_1^*(\boldsymbol{\rho}_1, \tilde{\omega}_+ + \omega_-/2)\mathcal{E}_1(\boldsymbol{\rho}_1, \tilde{\omega}_+ - \omega_-/2) \rangle_0
$$

$$
= \int \frac{d\omega_+}{2\pi} \int \frac{d\tilde{\omega}_+}{2\pi}
$$

$$
\Big[\langle \mathcal{E}_1(\boldsymbol{\rho}_1, \omega_+ + \omega_-/2)\mathcal{E}_1^*(\boldsymbol{\rho}_1, \omega_+ - \omega_-/2)\rangle_0 \langle \mathcal{E}_1^*(\boldsymbol{\rho}_1, \tilde{\omega}_+ + \omega_-/2)\mathcal{E}_1(\boldsymbol{\rho}_1, \tilde{\omega}_+ - \omega_-/2)\rangle_0
$$

$$
+ \langle \mathcal{E}_1(\boldsymbol{\rho}_1, \omega_+ + \omega_-/2)\mathcal{E}_1^*(\boldsymbol{\rho}_1, \tilde{\omega}_+ + \omega_-/2)\rangle_0 \langle \mathcal{E}_1^*(\boldsymbol{\rho}_1, \omega_+ - \omega_-/2)\mathcal{E}_1(\boldsymbol{\rho}_1, \tilde{\omega}_+ - \omega_-/2)\rangle_0
$$

$$
+ \langle \mathcal{E}_1(\boldsymbol{\rho}_1, \omega_+ + \omega_-/2)\mathcal{E}_1(\boldsymbol{\rho}_1, \tilde{\omega}_+ - \omega_-/2)\rangle_0 \langle \mathcal{E}_1^*(\boldsymbol{\rho}_1, \omega_+ - \omega_-/2)\mathcal{E}_1^*(\boldsymbol{\rho}_1, \tilde{\omega}_+ + \omega_-/2)\rangle_0 \Big],
$$

$$
(5.22)
$$

which follows from Gaussian moment factoring. Here however, the factoring takes place for each pair of integrated center frequencies but is still afforded by the fact that $\mathcal{E}_1$ falls within the scope of the central limit theorem. As in the CW case, the last of these terms vanishes owing to the diffuser statistics. The first term, after integration, is merely $|\mathcal{P}_1(\boldsymbol{\rho}_1, \omega_-)|^2$. Hence the remaining term, which can be expanded symbolically via the Fresnel propagation formula, is the $\mathcal{P}$-field's variance, viz.,

$$
\langle |\tilde{\mathcal{P}}_1(\boldsymbol{\rho}_1, \omega_-)|^2 \rangle_0 - |\mathcal{P}_1(\boldsymbol{\rho}_1, \omega_-)|^2
$$

$$
= \int \frac{d\omega_+}{2\pi} \int \frac{d\tilde{\omega}_+}{2\pi}
$$

$$
\langle \mathcal{E}_1(\boldsymbol{\rho}_1, \omega_+ + \omega_-/2)\mathcal{E}_1^*(\boldsymbol{\rho}_1, \tilde{\omega}_+ + \omega_-/2)\rangle_0 \langle \mathcal{E}_1^*(\boldsymbol{\rho}_1, \omega_+ - \omega_-/2)\mathcal{E}_1(\boldsymbol{\rho}_1, \tilde{\omega}_+ - \omega_-/2)\rangle_0
$$

$$
(5.23)
$$

$$
= \frac{1}{L^4} \int \frac{d\omega_+}{2\pi} \int \frac{d\tilde{\omega}_+}{2\pi} \int d\boldsymbol{\rho}_0 \int d\tilde{\boldsymbol{\rho}}_0
$$

$$
\mathcal{E}_0(\boldsymbol{\rho}_0, \omega_+ + \omega_-/2)\mathcal{E}_0^*(\boldsymbol{\rho}_0, \tilde{\omega}_+ + \omega_-/2)\mathcal{E}_0^*(\tilde{\boldsymbol{\rho}}_0, \omega_+ - \omega_-/2)\mathcal{E}_0(\tilde{\boldsymbol{\rho}}_0, \tilde{\omega}_+ - \omega_-/2)
$$

$$
\times e^{i\frac{\omega_+ - \tilde{\omega}_+}{2cL}\left(|\boldsymbol{\rho}_1 - \boldsymbol{\rho}_0|^2 - |\boldsymbol{\rho}_1 - \tilde{\boldsymbol{\rho}}_0|^2\right)}.
$$

$$
(5.24)
$$

Although symbolically articulable, this result seems impenetrable without further

specificity.

To simplify this result further, we assume that the initial illumination can be factored into a spatial component and a temporal one, viz.,

$$E_0(\boldsymbol{\rho}_0, t) = E_0(\boldsymbol{\rho}_0) S(t) \tag{5.25}$$

$$\mathcal{E}_0(\boldsymbol{\rho}_0, \omega) = E_0(\boldsymbol{\rho}_0) \mathcal{S}(\omega). \tag{5.26}$$

Notably, this assumption will not carry over to E_1 owing to the nature of Fresnel propagation, which will mix the space and time dependence. Applying it to our variance result yields

$$
\begin{aligned}
&\langle |\tilde{\mathcal{P}}_1(\boldsymbol{\rho}_1, \omega_-)|^2 \rangle_0 - |\mathcal{P}_1(\boldsymbol{\rho}_1, \omega_-)|^2 \\
&= \frac{1}{L^4} \int \frac{d\omega_+}{2\pi} \int \frac{d\tilde{\omega}_+}{2\pi} \int d\boldsymbol{\rho}_0 \int d\tilde{\boldsymbol{\rho}}_0 \, |E_0(\boldsymbol{\rho}_0)|^2 \, |E_0(\tilde{\boldsymbol{\rho}}_0)|^2 \, e^{i\frac{\omega_+ - \tilde{\omega}_+}{2cL}\left(|\boldsymbol{\rho}_1 - \boldsymbol{\rho}_0|^2 - |\boldsymbol{\rho}_1 - \tilde{\boldsymbol{\rho}}_0|^2\right)} \\
&\quad \times \mathcal{S}(\omega_+ + \omega_-/2)\mathcal{S}^*(\tilde{\omega}_+ + \omega_-/2)\mathcal{S}^*(\omega_+ - \omega_-/2)\mathcal{S}(\tilde{\omega}_+ - \omega_-/2),
\end{aligned} \tag{5.27}
$$

which, while simpler, still doesn't lend itself to further evaluation. However, this result does allow us to establish an upper bound on the variance of $\mathcal{P}_1(\boldsymbol{\rho}_1, 0)$:

$$
\begin{aligned}
&\langle |\tilde{\mathcal{P}}_1(\boldsymbol{\rho}_1, 0)|^2 \rangle_0 - |\mathcal{P}_1(\boldsymbol{\rho}_1, 0)|^2 \\
&\quad = \frac{1}{L^4} \int \frac{d\omega_+}{2\pi} \int \frac{d\tilde{\omega}_+}{2\pi} \int d\boldsymbol{\rho}_0 \int d\tilde{\boldsymbol{\rho}}_0 \, |E_0(\boldsymbol{\rho}_0)|^2 \, |E_0(\tilde{\boldsymbol{\rho}}_0)|^2 \, |\mathcal{S}(\omega_+)|^2 \, |\mathcal{S}(\tilde{\omega}_+)|^2 \\
&\qquad \times e^{i\frac{\omega_+ - \tilde{\omega}_+}{2cL}\left(|\boldsymbol{\rho}_1 - \boldsymbol{\rho}_0|^2 - |\boldsymbol{\rho}_1 - \tilde{\boldsymbol{\rho}}_0|^2\right)} \\
&\quad \leq \frac{1}{L^4} \int \frac{d\omega_+}{2\pi} \int \frac{d\tilde{\omega}_+}{2\pi} \int d\boldsymbol{\rho}_0 \int d\tilde{\boldsymbol{\rho}}_0 \, |E_0(\boldsymbol{\rho}_0)|^2 \, |E_0(\tilde{\boldsymbol{\rho}}_0)|^2 \, |\mathcal{S}(\omega_+)|^2 \, |\mathcal{S}(\tilde{\omega}_+)|^2 \\
&\quad = \left| \frac{1}{L^2} \int d\boldsymbol{\rho}_0 \, \mathcal{P}_0(\boldsymbol{\rho}_0, 0) \right|^2 \\
&\quad = |\mathcal{P}_1(\boldsymbol{\rho}_1, 0)|^2.
\end{aligned} \tag{5.28}
$$

The bound in (5.28) shows the speckle in the zero-frequency component of the $\mathcal{P}$ field at the target plane is no stronger than ordinary speckle and may even be appreciably weaker.

At first, this result may seem at odds with that of Teichman [27], who found that the $\mathcal{P}$-field speckle strength will at *best* be that of ordinary speckle and in general be stronger. His result considers the special case of single-frequency sinusoidal modulation, and—though not rederived here—we find it can be reproduced line-by-line in our paraxial framework using Gaussian moment factoring of the field envelope in place of his regional analysis of the four-point diffuser correlation function. As it turns out, the apparent discrepancy is owed to the fact that the $\mathcal{P}$-field speckle analyzed by Teichman is the speckle of the component at the modulation frequency, whereas the bound above applies only to the zero-frequency component.

To illustrate these results side-by-side concretely, we consider the following modulation:

$$S(t) = e^{-t^2/T^2} \cos(\Omega t) \tag{5.29}$$

$$\mathcal{S}(\omega) = \sqrt{\pi} \frac{T}{2} \left(e^{-\frac{T^2}{4}(\omega - \Omega)^2} + e^{-\frac{T^2}{4}(\omega + \Omega)^2} \right). \tag{5.30}$$

The Gaussian temporal attenuation is employed to avoid dealing with impulse functions. We assume $\Omega T \gg 1$, i.e., that the signal lasts many modulation periods, which effectively corresponds to Teichman's single-frequency-modulation case. Note, whereas the field envelope modulation frequency is Ω, the modulation frequency of the irradiance is 2Ω, and so that is the relevant frequency at which we will be concerned with the $\mathcal{P}$ field.

Using our narrowband modulation assumption, we can approximate the relevant product of $\mathcal{S}$ functions in Eq. (5.27)—evaluated at $\omega_- = 2\Omega$—accordingly:

$$\mathcal{S}(\omega_+ + \Omega)\mathcal{S}^*(\tilde{\omega}_+ + \Omega)\mathcal{S}^*(\omega_+ - \Omega)\mathcal{S}(\tilde{\omega}_+ - \Omega) \approx \frac{\pi^2 T^4}{16} e^{-\frac{T^2}{2}(\omega_+^2 + \tilde{\omega}_+^2)}. \tag{5.31}$$

This product effectively acts as a low pass filter on the integration frequencies in Eq. (5.27). As a result, we have $|\omega_+ - \tilde{\omega}_+|/2cL \ll \Omega/2cL = \pi/\Lambda L$ (where $\Lambda = 2\pi c/\Omega$ is the modulation wavelength), and so if we have sufficiently narrow initial illumination such that $E_0(\boldsymbol{\rho}_0) \approx 0$ for $|\boldsymbol{\rho}_0| > \sqrt{\Lambda L}$ ($\approx 22\,\mathrm{cm}$ for $\Lambda = 5\,\mathrm{cm}$ and

$L = 1\,\text{m}$), the Fresnel propagation term can be approximated by a Fourier transform kernel, yielding

$$\langle |\tilde{\mathcal{P}}_1(\boldsymbol{\rho}_1, 2\Omega)|^2 \rangle_0 - |\mathcal{P}_1(\boldsymbol{\rho}_1, 2\Omega)|^2$$
$$= \frac{1}{L^4} \int \frac{\mathrm{d}\omega_+}{2\pi} \int \frac{\mathrm{d}\tilde{\omega}_+}{2\pi} \int \mathrm{d}\boldsymbol{\rho}_0 \int \mathrm{d}\tilde{\boldsymbol{\rho}}_0 \, I_0(\boldsymbol{\rho}_0) I_0(\tilde{\boldsymbol{\rho}}_0) \frac{\pi^2 T^4}{16} e^{-\frac{T^2}{2}(\omega_+^2 + \tilde{\omega}_+^2)} e^{-i\frac{\omega_+ - \tilde{\omega}_+}{cL} \boldsymbol{\rho}_1 \cdot (\boldsymbol{\rho}_0 - \tilde{\boldsymbol{\rho}}_0)},$$
$$(5.32)$$

where we've defined $I_0(\boldsymbol{\rho}) = |E_0(\boldsymbol{\rho})|^2$ in analogy with the CW case. Equation (5.32) affords us a much more tractable result for a reasonably practical scenario. This expression can be evaluated in closed form if we use the Gaussian illumination profile from the CW case,

$$I_0(\boldsymbol{\rho}_0) = \left(8P/\pi d_0^2\right) \exp\left(-8\left|\boldsymbol{\rho}_0\right|^2 / d_0^2\right), \qquad (5.33)$$

with $d_0^2 < \Lambda L$ to satisfy our assumption. We then get

$$\langle |\tilde{\mathcal{P}}_1(\boldsymbol{\rho}_1, 2\Omega)|^2 \rangle_0 - |\mathcal{P}_1(\boldsymbol{\rho}_1, 2\Omega)|^2 = \frac{\pi P^2 T^2}{32 L^4} \sqrt{\frac{1}{1 + \left(\frac{d_0}{2cLT}\right)^2 |\boldsymbol{\rho}_1|^2}}. \qquad (5.34)$$

This result is maximized on axis, where the square-root term vanishes. Say $|\boldsymbol{\rho}_1| < 2L$, as is certainly necessary for paraxial operation. From $d_0^2 < \Lambda L$ it then follows that

$$\left(\frac{d_0}{2cLT}\right)^2 |\boldsymbol{\rho}_1|^2 < \left(\frac{2\pi}{\Omega T}\sqrt{\frac{L}{\Lambda}}\right)^2 \ll 1 \qquad (5.35)$$

provided $\Omega T \gg 2\pi\sqrt{L/\Lambda}$, which amounts to ≈ 28.1 for $L = 1\,\text{m}$ and $\Lambda = 5\,\text{cm}$. In this reasonable regime, the square-root term in Eq. (5.34) can be neglected entirely so that

$$\langle |\tilde{\mathcal{P}}_1(\boldsymbol{\rho}_1, 2\Omega)|^2 \rangle_0 - |\mathcal{P}_1(\boldsymbol{\rho}_1, 2\Omega)|^2 = \frac{\pi P^2 T^2}{32 L^4}. \qquad (5.36)$$

Using the same assumptions we've employed so far, but being stricter so that

95

$d_0^2 \ll \Lambda L$, we can approximate and evaluate the squared-mean $\mathcal{P}$ field using a similar process resulting in

$$|\mathcal{P}_1(\boldsymbol{\rho}_1, 2\Omega)|^2 = \frac{1}{L^4} \int \frac{\mathrm{d}\omega_+}{2\pi} \int \frac{\mathrm{d}\tilde{\omega}_+}{2\pi} \int \mathrm{d}\boldsymbol{\rho}_0 \int \mathrm{d}\tilde{\boldsymbol{\rho}}_0$$

$$I_0(\boldsymbol{\rho}_0)I_0(\tilde{\boldsymbol{\rho}}_0)\frac{\pi^2 T^4}{16} e^{-\frac{T^2}{2}(\omega_+^2 + \tilde{\omega}_+^2)} e^{-i\frac{2\Omega}{cL}\boldsymbol{\rho}_1 \cdot (\boldsymbol{\rho}_0 - \tilde{\boldsymbol{\rho}}_0)} \tag{5.37}$$

$$= \frac{\pi P^2 T^2}{32L^4} e^{-\left(\frac{d_0 \Omega}{2cL}\right)^2 |\boldsymbol{\rho}_1|^2}. \tag{5.38}$$

This implies that the speckle at the modulation frequency is as strong as ordinary speckle on axis and is stronger off axis, in complete agreement with Teichman. However, we can see that in the worst case it is enhanced only by a factor

$$\exp\left((d_0\Omega|\boldsymbol{\rho}_1|/2cL)^2\right) < \exp\left((2\pi d_0/\Lambda)^2\right) \approx 1.08, \tag{5.39}$$

which follows from taking $|\boldsymbol{\rho}_1| < 2L$, $\Lambda = 5\,\mathrm{cm}$, and $d_0 = 2.2\,\mathrm{mm}$. So while Teichman's result is qualitatively accurate, in practice it seems the speckle at the modulation frequency has approximately ordinary strength, at least within the paraxial regime. Of course, it should be emphasized however that this result is limited to the speckle shining on the target plane, and our present analysis doesn't suffice to go further.

To illustrate our zero-frequency bound, we proceed by analyzing the zero-frequency-component speckle for our specific modulation. Now the relevant product of $\mathcal{S}$ functions is approximated by

$$|\mathcal{S}(\omega_+)|^2 |\mathcal{S}(\tilde{\omega}_+)|^2 \approx \frac{\pi^2 T^4}{16} \left(e^{-\frac{T^2}{2}(\omega_+ - \Omega)^2} + e^{-\frac{T^2}{2}(\omega_+ + \Omega)^2}\right) \left(e^{-\frac{T^2}{2}(\tilde{\omega}_+ - \Omega)^2} + e^{-\frac{T^2}{2}(\tilde{\omega}_+ + \Omega)^2}\right).$$
$$\tag{5.40}$$

The same analysis as the modulation frequency component case can be used to eval-

uate the zero-frequency variance. We find that

$$\langle|\tilde{\mathcal{P}}_1(\boldsymbol{\rho}_1,0)|^2\rangle - |\mathcal{P}_1(\boldsymbol{\rho}_1,0)|^2 = \frac{\pi P^2 T^2}{16L^4\sqrt{1+\alpha^2|\boldsymbol{\rho}_1|^2}}\left(1 + e^{-\frac{\Omega^2 T^2\alpha^2|\boldsymbol{\rho}_1|^2}{1+\alpha^2|\boldsymbol{\rho}_1|^2}} + 2e^{-\Omega^2 T^2}\right.$$
$$\left. + 4e^{-\frac{\Omega^2 T^2}{4}\left(\frac{2+3\alpha^2|\boldsymbol{\rho}_1|^2}{1+\alpha^2|\boldsymbol{\rho}_1|^2}\right)}\right), \tag{5.41}$$

where $\alpha \equiv d_0/2cLT$. Equation (5.41) has its unique maximum on axis, where it takes the value

$$\langle|\tilde{\mathcal{P}}_1(\mathbf{0},0)|^2\rangle_0 - |\mathcal{P}_1(\mathbf{0},0)|^2 = \frac{\pi P^2 T^2}{8L^4}\left(1 + e^{-\Omega^2 T^2} + 2e^{-\Omega^2 T^2/2}\right). \tag{5.42}$$

Moreover, we find that

$$|\mathcal{P}_1(\boldsymbol{\rho}_1,0)|^2 = \frac{\pi P^2 T^2}{8L^4}\left(1 + e^{-\Omega^2 T^2} + 2e^{-\Omega^2 T^2/2}\right), \tag{5.43}$$

which together with the variance result implies that the zero-frequency speckle has ordinary strength on axis and is attenuated off axis, in complete agreement with our bound from (5.28).

5.2.2 Speckle Size

As we saw in the CW case, although the speckle variance is important to consider, the speckle size can perhaps be even more impactful as the speckles may be sufficiently small so as to be naturally averaged out by a finite-area detector. Carrying out a similar analysis for the modulated case though proves more difficult, as expected. The quantity of concern, the spatial covariance, can be derived via a process similar to what was done above for the variance, relying on Gaussian moment factoring and the Fresnel propagation integral:

$$\langle \tilde{\mathcal{P}}_1(\boldsymbol{\rho}_1, \omega_-) \tilde{\mathcal{P}}_1^*(\tilde{\boldsymbol{\rho}}_1, \omega_-) \rangle_0 - \mathcal{P}_1(\boldsymbol{\rho}_1, \omega_-) \mathcal{P}_1^*(\tilde{\boldsymbol{\rho}}_1, \omega_-)$$

$$= \frac{1}{L^4} \int \frac{d\omega_+}{2\pi} \int \frac{d\tilde{\omega}_+}{2\pi} \int d^2\boldsymbol{\rho}_0 \int d^2\tilde{\boldsymbol{\rho}}_0$$

$$\mathcal{E}_0(\boldsymbol{\rho}_0, \omega_+ + \omega_-/2) \mathcal{E}_0^*(\boldsymbol{\rho}_0, \tilde{\omega}_+ + \omega_-/2) \mathcal{E}_0^*(\tilde{\boldsymbol{\rho}}_0, \omega_+ - \omega_-/2) \mathcal{E}_0(\tilde{\boldsymbol{\rho}}_0, \tilde{\omega}_+ - \omega_-/2)$$

$$\times e^{i\frac{\omega_0 + \omega_+ + \omega_-/2}{2cL}|\boldsymbol{\rho}_1 - \boldsymbol{\rho}_0|^2} e^{-i\frac{\omega_0 + \tilde{\omega}_+ + \omega_-/2}{2cL}|\tilde{\boldsymbol{\rho}}_1 - \boldsymbol{\rho}_0|^2} e^{-i\frac{\omega_0 + \omega_+ - \omega_-/2}{2cL}|\boldsymbol{\rho}_1 - \tilde{\boldsymbol{\rho}}_0|^2} e^{i\frac{\omega_0 + \tilde{\omega}_+ - \omega_-/2}{2cL}|\tilde{\boldsymbol{\rho}}_1 - \tilde{\boldsymbol{\rho}}_0|^2}.$$

$$(5.44)$$

The differing spatial coordinates in each of the four exponential terms makes it impossible to group them in any useful way, regardless of their frequency terms. Expanding the squares (not shown here) does not make the situation particularly more illuminating. Removing the exponentials altogether to obtain an upper bound, as we did earlier for the zero-frequency variance, is not an option as that removes all the spatial dependence, which is precisely the property we wish to analyze. Assuming a space-time factorable illumination also doesn't seem to help, as it wouldn't alleviate the issue with evaluating the exponential terms. However, by a combination of assumptions mimicking our earlier approach, we can proceed to get some insight. First, we assume factorable illumination with a narrowband cosine modulation and a narrow enough spatial profile that the Fresnel kernel can be approximated by a Fourier transform kernel. Then, we evaluate at $\omega_- = 2\Omega$, which enables us to use the simple form of the $\mathcal{S}$-function product we found earlier. Subsequent results will be limited to the modulated component, but ultimately that is the component that will be of interest for imaging. We find

$$\langle \tilde{\mathcal{P}}_1(\boldsymbol{\rho}_1, 2\Omega) \tilde{\mathcal{P}}_1^*(\tilde{\boldsymbol{\rho}}_1, 2\Omega) \rangle_0 - \mathcal{P}_1(\boldsymbol{\rho}_1, 2\Omega) \mathcal{P}_1^*(\tilde{\boldsymbol{\rho}}_1, 2\Omega)$$

$$= \frac{e^{i\frac{\Omega}{cL}\left(|\boldsymbol{\rho}_1|^2 - |\tilde{\boldsymbol{\rho}}_1|^2\right)}}{L^4} \int \frac{d\omega_+}{2\pi} \int \frac{d\tilde{\omega}_+}{2\pi} \int d^2\boldsymbol{\rho}_0 \int d^2\tilde{\boldsymbol{\rho}}_0 \, I_0(\boldsymbol{\rho}_0) I_0(\tilde{\boldsymbol{\rho}}_0) \frac{\pi^2 T^4}{16} e^{-\frac{T^2}{2}\left(\omega_+^2 + \tilde{\omega}_+^2\right)}$$

$$\times e^{i\frac{1}{cL}[-\boldsymbol{\rho}_0 \cdot \boldsymbol{\rho}_1(\omega_0 + \omega_+ + \Omega) + \boldsymbol{\rho}_0 \cdot \tilde{\boldsymbol{\rho}}_1(\omega_0 + \tilde{\omega}_+ + \Omega) + \tilde{\boldsymbol{\rho}}_0 \cdot \boldsymbol{\rho}_1(\omega_0 + \omega_+ - \Omega) - \tilde{\boldsymbol{\rho}}_0 \cdot \tilde{\boldsymbol{\rho}}_1(\omega_0 + \tilde{\omega}_+ - \Omega)]}.$$

$$(5.45)$$

By assuming the same Gaussian form for I_0 as we used earlier, i.e., Eq. (5.33), this integral is composed entirely of Gaussian terms and so can be evaluated in closed form. Unfortunately though, the guarantee of a closed-form result is not the guarantee of a simple result, and we find the result to be too cumbersome to display here. However, we can proceed with further analysis by assuming fixed values for the physical parameters and numerically evaluating the width of the magnitude of this covariance. In particular, we take $\lambda_0 = 532\,\text{nm}$, $\Lambda = 5\,\text{cm}$, $L = 1\,\text{m}$, $d_0 = 3\,\text{mm}$, and $T = 1\,\text{s}$.

Analysis is further complicated by the fact that the covariance depends on both $\boldsymbol{\rho}_1$ and $\tilde{\boldsymbol{\rho}}_1$ individually, and does not afford a simple expression in terms of only $\boldsymbol{\rho}_1 - \tilde{\boldsymbol{\rho}}_1$, i.e., $\tilde{\mathcal{P}}_1(\boldsymbol{\rho}_1, 2\Omega) - \mathcal{P}_1(\boldsymbol{\rho}_1, \Omega)$ is not statistically homogeneous. So, we proceed by fixing a value for $\tilde{\boldsymbol{\rho}}_1$, then treating the magnitude of the covariance as a weighting function in terms of $\boldsymbol{\rho}_1$. We numerically normalize this function so it can be treated like a pdf and then find its standard deviation to define the speckle size. That is, defining

$$f_{\boldsymbol{\rho}_1}(\boldsymbol{\rho}_1; \tilde{\boldsymbol{\rho}}_1) \equiv \frac{\left| \langle \tilde{\mathcal{P}}_1(\boldsymbol{\rho}_1, 2\Omega) \tilde{\mathcal{P}}_1^*(\tilde{\boldsymbol{\rho}}_1, 2\Omega) \rangle_0 - \mathcal{P}_1(\boldsymbol{\rho}_1, 2\Omega) \mathcal{P}_1^*(\tilde{\boldsymbol{\rho}}_1, 2\Omega) \right|}{\int \mathrm{d}^2\boldsymbol{\rho}_1 \left| \langle \tilde{\mathcal{P}}_1(\boldsymbol{\rho}_1, 2\Omega) \tilde{\mathcal{P}}_1^*(\tilde{\boldsymbol{\rho}}_1, 2\Omega) \rangle_0 - \mathcal{P}_1(\boldsymbol{\rho}_1, 2\Omega) \mathcal{P}_1^*(\tilde{\boldsymbol{\rho}}_1, 2\Omega) \right|}, \quad (5.46)$$

we take the speckle size at $\tilde{\boldsymbol{\rho}}_1$ to be

$$\sigma_{\mathrm{sp}}(\tilde{\boldsymbol{\rho}}_1) \equiv \sqrt{\int \mathrm{d}^2\boldsymbol{\rho}_1 \, |\boldsymbol{\rho}_1|^2 f_{\boldsymbol{\rho}_1}(\boldsymbol{\rho}_1; \tilde{\boldsymbol{\rho}}_1) - \left| \int \mathrm{d}^2\boldsymbol{\rho}_1 \, \boldsymbol{\rho}_1 f_{\boldsymbol{\rho}_1}(\boldsymbol{\rho}_1; \tilde{\boldsymbol{\rho}}_1) \right|^2}. \quad (5.47)$$

Conveniently, we find that the result is consistent to about 5 significant figures across a large variety of values for $\tilde{\boldsymbol{\rho}}_1$, varying from the origin all the way to $10\,\text{m}$ off-axis in both directions.[2] So, for all practical purposes, we find the speckle size for these physical parameters to be approximately $\sigma_{\mathrm{sp}} \approx 1.13 \times 10^{-4}\,\text{m}$. Coincidentally, this works out to be the same number, to similar precision, as $d_1/2\Omega_{01} = 4cL/d_0\omega_0$, the e^{-1}-attenuation radius of the first-bounce CW speckle from Eq. (5.14). To make

---

[2]This suggests that the covariance could be well approximated by a Schell model, viz.,

$$\mathrm{cov}(\tilde{\mathcal{P}}_1(\boldsymbol{\rho}_1, 2\Omega), \tilde{\mathcal{P}}_1(\tilde{\boldsymbol{\rho}}_1, 2\Omega)) \approx \mathrm{var}(\tilde{\mathcal{P}}_1((\boldsymbol{\rho}_1 + \tilde{\boldsymbol{\rho}}_1)/2, 2\Omega)) R(\boldsymbol{\rho}_1 - \tilde{\boldsymbol{\rho}}_1), \quad (5.48)$$

for some function $R(\cdot)$ such that $R(\mathbf{0}) = 1$.

a fair comparison though, we should use the standard deviation of the CW case as well, which differs by a factor of $\sqrt{2}$. So, it seems that the modulated first-bounce speckle size is only a factor of $\sqrt{2}$ greater than the CW speckle. Should this similarity hold for further bounces, the situation is quite favorable. Considering Eqs. (5.15) and (5.16), only the leading nontrivial term matters in each, as we've argued before that realistic parameter values will lead to mixed Fresnel numbers that significantly attenuate all the other terms. What's left then in each case is effectively a single-bounce speckle covariance that depends only on the previous pupil size. As the pupils only get larger (illumination size < target size < wall size), the speckle size only gets smaller. In particular we find speckle widths on the order of 10^{-6} m and 10^{-7} m for the second and third bounce respectively of the CW case, although sub-optical-wavelength correlation lengths would fall prey to the evanescence cutoff. Should such widths carry over to the modulated case, it is beyond question that any reasonable detector area will necessarily average over many speckles.

5.3 Shot-Noise Limit

The impact of a finite detector area integrating over multiple speckles can be perhaps most readily seen in analyzing the resulting statistics for semiclassical photodetection. The traditional semiclassical approach for analyzing photodetection statistics models the detected power (spatially-integrated irradiance) as generating a stochastic current in the form of a conditionally Poisson impulse train of elementary charge carriers conditioned on that detected power. This current is then divided by the elementary charge and integrated over time to yield a photon count N, which takes the form of a Poisson random variable conditioned on knowledge of the detected power. Since Poisson random variables are notable for their variance equaling their mean, the resulting signal-to-noise ratio (SNR) is $\langle N \rangle^2 / \langle \Delta N^2 \rangle = \langle N \rangle$, which increases monotonically as the detected power increases. This summarizes the shot-noise limit, in which the SNR is limited only by this fundamental photodetection noise whose ultimate origin is the quantum nature of the underlying charge carriers. When the input irradiance is

itself a random process, the unconditioned statistics of N may take a form other than Poisson. The resulting variance cannot be lower than the mean, i.e., the shot-noise limit, but on the other hand may contain additional excess-noise terms that threaten to degrade the SNR beyond what is already imposed by quantum theory. Speckle is an example of such excess noise, and using the results we've established so far we can analyze its impact on photodetection statistics.

For simplicity, we proceed in the CW case, where our results for multi-bounce speckle are best established. We imagine that the final irradiance is detected over a finite area A to produce a power

$$P(t) = P = \int_A \mathrm{d}^2\boldsymbol{\rho}\, I(\boldsymbol{\rho}), \tag{5.49}$$

where the lack of temporal dependence follows from the CW assumption. Here we use P to denote the detected power, not to be confused with our earlier use of P for the initial illumination power. Without loss of generality, we choose to work here in units in which I is measured in photons/m^2 so that P is measured in photons. The resulting photon count N is conditionally Poisson, such that its mean and variance conditioned on knowledge of P are given by

$$\langle \Delta N^2 \rangle_{|P} = \langle N \rangle_{|P} = \eta P T \tag{5.50}$$

where η is the detector's quantum efficiency and T the detector integration time. Accordingly, the unconditioned mean is given by

$$\langle N \rangle = \eta \langle P \rangle T. \tag{5.51}$$

The unconditioned variance of N can be found in terms of the statistics of P via

the law of iterated expectation or, equivalently, the law of total variance:

$$\langle \Delta N^2 \rangle = \langle N^2 \rangle - \langle N \rangle^2 \tag{5.52}$$

$$= \langle \langle N^2 \rangle_{|P} \rangle - (\eta \langle P \rangle T)^2 \tag{5.53}$$

$$= \langle \langle \Delta N^2 \rangle_{|P} + \langle N \rangle_{|P}^2 \rangle - \eta^2 \langle P \rangle^2 T^2 \tag{5.54}$$

$$= \langle \eta PT + \eta^2 P^2 T^2 \rangle - \eta^2 \langle P \rangle^2 T^2 \tag{5.55}$$

$$= \eta \langle P \rangle T + \eta^2 \langle \Delta P^2 \rangle T^2, \tag{5.56}$$

where the first term is the shot noise and the second term is the excess noise imposed by speckle. In the absence of speckle, the irradiance and accordingly the detected power are deterministic, and so the excess noise term is 0. However, in the presence of speckle, the relevant statistics of P can be found from

$$\langle P \rangle = \int_A \mathrm{d}^2 \boldsymbol{\rho} \, \langle I(\boldsymbol{\rho}) \rangle \tag{5.57}$$

$$\langle P^2 \rangle = \int_A \mathrm{d}^2 \boldsymbol{\rho} \int_A \mathrm{d}^2 \tilde{\boldsymbol{\rho}} \, \langle I(\boldsymbol{\rho}) I(\tilde{\boldsymbol{\rho}}) \rangle, \tag{5.58}$$

where $\langle I(\boldsymbol{\rho}) I(\tilde{\boldsymbol{\rho}}) \rangle$ is the correlation function we found for each bounce in Eqs. (5.14)–(5.16) evaluated at zero offset, i.e., $\boldsymbol{\mu} = \tilde{\boldsymbol{\mu}} = \mathbf{0}$. For our purposes, we will assume the detected light is that from the third bounce. Recalling that our irradiance correlation functions depend only on the magnitude of the difference of their spatial coordinates, i.e., that we found the irradiances to be statistically homogeneous and isotropic random processes, we define

$$\mathrm{cov}_{I_3}(|\boldsymbol{\rho}_-|) \equiv \langle I_3(\boldsymbol{\rho}_+ + \boldsymbol{\rho}_-/2; \mathbf{0}) I_3(\boldsymbol{\rho}_+ - \boldsymbol{\rho}_-/2; \mathbf{0}) \rangle_{0,1,2} - \langle I_3 \rangle^2. \tag{5.59}$$

Switching to sum and difference coordinates $\boldsymbol{\rho}_- = \boldsymbol{\rho}_3 - \tilde{\boldsymbol{\rho}}_3$ and $\boldsymbol{\rho}_+ = (\boldsymbol{\rho}_3 + \tilde{\boldsymbol{\rho}}_3)/2$, taking a circular detector area of radius R, and performing the $\boldsymbol{\rho}_+$ integration, we

have that

$$\langle \Delta P^2 \rangle = \int d^2 \boldsymbol{\rho}_- \, \text{cov}_{I_3}(|\boldsymbol{\rho}_-|) O(|\boldsymbol{\rho}_-|, 2R) \tag{5.60}$$

$$= K \langle P \rangle^2, \tag{5.61}$$

where

$$O(\zeta, D) = \begin{cases} \frac{D^2}{2} \left[\cos^{-1}\left(\frac{\zeta}{D}\right) - \frac{\zeta}{D}\sqrt{1 - \frac{\zeta^2}{D^2}} \right] & \text{if } 0 \le \zeta \le D \\ 0 & \text{else} \end{cases} \tag{5.62}$$

is the overlap area between two circles of diameter D whose origins are separated by a distance ζ, and

$$K \equiv \frac{1}{\pi^2 R^4} \int d^2 \boldsymbol{\rho}_- \, \frac{\text{cov}_{I_3}(|\boldsymbol{\rho}_-|)}{\langle I_3 \rangle^2} O(|\boldsymbol{\rho}_-|, 2R) \tag{5.63}$$

$$= \frac{1}{4R^2} \left[\frac{4R^2}{1 + \Omega_{01}^2} + \frac{4R^2}{1 + \Omega_{12}^2} + \frac{4R^2}{1 + \Omega_{01}^2 + \Omega_{12}^2} + \frac{d_1^2}{\Omega_{12}^2}(1 + \Omega_{12})\left(1 + \frac{1}{1 + \Omega_{01}^2}\right) \right.$$

$$- \frac{d_1^2(2 + \Omega_{01}^2)}{\Omega_{12}(1 + \Omega_{01}^2)} B\left(\frac{8R^2 \Omega_{12}}{d_1^2}\right) - \frac{d_1^2}{\Omega_{12}^2} B\left(\frac{8R^2 \Omega_{12}^2}{d_1^2(1 + \Omega_{12}^2)}\right)$$

$$\left. - \frac{d_1^2}{\Omega_{12}^2(1 + \Omega_{01}^2)} B\left(\frac{8R^2 \Omega_{12}^2(1 + \Omega_{01}^2)}{d_1^2(1 + \Omega_{01}^2 + \Omega_{12}^2)}\right) \right], \tag{5.64}$$

where

$$B(x) \equiv \exp(-x) \times (\text{BI}_0(x) + \text{BI}_1(x)), \tag{5.65}$$

with BI_n being the nth-order modified Bessel function of the first kind. In terms of this result, the photon-count variance is

$$\langle \Delta N^2 \rangle = \langle N \rangle + K \langle N \rangle^2. \tag{5.66}$$

So, provided $\langle N \rangle \ll 1/K$, the second term will be negligible compared to the first, and accordingly it can be said that we're operating in the shot-noise limit and that

the effects of speckle can be ignored. In terms of the SNR's behavior as $\langle N \rangle$ grows without bound, the shot-noise limit allows for the SNR to likewise grow without bound, whereas the effect of speckle can be seen as bounding this growth at SNR $\leq 1/K$ because we have that

$$\lim_{\langle N \rangle \to \infty} \frac{\langle N \rangle^2}{\langle \Delta N^2 \rangle} = \lim_{\langle N \rangle \to \infty} \frac{\langle N \rangle^2}{\langle N \rangle + K \langle N \rangle^2} = \frac{1}{K}. \tag{5.67}$$

Note, K monotonically decreases with increasing R, and we have that

$$\lim_{R \to 0} K = \frac{3 + \Omega_{01}^2}{1 + \Omega_{01}^2} + \frac{2}{1 + \Omega_{12}^2} + \frac{2}{1 + \Omega_{01}^2 + \Omega_{12}^2}, \tag{5.68}$$

and

$$\lim_{R \to \infty} K = \frac{3 + \Omega_{01}^4 + 4\Omega_{01}^2 + 3\Omega_{01}^2\Omega_{12}^2 + 4\Omega_{12}^2 + \Omega_{12}^4}{(1 + \Omega_{01}^2)(1 + \Omega_{12}^2)(1 + \Omega_{01}^2 + \Omega_{12}^2)}. \tag{5.69}$$

Moreover, for $\Omega_{01}, \Omega_{12} \ll 1$ we have that $\lim_{R \to 0} K \approx 7$ and $\lim_{R \to \infty} K \approx 3$, and for $\Omega_{01}, \Omega_{12} \gg 1$ we have that $\lim_{R \to 0} K \approx 1$ and $\lim_{R \to \infty} K \approx 0$. So, integrating over a large enough detector area negates one bounce's worth of speckle, and taking the two Fresnel numbers to be large enough negates the remaining two bounce's worth of speckle. Taking reasonable parameter values $\lambda_0 = 532\,\text{nm}$, $L = 1\,\text{m}$, $d_0 = 1\,\text{mm}$, $d_1 = 10\,\text{cm}$, $d_2 = 1\,\text{m}$, and $R = 1\,\text{cm}$, we find that $1/K \approx 4700$. So, speckle at worst limits the SNR to a very high value as $\langle N \rangle$ grows without bound.

5.4   Small-Reflector Limit

Despite the fact that our results for the modulated case have been thus far limited to first-order speckle, we find that further results can be obtained in the limit in which there is no spatial dependence. Physically, in the NLoS analogy, this corresponds to the case in which the initial illumination covers a very small area, the target is very small, and the third-bounce area is very small. The last constraint might be fulfilled, for example, if a small, diffuse object is used to see into an occluded space, as opposed

to a large wall. In the CW case, this amounts to the limit in which the mixed Fresnel numbers approach zero, which as we saw earlier leads to ordinary speckle strength after the first bounce, $3\times$ ordinary speckle strength after the second bounce, and $7\times$ ordinary speckle strength after the third bounce. In fact, for this case, the complete distributions of the speckle and speckled speckle irradiances are known [26]. Ignoring the attenuation factors from free-space propagation and the finite pupil sizes we have

$$p_{I_1}(I_1) = \begin{cases} \exp\left(-I_1/\langle I_1\rangle\right)/\langle I_1\rangle & \text{for } I_1 \geq 0 \\ 0 & \text{else} \end{cases} \tag{5.70}$$

$$p_{I_2}(I_2) = \begin{cases} 2K_0\left(2\sqrt{I_2/\langle I_1\rangle}\right)/\langle I_1\rangle & \text{for } I_2 \geq 0 \\ 0 & \text{else,} \end{cases} \tag{5.71}$$

where p_X is the probability density function for the random variable X and K_0 is the zeroth-order modified Bessel function of the second kind. The second result follows from taking the speckled speckle to be negative exponentially distributed given the mean irradiance, which is itself taken to be negative exponentially distributed. We can carry this analysis another step to find the speckled speckled speckle distribution:

$$p_{I_3}(I_3) = \begin{cases} G_{0,3}^{3,0}\left(I_3/\langle I_1\rangle \mid 0,0,0\right)/\langle I_1\rangle & \text{for } I_3 \geq 0 \\ 0 & \text{else,} \end{cases} \tag{5.72}$$

where $G_{p,q}^{m,n}$ is the Meijer G function [28]. All three are plotted in Fig. 5-2 with the first mean normalized to 1. It can be seen that each diffuser increases the variance of the resulting distribution. In fact, the means and variances can be calculated numerically from these distributions, and we find them to be in complete accordance with our earlier CW results, leading to ordinary, $3\times$ ordinary, and $7\times$ ordinary speckle strength at each respective plane. As one might expect, these three cases follow a pattern that generalizes to an arbitrary number of diffusers. For n diffusers where n

105

is any positive integer, we have

$$
p_{I_n}(I_n) = \begin{cases} G_{0,n}^{n,0}\left(I_n/\langle I_1\rangle \mid 0,\ldots,0\right)/\langle I_1\rangle & \text{for } I_n \geq 0 \\ 0 & \text{else.} \end{cases} \tag{5.73}
$$

This can be proven inductively using standard properties of the Meijer G function [29]. All three of the examples above serve as base cases, and the inductive step follows from $p_{I_{n+1}}(w) = 0$ for $w < 0$ and

$$
p_{I_{n+1}}(w) = \int_0^\infty \mathrm{d}z\, p_{I_n}(z)\exp(-w/z)/z \tag{5.74}
$$

$$
= \int_0^\infty \mathrm{d}z\, G_{0,n}^{n,0}(z \mid 0,\ldots,0)\exp(-w/z)/z \tag{5.75}
$$

$$
= \int_0^\infty \mathrm{d}x\, G_{0,n}^{n,0}(1/x \mid 0,\ldots,0)\exp(-wx)/x \tag{5.76}
$$

$$
= \int_0^\infty \mathrm{d}x\, G_{n,0}^{0,n}(x \mid 1,\ldots,1)\exp(-wx)/x \tag{5.77}
$$

$$
= G_{n+1,0}^{0,n+1}(1/w \mid 1,1,\ldots,1) \tag{5.78}
$$

$$
= G_{0,n+1}^{n+1,0}(w \mid 0,0,\ldots,0), \tag{5.79}
$$

for $w \geq 0$, where Eqs. (5.77)–(5.79) make use of those standard properties. The mth moment can also be found from known properties of G:

$$
\int_0^\infty \mathrm{d}z\, z^m\, G_{0,n}^{n,0}(z \mid 0,\ldots,0) = (\Gamma(m+1))^n = (m!)^n, \tag{5.80}
$$

from which it follows that the nth bounce in the CW small-reflector limit will experience $(2^n - 1)\times$ ordinary speckle strength.

More interesting than the CW case, however, this small-reflector limit allows us to analyze the speckle statistics at planes 2 and 3 for the modulated case. Following our earlier analysis of the modulated case, we can trivially take the initial illumination to be space-time factorable, so that the speckle at plane 1 has the variance given in Eq. (5.27). Now, we assume a narrow-enough initial illumination such that $I_0(\boldsymbol{\rho}_0) \approx$
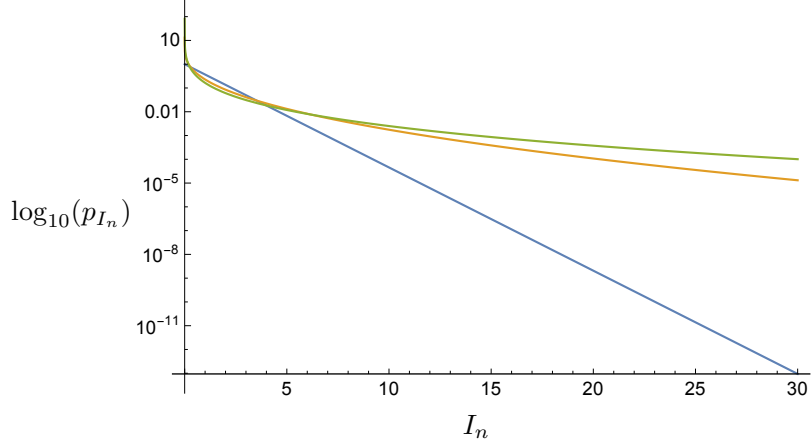
Figure 5-2: Plot of the probability density functions for the small-reflector-limit irradiances at planes 1 (blue), 2 (orange), and 3 (green). The vertical axis is $\log_{10}$ scale, and the first mean has been normalized to 1.

$P\delta(\boldsymbol{\rho}_0)$, which reduces the result to

$$\langle|\tilde{\mathcal{P}}_1(\boldsymbol{\rho}_1,\omega_-)|^2\rangle_0 - |\mathcal{P}_1(\boldsymbol{\rho}_1,\omega_-)|^2 = \left|\frac{P}{L^2}\int\frac{\mathrm{d}\omega_+}{2\pi}\,\mathcal{S}(\omega_+ + \omega_-/2)\mathcal{S}^*(\omega_+ - \omega_-/2)\right|^2$$

(5.81)

$$= \left|\frac{1}{L^2}\int\mathrm{d}^2\boldsymbol{\rho}_0\,\mathcal{P}_0(\boldsymbol{\rho}_0,\omega_-)\right|^2$$

(5.82)

$$= |\mathcal{P}_1(\boldsymbol{\rho}_1,\omega_-)|^2,$$

(5.83)

i.e., there is ordinary speckle at plane 1.

For plane 2, we proceed as before using the central limit theorem, Gaussian mo-

107

ment factoring, and the law of iterated expectation:

$$
\langle |\tilde{\mathcal{P}}_2(\boldsymbol{\rho}_2, \omega_-)|^2 \rangle_1
$$
$$
= \int \frac{\mathrm{d}\omega_+}{2\pi} \int \frac{\mathrm{d}\tilde{\omega}_+}{2\pi}
$$
$$
\langle \mathcal{E}_2(\boldsymbol{\rho}_2, \omega_+ + \omega_-/2) \mathcal{E}_2^*(\boldsymbol{\rho}_2, \omega_+ - \omega_-/2) \mathcal{E}_2^*(\boldsymbol{\rho}_2, \tilde{\omega}_+ + \omega_-/2) \mathcal{E}_2(\boldsymbol{\rho}_2, \tilde{\omega}_+ - \omega_-/2) \rangle_1
$$
$$
= \int \frac{\mathrm{d}\omega_+}{2\pi} \int \frac{\mathrm{d}\tilde{\omega}_+}{2\pi}
$$
$$
\Big[\langle \mathcal{E}_2(\boldsymbol{\rho}_2, \omega_+ + \omega_-/2) \mathcal{E}_2^*(\boldsymbol{\rho}_2, \omega_+ - \omega_-/2) \rangle_1 \langle \mathcal{E}_2^*(\boldsymbol{\rho}_2, \tilde{\omega}_+ + \omega_-/2) \mathcal{E}_2(\boldsymbol{\rho}_2, \tilde{\omega}_+ - \omega_-/2) \rangle_1
$$
$$
+ \langle \mathcal{E}_2(\boldsymbol{\rho}_2, \omega_+ + \omega_-/2) \mathcal{E}_2^*(\boldsymbol{\rho}_2, \tilde{\omega}_+ + \omega_-/2) \rangle_1 \langle \mathcal{E}_2^*(\boldsymbol{\rho}_2, \omega_+ - \omega_-/2) \mathcal{E}_2(\boldsymbol{\rho}_2, \tilde{\omega}_+ - \omega_-/2) \rangle_1 \Big].
$$
$$
\tag{5.84}
$$

The relevant Fresnel diffraction formula is now

$$
\mathcal{E}_2(\boldsymbol{\rho}_2, \omega) = \frac{e^{i\frac{(\omega_0+\omega)L}{c}}}{i\lambda_0 L} \int \mathrm{d}^2\boldsymbol{\rho}_1 \, \mathcal{E}_1(\boldsymbol{\rho}_1, \omega) e^{i\frac{\omega_0+\omega}{2cL}|\boldsymbol{\rho}_2-\boldsymbol{\rho}_1|^2} e^{i\frac{\omega_0+\omega}{c}h_1(\boldsymbol{\rho}_1)} e^{-\frac{4}{d_1^2}|\boldsymbol{\rho}_1|^2}. \tag{5.85}
$$

So we have

$$
\langle \mathcal{E}_2(\boldsymbol{\rho}_2, \omega_+ + \omega_-/2) \mathcal{E}_2^*(\boldsymbol{\rho}_2, \omega_+ - \omega_-/2) \rangle_1
$$
$$
= \frac{e^{i\frac{\omega_- L}{c}}}{L^2} \int \mathrm{d}^2\boldsymbol{\rho}_1 \, \mathcal{E}_1(\boldsymbol{\rho}_1, \omega_+ + \omega_-/2) \mathcal{E}_1^*(\boldsymbol{\rho}_1, \omega_+ - \omega_-/2) e^{i\frac{\omega_-}{2cL}|\boldsymbol{\rho}_2-\boldsymbol{\rho}_1|^2} e^{-\frac{8}{d_1^2}|\boldsymbol{\rho}_1|^2}. \tag{5.86}
$$

Now we take the pupil to be small so that $\exp\left(-8|\boldsymbol{\rho}_1|^2/d_1^2\right) \approx \pi d_1^2 \delta(\boldsymbol{\rho}_1)/8$ can be used in Eq. (5.86). From this it follows that

$$
\langle \mathcal{E}_2(\boldsymbol{\rho}_2, \omega_+ + \omega_-/2) \mathcal{E}_2^*(\boldsymbol{\rho}_2, \omega_+ - \omega_-/2) \rangle_1
$$
$$
= \frac{\pi d_1^2}{8L^2} e^{i\frac{\omega_- L}{c}} e^{i\frac{\omega_-}{2cL}|\boldsymbol{\rho}_2|^2} \mathcal{E}_1(\mathbf{0}, \omega_+ + \omega_-/2) \mathcal{E}_1^*(\mathbf{0}, \omega_+ - \omega_-/2). \tag{5.87}
$$

Similar calculations follow for the other moments, with the result being that

$$
\langle|\tilde{\mathcal{P}}_2(\boldsymbol{\rho}_2,\omega_-)|^2\rangle_1 = \frac{\pi^2 d_1^4}{32L^4} \int \frac{\mathrm{d}\omega_+}{2\pi} \int \frac{\mathrm{d}\tilde{\omega}_+}{2\pi}\, \mathcal{E}_1(\mathbf{0},\omega_+ + \omega_-/2)\mathcal{E}_1^*(\mathbf{0},\omega_+ - \omega_-/2)
$$

$$
\times\, \mathcal{E}_1^*(\mathbf{0},\tilde{\omega}_+ + \omega_-/2)\mathcal{E}_1(\mathbf{0},\tilde{\omega}_+ - \omega_-/2) \tag{5.88}
$$

$$
= \frac{\pi^2 d_1^4}{32L^4}\, |\mathcal{P}_1(\mathbf{0},\omega_-)|^2\,, \tag{5.89}
$$

and so

$$
\langle|\tilde{\mathcal{P}}_2(\boldsymbol{\rho}_2,\omega_-)|^2\rangle_{0,1} = \frac{\pi^2 d_1^4}{32L^4}\, |\mathcal{P}_1(\mathbf{0},\omega_-)|^2\,. \tag{5.90}
$$

For the squared mean, a similar analysis—without the need for Gaussian moment factoring—yields

$$
|\mathcal{P}_2(\boldsymbol{\rho}_2,\omega_-)|^2 = \frac{\pi^2 d_1^4}{64L^4}\, |\mathcal{P}_1(\mathbf{0},\omega_-)|^2\,, \tag{5.91}
$$

which combined with our ordinary-speckle result for plane 1, namely

$$
\langle|\tilde{\mathcal{P}}_1(\boldsymbol{\rho}_1,\omega_-)|^2\rangle_0 = 2\,|\mathcal{P}_1(\boldsymbol{\rho}_1,\omega_-)|^2\,, \tag{5.92}
$$

leads to

$$
\langle|\tilde{\mathcal{P}}_2(\boldsymbol{\rho}_2,\omega_-)|^2\rangle_{0,1} = 4\,|\mathcal{P}_2(\boldsymbol{\rho}_2,\omega_-)|^2\,, \tag{5.93}
$$

i.e., that the speckle variance at plane 2 is 3× as strong as that of ordinary speckle. The above analysis can be repeated for plane 3 by changing subscripts appropriately with the result that the extra factor of 2 in this last step will stack and leave

$$
\langle|\tilde{\mathcal{P}}_3(\boldsymbol{\rho}_3,\omega_-)|^2\rangle_{0,1,2} = 8\,|\mathcal{P}_3(\boldsymbol{\rho}_3,\omega_-)|^2\,, \tag{5.94}
$$

i.e., that the speckle variance at plane 3 is 7× as strong as that of ordinary speckle. Accordingly, it's clear that in this small-reflector limit, the modulated speckle for a

nth bounce return will have a speckle variance that is $(2^n - 1)\times$ as strong as that of ordinary speckle, just as in the CW case.

Chapter 6

Summary and Future Work

In summary, we have presented a complete light transport model, in phasor-field terms, capable of describing propagation through a transmissive, paraxial geometry—including intervening occluders, specular-plus-diffuser masks, and lenses—that serves as an unfolded proxy for occlusion-aided, three-bounce NLoS imaging. For imaging purely-diffuse objects without intervening occluders, we phrased our analysis in terms of the $\mathcal{P}$ field and provided a straightforward derivation of its propagation behavior, analogous to that reported by Reza *et al.* [9], as well as its interaction with a variety of lens configurations. To handle more general propagation scenarios, we introduced and presented propagation primitives for the two-frequency spatial Wigner distribution (TFSWD). With these in hand, we turned our attention to the task of diffuse-object, occlusion-aided imaging and arrived at closed-form results for occlusion-aided imaging with unmodulated light using either a Gaussian-pinhole occluder or a Gaussian-pinspeck occluder. Inspired by observations from this scenario, we abstracted its most significant component, deriving a $\mathcal{P}$-field input-output relation for occluder-interrupted post-diffuser propagation, which enabled us to derive simplified, intuitive behavior in the geometric-optics limit.

Our results show that imaging unoccluded diffuse objects with unmodulated light is not possible in the paraxial regime, but phasor-field imaging provides techniques for image construction if modulated light is used or object occlusion can be exploited. For imaging non-occluded diffuse objects with modulated light, spatial resolution is

the diffraction limit at the modulation frequency. For occlusion-aided imaging of the same object with unmodulated light, spatial resolution is set by the optical-frequency diffraction limit of the occluder. Although the latter can be far superior to the former, blind determination of the occluder's characteristics poses a challenge for exploiting its presence, and even with a known occluder, imaging performance will be limited by its size and shape.

Mindful of the limitations of our paraxial assumption, we have derived nonparaxial post-diffuser propagation primitives for the $\mathcal{P}$ field and, equivalently, the diffuser-averaged STA irradiance using the Rayleigh–Sommerfeld diffraction integral for the complex field envelope. We have also proposed nonparaxial free-space propagation primitives for the 6D light field and, equivalently, the TFSWD. Our proposal was inspired by applying geometric intuition to our result for the Fresnel limit, and its validity is suggested by the fact that it reproduces our derived propagation result for the diffuser-averaged STA irradiance. We then provided a more formal derivation of this primitive using the angular-spectrum representation of the complex field envelope under certain constraints on the relevant correlation functions. Pushing past these constraints, we provided a more general characterization of TFSWD behavior by deriving a set of differential equations it obeys.

Returning to the paraxial regime, we then explored the impacts of speckle. We provided an analysis of third-order speckle for unmodulated illumination and first-order speckle for modulated illumination. For the unmodulated case, our results are promising as we find the geometry of typical NLoS scenarios is likely to minimize most of the final speckle and the finite size of the detector is likely to average out the rest. We also established that time-averaged illumination techniques provide another method for speckle management. For the modulated case, we found that the zero-frequency speckle for space-time factorable illumination is no stronger than ordinary speckle. By analyzing a specific, asymptotically single-frequency signal, we were able to demonstrate this bound in addition to establishing the validity of Teichman's [27] result that the modulation-frequency-component speckle is in general stronger than ordinary speckle. On a positive note, although Teichman's result appears valid, our

analysis suggests that in practice any speckle enhancement effect is likely to be minimal, leaving us to conclude that modulated first-order speckle is probably about as strong as ordinary speckle.

Considering the correlation length of first-order modulated speckle, we concluded that it is likely to be averaged out by realistic detectors. Using semiclassical photodetection theory, we demonstrated that the effect of finite-aperture detectors integrating over multiple speckles is such that, for realistic parameter values, the imposed excess noise is either negligible or it sets a very high ultimate limit on the measurement's SNR. Finally, considering small-reflector geometries, we derived the full irradiance distribution and all its moments for arbitrary-order speckle in the CW case. For the modulated case, we derived the first and second moments of arbitrary-order modulated-component speckle. In both cases, we find the nth order speckle variance to be $(2^n - 1)\times$ as strong as that of ordinary speckle.

Although we have covered considerable ground in providing a formal analysis of phasor-field imaging, there are many topics suitable for future research. Regarding our forward-model framework, it would be appealing to reframe our result for occluder-interrupted propagation to account for nonparaxial behavior. A straightforward extension seems untenable, but approximations afforded by the geometric-optics limit may prove favorable. More generally, it would be ideal to find a TFSWD propagation primitive for arbitrary linear transformations of the underlying field. Such a primitive could capture all of our phasor-field propagation results, e.g., for free space, masks, and lenses, while expanding the range of applicability to other optical components like frequency-dependent filters. It might also enable us to handle nontrivial elements of the NLoS geometry, such as nonplanar targets and angled walls. Regarding speckle, a pressing open question is how higher-order modulated speckle behaves in more typical NLoS geometries. Our analysis of the modulated case has also left out methods for speckle reduction. Additionally, it seems worthwhile to design and execute experiments to investigate to what extent if any the effects of speckle are actually present in NLoS imaging scenarios, modulated or otherwise.

Notably, our imaging analysis has left out a proposal for how occlusion might

be leveraged synergistically with modulated light. Future research would do well to consider this question. One complication is that the convolutional image formed by the occluder is recovered by imaging the final diffuser, whereas the image formed from the $\mathcal{P}$ field modulation is accessed by focusing, either physically or computationally, through the final diffuser onto the hidden target plane. A synergistic approach would need to determine where to focus, perhaps on the final diffuser to recover the occlusion-aided image and then use computational techniques to extract the $\mathcal{P}$-field image. Another complication is that the resolution provided by either of these reconstruction modalities may dominate the other. For example, in cursory numerical analysis of discretized-forward-model singular values for simple occluded, modulated cases—not included in this thesis—we found that the addition of centimeter-scale occluders seemed to add little benefit to the already significant conditioning provided by centimeter-scale modulation. This finding is tentative though, and further consideration of this topic is merited. Those looking to leverage both occlusion and modulation might look into the possibility of imaging an unknown occluder via modulated illumination and then leveraging its now known properties to form better images of the scene behind it.

Finally, the most exciting avenue opened by this work is the possibility of imaging around the corner with physical optics. Experimental demonstrations of our theoretical proposals for focusing, projecting, and imaging the $\mathcal{P}$ field through intervening diffuse transmission or reflection with actual lenses would be very inspiring. As noted in that analysis, our mathematics assumed rather large lenses, which can be alleviated while improving resolution by increasing the $\mathcal{P}$-field frequency. For the standard modulate-and-detect approach to $\mathcal{P}$-field imaging, the accessible $\mathcal{P}$ field frequency is likely to be limited by the bandwidth of available detectors. At optical wavelengths, fiber-coupled detectors with 40 GHz bandwidth are readily available, and at communications wavelengths, e.g., $\lambda_0 = 1550\,\text{nm}$, detectors with 100 GHz bandwidth can also be obtained today. Experimentalists looking to push past these numbers in physical-optics demonstrations may find it useful to consider the synthetic-wavelength-holography approach we discuss in Appendix D. There, the need for fast

detectors is traded for a requirement to coherently detect at high spatial resolution, but the attainable $\mathcal{P}$-field frequency is in principle only limited by the diffuser surface roughness, which is likely to become significant around 1 THz. The required spatial resolution will be determined by the speckle geometry and the need to avoid signal fading, so initial experiments may consider geometries with small reflectors to ensure the full speckle pattern is resolved at the detector. Detection of light from large reflectors, e.g., entire walls, may need to await technological advances in the resolution of lock-in cameras [30, 31], which combine traditional detector arrays with lock-in amplifiers at each detector element, enabling single-shot spatially-resolved coherent detection. Alternatively, one might consider scanned heterodyne configurations or application of photonic lanterns [32], which couple light from a multi-mode fiber into many individual single-mode fibers.

Appendix A

Non-Line-of-Sight Geometry
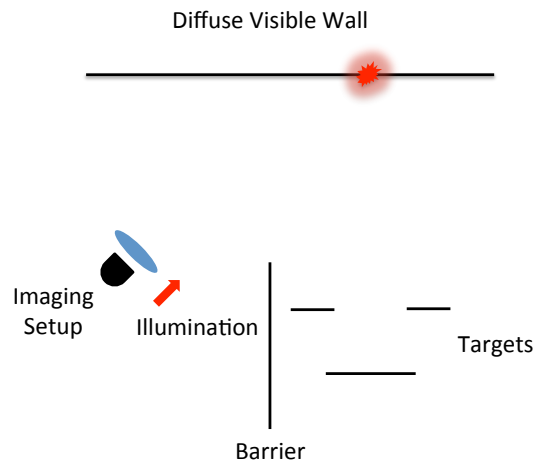
Figure A-1: An example of a typical NLoS geometry. Laser illumination is focused on a small spot on a diffuse visible wall which in turn flood illuminates a scene of diffuse reflecting targets. The returned light is detected by an optical configuration that images the visible wall.

Throughout this thesis, we have made exclusive use of transmissive geometries. In practice, NLoS scenarios are often entirely reflective geometries. This may seem like the most significant shortcoming of our framework for application to seeing around corners. However, as we will show now, our transmissive framework can be adapted to address typical reflective NLoS geometries. Consider the typical NLoS scenario depicted in Fig. A-1. Incident laser illumination is focused on a small spot on a diffuse reflecting visible wall which in turn flood illuminates a scene of diffuse reflecting

117

targets. These targets then reflect some light back to the visible wall, which is then imaged by a detector together with imaging optics. If we take the initial illumination spot on the visible wall to have small spatial extent, as is often the case, and we assume that the resolution of the imaging optics suffices to capture all relevant detail of the diffuser-averaged STA irradiance at the visible wall, then the first and final bounces in the light's path can effectively be ignored. What remains is to understand the $\mathcal{P}$-field input-output relation for point-source illumination at the plane of the visible wall propagating into the scene and returning back to the visible wall.

If the scene can be approximated by a set of fronto-planar facets, then a simple transmissive analogy can be readily applied. In our example, we've depicted three opaque, diffuse, fronto-planar targets at two planes, which we'll call planes 1 and 2. If we temporarily imagine time gating our detection so that we only see return light from the first plane, the transmissive analogy is obvious. Focused illumination is incident upon a diffuser, propagates a distance, then falls upon a transmissivity mask $T_1(\boldsymbol{\rho}_1)$ which takes the value 0 wherever no target is present and takes on values according to the albedo patterns of each target at their locations. This mask is butted up against another diffuser which represents the diffuse reflectivity of the target. The illumination then continues propagating a final distance corresponding to the return trip to the visible wall.

Now imagine time gating our detection so as to only see return light from the second target plane. In that case the transmissive analogy would be that focused illumination passes through a diffuser, propagates a distance to plane 1, is blocked by an occlusion mask $P_1(\boldsymbol{\rho}_1)$ that takes the value 0 wherever a target is present at plane 1 and 1 otherwise, propagates another distance to plane 2, passes through a transmissivity mask $T_2(\boldsymbol{\rho}_2)$ and diffuser, propagates back to plane 1 where it is once again occluded by $P_1(\boldsymbol{\rho}_1)$, and then propagates a final distance accounting for the return trip to the visible wall. The actual detected diffuser-averaged STA irradiance pattern will be a sum of these two scenarios, as each incurs the appropriate roundtrip time delays. By the linearity of the Fourier transform, the resulting $\mathcal{P}$ field is also

118

just a sum of the output $\mathcal{P}$ field from each of these transmissive scenarios. That is

$$\mathcal{P}_{\text{out}}(\boldsymbol{\rho}_{\text{out}}, \omega_-) = \sum_n \mathcal{P}_{\text{out}_n}(\boldsymbol{\rho}_{\text{out}}, \omega_-), \tag{A.1}$$

where each $\mathcal{P}_{\text{out}_n}$ represents the output from one of these transmissive analogies, as depicted in Fig. A-2.
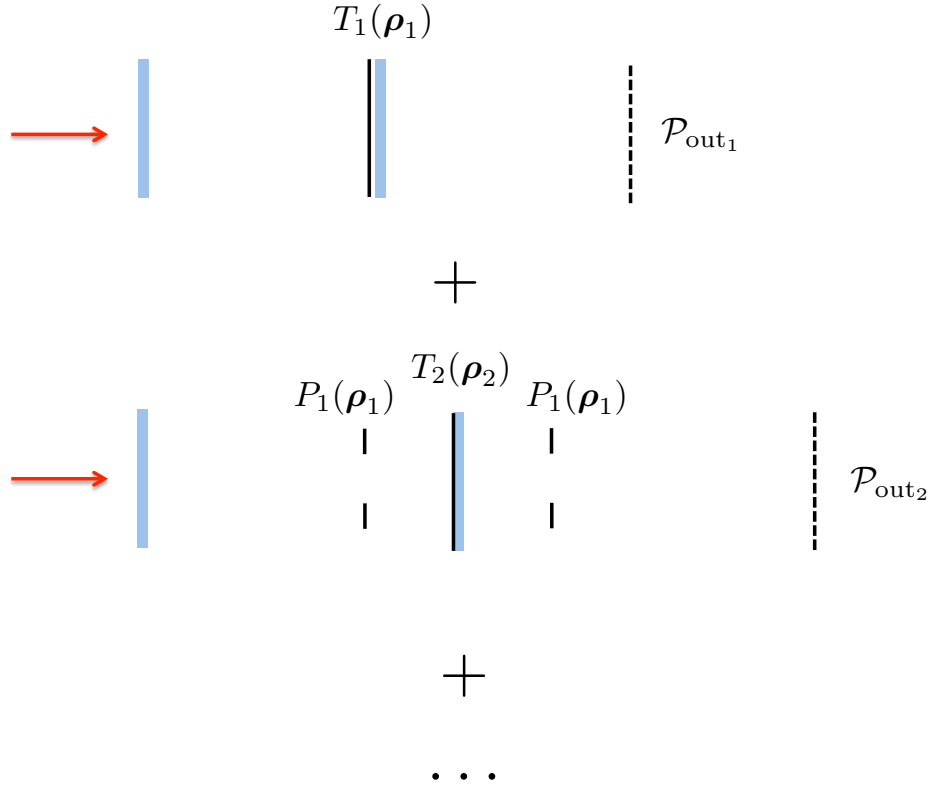
Figure A-2: A sum of transmissive geometries that encapsulates the relevant behavior of our example NLoS geometry.

In general, there may be many more transmissive geometries that need to be considered, e.g., if there are many planes containing targets. Even in our simple two-plane scenario, one might argue that light could reflect off the target in plane 2, then off the backs of the targets in plane 1, then back off of the target in plane 2 before returning to the visible wall. Although this scenario could be depicted with an appropriate higher-order transmissive diagram, it represents a fifth-bounce geometry, which is in general much weaker than the third-bounce geometry that our original

intent was to model with the Fig. A-1 setup.

Nondiffuse targets can also be modeled with appropriate use of the specular-plus-diffuser masks we discussed in Chapter 3, as can partially transparent targets. The main drawback to this approach then, beyond its complexity, is its inability to deal with angled targets, which might reflect the illumination off axis, or nonplanar targets more generally. This approach to NLoS modeling will also be frustrated if the visible wall is not purely diffuse, or if we don't wish to use such simple techniques for initial illumination and final detection—e.g., if we want to use the $\mathcal{P}$-field projecting and direct-imaging techniques discussed at the end of Chapter 2—as the significant angle that the source and detector make with the visible wall will then be relevant. Some of these issues may be manageable within the transmissive framework and undoubtedly some may not. We leave these issues open as a worthwhile topic for future research.

Appendix B

The Limits of Cascading Propagation

In Chapter 3 we argued that the $\mathcal{P}$ field alone does not suffice to explain propagation starting from planes that contain spatial coherence, i.e., that are not a pure diffusive element which destroys the coherence accumulated from any preceding propagation. The upshot of this fact is that one cannot draw up a set of $\mathcal{P}$-field propagation primitives that correctly derive the $\mathcal{P}$-field input-output relation for a general, complex geometry such as that in Fig. 3-1 by means of propagating the $\mathcal{P}$ field piecemeal to and from arbitrarily chosen planes of interest. The analysis presented in Sec. 3.4, however, may lead one to believe that such a simplified $\mathcal{P}$-field-only propagation intuition can be relied upon at least in some limit, e.g., the geometric-optics limit. Nonetheless, a very simple example suggests that such is not the case.

Consider analyzing the scenario from Sec. 3.4 by naively propagating the $\mathcal{P}$ field to and from the intervening occluder-containing plane. Using $\hat{\mathcal{P}}_2(\boldsymbol{\rho}_2, \omega_-)$ to denote the putative $\mathcal{P}$ field obtained by this procedure, we have that

$$
\hat{\mathcal{P}}_2(\boldsymbol{\rho}_2, \omega_-) = \frac{e^{i\omega_-(L_1+L_2)/c}}{L_1^2 L_2^2} \int \mathrm{d}^2\boldsymbol{\rho}_1 \, e^{i\frac{\omega_-}{2cL_2}|\boldsymbol{\rho}_2-\boldsymbol{\rho}_1|^2} |P(\boldsymbol{\rho}_1)|^2 \int \mathrm{d}^2\boldsymbol{\rho}_0 \, e^{i\frac{\omega_-}{2cL_1}|\boldsymbol{\rho}_1-\boldsymbol{\rho}_0|^2} \mathcal{P}_0(\boldsymbol{\rho}_0, \omega_-)
$$

$$\tag{B.1}$$

$$
= \frac{e^{i\omega_-(L_1+L_2)/c}}{L_1^2 L_2^2} e^{i\frac{\omega_-}{2cL_2}|\boldsymbol{\rho}_2|^2} \int \mathrm{d}^2\boldsymbol{\rho}_0 \, e^{i\frac{\omega_-}{2cL_1}|\boldsymbol{\rho}_0|^2} \mathcal{P}_0(\boldsymbol{\rho}_0, \omega_-)
$$

$$
\times \int \mathrm{d}^2\boldsymbol{\rho}_1 \, e^{i\frac{\omega_-}{2c}|\boldsymbol{\rho}_1|^2\left(\frac{1}{L_1}+\frac{1}{L_2}\right)} |P(\boldsymbol{\rho}_1)|^2 e^{-i\frac{\omega_-}{c}\boldsymbol{\rho}_1\cdot\left(\frac{\boldsymbol{\rho}_0}{L_1}+\frac{\boldsymbol{\rho}_2}{L_2}\right)}.
$$

$$\tag{B.2}$$

Defining

$$\mathcal{T}(\mathbf{k}) \equiv \int d^2\boldsymbol{\rho}\, |P(\boldsymbol{\rho})|^2 \exp\left(-i\mathbf{k}\cdot\boldsymbol{\rho}\right) \tag{B.3}$$

to be the Fourier transform of $|P(\boldsymbol{\rho})|^2$, and

$$\mathcal{G}(\mathbf{k}) \equiv \exp\left(-i\frac{c}{2\omega_-}\frac{L_1 L_2}{L_1 + L_2}|\mathbf{k}|^2\right), \tag{B.4}$$

we can reduce Eq. (B.2) to

$$\hat{\mathcal{P}}_2(\boldsymbol{\rho}_2,\omega_-) = \frac{i2\pi c}{\omega_-}\frac{1}{L_1 L_2}\frac{e^{i\omega_-(L_1+L_2)/c}}{L_1+L_2}e^{i\frac{\omega_-}{2cL_2}|\boldsymbol{\rho}_2|^2}$$
$$\int d^2\boldsymbol{\rho}_0\, e^{i\frac{\omega_-}{2cL_1}|\boldsymbol{\rho}_0|^2}\mathcal{P}_0(\boldsymbol{\rho}_0,\omega_-)\mathcal{H}\left(\frac{\omega_-}{c}\left(\frac{\boldsymbol{\rho}_0}{L_1}+\frac{\boldsymbol{\rho}_2}{L_2}\right)\right), \tag{B.5}$$

where

$$\mathcal{H}(\mathbf{k}) \equiv \int \frac{d^2\mathbf{k}'}{(2\pi)^2}\,\mathcal{T}(\mathbf{k}')\mathcal{G}(\mathbf{k}-\mathbf{k}'), \tag{B.6}$$

is the convolution of $\mathcal{T}$ and $\mathcal{G}$. Paralleling our previous analysis we take $\mathcal{T}$ to be of nominal width $1/\sigma$. Note that $\mathcal{G}$ is of nominal extent $|\mathbf{k}| \leq \frac{\omega_-}{c}\frac{L_1+L_2}{L_1 L_2}$, in that it becomes highly oscillatory for $|\mathbf{k}| > \frac{\omega_-}{c}\frac{L_1+L_2}{L_1 L_2}$. Thus the geometric-optics limit from Sec. 3.4—in which $\Omega_1 + \Omega_2 \gg 1$—is precisely the limit in which $\mathcal{T}$ is very narrow compared to $\mathcal{G}$, so that $\mathcal{T}$ behaves like a delta function in the convolution. In such a limit, the $\mathcal{T}$ dependence in Eq. (B.5) vanishes, leaving behind at most a constant, which clearly can't be valid outside of the trivial cases of an infinite, uniformly-attenuating mask or the absence of any mask. Even so, consider the latter case, in which there is no intervening occluder and we are effectively trying to build up free-space Fresnel propagation for the $\mathcal{P}$ field by propagating to and from an arbitrary intermediate free-space plane. In that case we know the correct answer is given by

$$\mathcal{P}_2(\boldsymbol{\rho}_2,\omega_-) = \frac{e^{i\omega_- L_T/c}}{L_T^2}\int d^2\boldsymbol{\rho}_0\, e^{i\frac{\omega_-}{2cL_T}|\boldsymbol{\rho}_2-\boldsymbol{\rho}_0|^2}\mathcal{P}_0(\boldsymbol{\rho}_0,\omega_-), \tag{B.7}$$

where $L_T = L_1 + L_2$. The result predicted by our piecemeal analysis however is

$$
\begin{aligned}
\hat{\mathcal{P}}_2(\boldsymbol{\rho}_2, \omega_-) =& \frac{i2\pi c}{\omega_-} \frac{1}{L_1 L_2} \frac{e^{i\omega_-(L_1+L_2)/c}}{L_1 + L_2} e^{i\frac{\omega_-}{2cL_2}|\boldsymbol{\rho}_2|^2} \\
& \int \mathrm{d}^2\boldsymbol{\rho}_0 \, e^{i\frac{\omega_-}{2cL_1}|\boldsymbol{\rho}_0|^2} \mathcal{P}_0(\boldsymbol{\rho}_0, \omega_-) e^{-i\frac{\omega_-}{2c}\frac{L_1 L_2}{L_1+L_2}\left(\frac{\boldsymbol{\rho}_0}{L_1}+\frac{\boldsymbol{\rho}_2}{L_2}\right)} & \text{(B.8)} \\
=& \frac{i2\pi c}{\omega_-} \frac{1}{L_1 L_2} \frac{e^{i\omega_-(L_1+L_2)/c}}{L_1 + L_2} \int \mathrm{d}^2\boldsymbol{\rho}_0 \, e^{i\frac{\omega_-}{2c(L_1+L_2)}|\boldsymbol{\rho}_2-\boldsymbol{\rho}_0|^2} \mathcal{P}_0(\boldsymbol{\rho}_0, \omega_-) & \text{(B.9)} \\
=& \frac{i2\pi c}{\omega_-} \frac{L_1 + L_2}{L_1 L_2} \mathcal{P}_2(\boldsymbol{\rho}_2, \omega_-). & \text{(B.10)}
\end{aligned}
$$

This prediction differs from the correct result by a factor that depends not only on the distances to and from the intermediate plane used but on the modulation frequency as well. For any modulation that isn't single frequency, this implies that the piecemeal analysis predicts a modulation shape distortion relative to the true result. So, this sort of piecemeal analysis simply cannot be relied on. It is worth noting however, by contrast, the Fresnel propagation primitive for the underlying optical field *does* permit this sort of cascaded construction. That $\mathcal{P}$-field propagation can't be built up in this way is a demonstration of the fact that the $\mathcal{P}$ field does not obey the sort of wave equation that the underlying optical field does, as one may easily be misled into believing. By contrast, the TFSWD propagation primitive does permit cascaded construction. Moreover, the evolution of the space-time autocorrelation function, which is equivalent to the TFSWD in information content, can be characterized by a pair of differential equations [22, 25]. So, it should be possible to write down differential equations for the TFSWD (or 6D light field) in analogy to the wave equation. This idea is explored in Chapter 4.

Appendix C

TFSWD-Primitive Derivations

In this appendix we provide derivations for the TFSWD's propagation primitives given earlier in Eqs. (3.15)–(3.18).

C.1   Propagation Through a Diffuser

Consider propagation through one of our diffusers: assume that we know $W_{\mathcal{E}_z}(\boldsymbol{\rho}_+, \mathbf{k}, \omega_+, \omega_-)$ and we want to find $W_{\mathcal{E}_z'}(\boldsymbol{\rho}_+, \mathbf{k}, \omega_+, \omega_-)$, where, for $(z, k) = (0, 0), (L_1, 1), (L_1 + L_2, 2)$,

$$\mathcal{E}_z'(\boldsymbol{\rho}, \omega) = \mathcal{E}_z(\boldsymbol{\rho}, \omega)e^{i(\omega_0+\omega)h_k(\boldsymbol{\rho})/c} \approx \mathcal{E}_z(\boldsymbol{\rho}, \omega)e^{i\omega_0 h_k(\boldsymbol{\rho})/c}, \tag{C.1}$$

with

$$\langle e^{i\omega_0[h_k(\boldsymbol{\rho})-h_k(\boldsymbol{\rho}')]/c} \rangle \approx \lambda_0^2 \delta(\boldsymbol{\rho} - \boldsymbol{\rho}'). \tag{C.2}$$

125

In this case we immediately get

$$
W_{\mathcal{E}_z'}(\boldsymbol{\rho}_+, \mathbf{k}, \omega_+, \omega_-) = \int \mathrm{d}^2\boldsymbol{\rho}_- e^{-i\mathbf{k}\cdot\boldsymbol{\rho}_-}
$$
$$
\times \langle \mathcal{E}_z'(\boldsymbol{\rho}_+ + \boldsymbol{\rho}_-/2, \omega_+ + \omega_-/2)\mathcal{E}_z'^*(\boldsymbol{\rho}_+ - \boldsymbol{\rho}_-/2, \omega_+ - \omega_-/2)\rangle
$$
$$
\tag{C.3}
$$

$$
= \int \mathrm{d}^2\boldsymbol{\rho}_- \, e^{-i\mathbf{k}\cdot\boldsymbol{\rho}_-}
$$
$$
\times \langle \mathcal{E}_z(\boldsymbol{\rho}_+ + \boldsymbol{\rho}_-/2, \omega_+ + \omega_-/2)\mathcal{E}_z^*(\boldsymbol{\rho}_+ - \boldsymbol{\rho}_-/2, \omega_+ - \omega_-/2)\rangle
$$
$$
\times \langle e^{i\omega_0[h_z(\boldsymbol{\rho}_+ + \boldsymbol{\rho}_-/2) - h_k(\boldsymbol{\rho}_+ - \boldsymbol{\rho}_-/2)]/c}\rangle
\tag{C.4}
$$

$$
= \lambda_0^2 \langle \mathcal{E}_z(\boldsymbol{\rho}_+, \omega_+ + \omega_-/2)\mathcal{E}_z^*(\boldsymbol{\rho}_+, \omega_+ - \omega_-/2)\rangle
\tag{C.5}
$$

$$
= \lambda_0^2 \int \frac{\mathrm{d}^2\mathbf{k}'}{(2\pi)^2} \, W_{\mathcal{E}_z}(\boldsymbol{\rho}_+, \mathbf{k}', \omega_+, \omega_-).
\tag{C.6}
$$

Physically, the $\mathbf{k}$ dependence of the TFSWD carries the field's spatial-frequency information, i.e., its directionality. The result we have just obtained shows that the diffuser has completely destroyed the directionality of $\mathcal{E}_z(\boldsymbol{\rho}, \omega)$, because $W_{\mathcal{E}_z'}(\boldsymbol{\rho}_+, \mathbf{k}, \omega_+, \omega_-)$ is independent of $\mathbf{k}$.

C.2   Propagation Through a Deterministic Occluder

Now consider propagation through a deterministic transmission mask. Here we want to find $W_{\mathcal{E}_z'}(\boldsymbol{\rho}_+, \mathbf{k}, \omega_+, \omega_-)$ given $W_{\mathcal{E}_z}(\boldsymbol{\rho}_+, \mathbf{k}, \omega_+, \omega_-)$ and a *deterministic* $P(\boldsymbol{\rho})$, where

$$
\mathcal{E}_z'(\boldsymbol{\rho}, \omega) = \mathcal{E}_z(\boldsymbol{\rho}, \omega)P(\boldsymbol{\rho}).
\tag{C.7}
$$

For this case we have that

$$
W_{\mathcal{E}_z'}(\boldsymbol{\rho}_+, \mathbf{k}, \omega_+, \omega_-)
$$
$$
= \int \mathrm{d}^2\boldsymbol{\rho}_- \, \langle \mathcal{E}_z'(\boldsymbol{\rho}_+ + \boldsymbol{\rho}_-/2, \omega_+ + \omega_-/2)\mathcal{E}_z'^*(\boldsymbol{\rho}_+ - \boldsymbol{\rho}_-/2, \omega_+ - \omega_-/2)\rangle e^{-i\mathbf{k}\cdot\boldsymbol{\rho}_-}
\tag{C.8}
$$

$$= \int \mathrm{d}^2\boldsymbol{\rho}_- \left\langle \mathcal{E}_z(\boldsymbol{\rho}_+ + \boldsymbol{\rho}_-/2, \omega_+ + \omega_-/2)\mathcal{E}_z^*(\boldsymbol{\rho}_+ - \boldsymbol{\rho}_-/2, \omega_+ - \omega_-/2) \right\rangle$$

$$\times P(\boldsymbol{\rho}_+ + \boldsymbol{\rho}_-/2)P^*(\boldsymbol{\rho}_+ - \boldsymbol{\rho}_-/2)e^{-i\mathbf{k}\cdot\boldsymbol{\rho}_-} \tag{C.9}$$

$$= \int \frac{\mathrm{d}^2\mathbf{k}'}{(2\pi)^2} W_{\mathcal{E}_z}(\boldsymbol{\rho}_+, \mathbf{k}', \omega_+, \omega_-) \int \mathrm{d}^2\boldsymbol{\rho}_- \, P(\boldsymbol{\rho}_+ + \boldsymbol{\rho}_-/2)P^*(\boldsymbol{\rho}_+ - \boldsymbol{\rho}_-/2)e^{-i(\mathbf{k}-\mathbf{k}')\cdot\boldsymbol{\rho}_-}$$

$$\tag{C.10}$$

$$= \int \frac{\mathrm{d}^2\mathbf{k}'}{(2\pi)^2} W_{\mathcal{E}_z}(\boldsymbol{\rho}_+, \mathbf{k}', \omega_+, \omega_-)W_P(\boldsymbol{\rho}_+, \mathbf{k} - \mathbf{k}'), \tag{C.11}$$

where

$$W_P(\boldsymbol{\rho}_+, \mathbf{k}) \equiv \int \mathrm{d}^2\boldsymbol{\rho}_- \, P(\boldsymbol{\rho}_+ + \boldsymbol{\rho}_-/2)P^*(\boldsymbol{\rho}_+ - \boldsymbol{\rho}_-/2)e^{-i\mathbf{k}\cdot\boldsymbol{\rho}_-} \tag{C.12}$$

is the spatial Wigner distribution of $P(\boldsymbol{\rho})$. In words, Eq. (C.11) shows that multiplying $\mathcal{E}_z(\boldsymbol{\rho}, \omega)$ by a deterministic field-transmission mask implies that $W_{\mathcal{E}_z'}(\boldsymbol{\rho}_+, \mathbf{k}, \omega_+, \omega_-)$ is obtained from a $\mathbf{k}$-space convolution of $W_{\mathcal{E}_z}(\boldsymbol{\rho}_+, \mathbf{k}, \omega_+, \omega_-)$ with the field-transmission mask's spatial Wigner distribution. Moreover, Eq. (C.12), together with Eq. (3.14), immediately leads to

$$\mathcal{P}_z(\boldsymbol{\rho}_+, \omega_-) = \int \frac{\mathrm{d}\omega_+}{2\pi} \int \frac{\mathrm{d}^2\mathbf{k}}{(2\pi)^2} W_{\mathcal{E}_z}(\boldsymbol{\rho}_+, \mathbf{k}, \omega_+, \omega_-) \tag{C.13}$$

$$= \int \frac{\mathrm{d}\omega_+}{2\pi} \int \frac{\mathrm{d}^2\mathbf{k}}{(2\pi)^2} \int \frac{\mathrm{d}^2\mathbf{k}'}{(2\pi)^2} W_{\mathcal{E}_z}(\boldsymbol{\rho}_+, \mathbf{k}', \omega_+, \omega_-)W_P(\boldsymbol{\rho}_+, \mathbf{k} - \mathbf{k}') \tag{C.14}$$

$$= \int \frac{\mathrm{d}\omega_+}{2\pi} \int \frac{\mathrm{d}^2\mathbf{k}'}{(2\pi)^2} W_{\mathcal{E}_z}(\boldsymbol{\rho}_+, \mathbf{k}', \omega_+, \omega_-)|P(\boldsymbol{\rho}_+)|^2 = \mathcal{P}_z(\boldsymbol{\rho}_+, \omega_-)|P(\boldsymbol{\rho}_+)|^2,$$

$$\tag{C.15}$$

as could have been directly obtained from Eq, (C.7) and the $\mathcal{P}$-field's definition.

C.3 Propagation Through a Specular-Plus-Diffuser Mask

Combining the approaches for the diffuser and deterministic transmission mask allows us to model the propagation through a specular-plus-diffuser mask. We take such a

127

mask to be a multiplicative random process $F(\boldsymbol{\rho}_1)$ having nonzero mean $\langle F(\boldsymbol{\rho}_1)\rangle \neq 0$, and covariance, $\langle \Delta F(\boldsymbol{\rho}_+ + \boldsymbol{\rho}_-/2)\Delta F^*(\boldsymbol{\rho}_+ - \boldsymbol{\rho}_-/2)\rangle \approx \lambda_0^2 \mathcal{F}(\boldsymbol{\rho}_+)\delta(\boldsymbol{\rho}_-)$ where $0 \leq \mathcal{F}(\boldsymbol{\rho}_+) \leq 1$ and $\Delta F(\boldsymbol{\rho}) \equiv F(\boldsymbol{\rho}) - \langle F(\boldsymbol{\rho})\rangle$. The propagation analysis follows from combining the two previous analyses:

$$W_{\mathcal{E}_z'}(\boldsymbol{\rho}_+, \mathbf{k}, \omega_+, \omega_-)$$

$$= \int \mathrm{d}^2\boldsymbol{\rho}_- \, \langle \mathcal{E}_z'(\boldsymbol{\rho}_+ + \boldsymbol{\rho}_-/2, \omega_+ + \omega_-/2)\mathcal{E}_z'^*(\boldsymbol{\rho}_+ - \boldsymbol{\rho}_-/2, \omega_+ - \omega_-/2)\rangle e^{-i\mathbf{k}\cdot\boldsymbol{\rho}_-} \tag{C.16}$$

$$= \int \mathrm{d}^2\boldsymbol{\rho}_- \, \langle \mathcal{E}_z(\boldsymbol{\rho}_+ + \boldsymbol{\rho}_-/2, \omega_+ + \omega_-/2)\mathcal{E}_z^*(\boldsymbol{\rho}_+ - \boldsymbol{\rho}_-/2, \omega_+ - \omega_-/2)\rangle$$

$$\times \langle F(\boldsymbol{\rho}_+ + \boldsymbol{\rho}_-/2)F^*(\boldsymbol{\rho}_+ - \boldsymbol{\rho}_-/2)\rangle e^{-i\mathbf{k}\cdot\boldsymbol{\rho}_-}. \tag{C.17}$$

From expanding $F(\boldsymbol{\rho})$ into a sum of its (deterministic) mean and zero-mean random portions, it follows that

$$W_{\mathcal{E}_z'}(\boldsymbol{\rho}_+, \mathbf{k}, \omega_+, \omega_-) = \int \mathrm{d}^2\boldsymbol{\rho}_- \, \langle \mathcal{E}_z(\boldsymbol{\rho}_+ + \boldsymbol{\rho}_-/2, \omega_+ + \omega_-/2)\mathcal{E}_z^*(\boldsymbol{\rho}_+ - \boldsymbol{\rho}_-/2, \omega_+ - \omega_-/2)\rangle$$

$$\times (\langle F(\boldsymbol{\rho}_+ + \boldsymbol{\rho}_-/2)\rangle\langle F^*(\boldsymbol{\rho}_+ - \boldsymbol{\rho}_-/2)\rangle + \langle \Delta F(\boldsymbol{\rho}_+ + \boldsymbol{\rho}_-/2)\Delta F^*(\boldsymbol{\rho}_+ - \boldsymbol{\rho}_-/2)\rangle)e^{-i\mathbf{k}\cdot\boldsymbol{\rho}_-} \tag{C.18}$$

$$= \int \frac{\mathrm{d}^2\mathbf{k}'}{(2\pi)^2} W_{\mathcal{E}_{L_1}}(\boldsymbol{\rho}_+, \mathbf{k}', \omega_+, \omega_-)W_{\langle F\rangle}(\boldsymbol{\rho}_+, \mathbf{k} - \mathbf{k}') + \lambda_0^2 \mathcal{F}(\boldsymbol{\rho}_+) \int \frac{\mathrm{d}^2\mathbf{k}'}{(2\pi)^2} W_{\mathcal{E}_{L_1}}(\boldsymbol{\rho}_+, \mathbf{k}', \omega_+, \omega_-). \tag{C.19}$$

C.4   Fresnel Diffraction

Our final task is to find $W_{\mathcal{E}_L}(\boldsymbol{\rho}_+, \mathbf{k}, \omega_+, \omega_-)$ when

$$\mathcal{E}_L(\boldsymbol{\rho}_L, \omega) = \int \mathrm{d}^2\boldsymbol{\rho}_0 \, \mathcal{E}_0(\boldsymbol{\rho}_0, \omega)\frac{(\omega_0 + \omega)e^{i(\omega_0 + \omega)(L/c + |\boldsymbol{\rho}_L - \boldsymbol{\rho}_0|^2/2cL)}}{i2\pi cL}, \tag{C.20}$$

i.e., for Fresnel diffraction over a distance L [1]. This calculation turns out to be more complicated than its predecessors in this appendix. We start from

$$
\begin{aligned}
W_{\mathcal{E}_L}(\boldsymbol{\rho}_+, \mathbf{k}, \omega_+, \omega_-) &= \int \mathrm{d}^2 \boldsymbol{\rho}_- \int \mathrm{d}^2 \boldsymbol{\rho}_0 \int \mathrm{d}^2 \boldsymbol{\rho}_0' \, \langle \mathcal{E}_0(\boldsymbol{\rho}_0, \omega_+ + \omega_-/2) \mathcal{E}_0^*(\boldsymbol{\rho}_0', \omega_+ - \omega_-/2) \rangle \\
&\quad \times e^{i\omega_- L/c} e^{-i\mathbf{k}\cdot\boldsymbol{\rho}_-} \frac{(\omega_0 + \omega_+ + \omega_-/2) e^{i(\omega_0+\omega_++\omega_-/2)|\boldsymbol{\rho}_++\boldsymbol{\rho}_-/2-\boldsymbol{\rho}_0|^2/2cL}}{i2\pi cL} \\
&\quad \times \frac{(\omega_0 + \omega_+ - \omega_-/2) e^{-i(\omega_0+\omega_+-\omega_-/2)|\boldsymbol{\rho}_+-\boldsymbol{\rho}_-/2-\boldsymbol{\rho}_0'|^2/2cL}}{-i2\pi cL}.
\end{aligned} \tag{C.21}
$$

Exploiting $\Delta\omega \ll \omega_0$, and making the coordinate transformation from $\boldsymbol{\rho}_0$ and $\boldsymbol{\rho}_0'$ to $\boldsymbol{\rho}_{0_+} \equiv (\boldsymbol{\rho}_0 + \boldsymbol{\rho}_0')/2$ and $\boldsymbol{\rho}_{0_-} \equiv \boldsymbol{\rho}_0 - \boldsymbol{\rho}_0'$, we can reduce Eq. (C.21) to

$$
\begin{aligned}
&W_{\mathcal{E}_L}(\boldsymbol{\rho}_+, \mathbf{k}, \omega_+, \omega_-) \\
&= \int \mathrm{d}^2 \boldsymbol{\rho}_- \int \mathrm{d}^2 \boldsymbol{\rho}_{0_+} \int \mathrm{d}^2 \boldsymbol{\rho}_{0_-} \, \langle \mathcal{E}_0(\boldsymbol{\rho}_{0_+} + \boldsymbol{\rho}_{0_-}/2, \omega_+ + \omega_-/2) \mathcal{E}_0^*(\boldsymbol{\rho}_{0_+} - \boldsymbol{\rho}_{0_-}/2, \omega_+ - \omega_-/2) \rangle \\
&\quad \times \frac{e^{i\omega_- L/c}}{(\lambda_0 L)^2} e^{i(\omega_0+\omega_+)(\boldsymbol{\rho}_+-\boldsymbol{\rho}_{0_+})\cdot(\boldsymbol{\rho}_--\boldsymbol{\rho}_{0_-})/cL} e^{i\omega_-(|\boldsymbol{\rho}_+-\boldsymbol{\rho}_{0_+}|^2+|\boldsymbol{\rho}_--\boldsymbol{\rho}_{0_-}|^2/4)/2cL} e^{-i\mathbf{k}\cdot\boldsymbol{\rho}_-}.
\end{aligned} \tag{C.22}
$$

Rearranging terms allows us to put the $\boldsymbol{\rho}_-$ integral inside the $\boldsymbol{\rho}_{0_+}$ and $\boldsymbol{\rho}_{0_-}$ integrals, i.e.,

$$
\begin{aligned}
&W_{\mathcal{E}_L}(\boldsymbol{\rho}_+, \mathbf{k}, \omega_+, \omega_-) \\
&= \int \mathrm{d}^2 \boldsymbol{\rho}_{0_+} \int \mathrm{d}^2 \boldsymbol{\rho}_{0_-} \, \langle \mathcal{E}_0(\boldsymbol{\rho}_{0_+} + \boldsymbol{\rho}_{0_-}/2, \omega_+ + \omega_-/2) \mathcal{E}_0^*(\boldsymbol{\rho}_{0_+} - \boldsymbol{\rho}_{0_-}/2, \omega_+ - \omega_-/2) \rangle \frac{e^{i\omega_- L/c}}{(\lambda_0 L)^2} \\
&\quad \times e^{-i(\omega_0+\omega_+)(\boldsymbol{\rho}_+-\boldsymbol{\rho}_{0_+})\cdot\boldsymbol{\rho}_{0_-}/cL} e^{i\omega_-(|\boldsymbol{\rho}_+-\boldsymbol{\rho}_{0_+}|^2/2cL+|\boldsymbol{\rho}_{0_-}|^2/8cL)} \\
&\quad \times \int \mathrm{d}^2 \boldsymbol{\rho}_- \, e^{i\omega_-|\boldsymbol{\rho}_-|^2/8cL} e^{-i[\mathbf{k}-(\omega_0+\omega_+)(\boldsymbol{\rho}_+-\boldsymbol{\rho}_{0_+})/cL+\omega_-\boldsymbol{\rho}_{0_-}/4cL)]\cdot\boldsymbol{\rho}_-}.
\end{aligned} \tag{C.23}
$$

---

[1] For notational convenience, we have assumed that the diffraction takes place between the $z = 0$ and $z = L$ planes, but the result we obtain will apply for $+z$-going Fresnel diffraction over a distance L starting from an arbitrary z plane.

Performing the $\boldsymbol{\rho}_-$ integral then yields

$$W_{\mathcal{E}_L}(\boldsymbol{\rho}_+, \mathbf{k}, \omega_+, \omega_-)$$

$$= \int \mathrm{d}^2\boldsymbol{\rho}_{0_+} \int \mathrm{d}^2\boldsymbol{\rho}_{0_-} \langle \mathcal{E}_0(\boldsymbol{\rho}_{0_+} + \boldsymbol{\rho}_{0_-}/2, \omega_+ + \omega_-/2)\mathcal{E}_0^*(\boldsymbol{\rho}_{0_+} - \boldsymbol{\rho}_{0_-}/2, \omega_+ - \omega_-/2)\rangle \frac{e^{i\omega_- L/c}}{(\lambda_0 L)^2}$$

$$\times e^{-i(\omega_0+\omega_+)(\boldsymbol{\rho}_+-\boldsymbol{\rho}_{0_+})\cdot\boldsymbol{\rho}_{0_-}/cL}e^{i\omega_-|\boldsymbol{\rho}_+-\boldsymbol{\rho}_{0_+}|^2/2cL}e^{i\omega_-|\boldsymbol{\rho}_{0_-}|^2/8cL}(i8\pi cL/\omega_-)$$

$$\times e^{-2icL|\mathbf{k}-(\omega_0+\omega_+)(\boldsymbol{\rho}_+-\boldsymbol{\rho}_{0_+})/cL+\omega_-\boldsymbol{\rho}_{0_-}/4cL|^2/\omega_-}, \tag{C.24}$$

which, after some terms cancel, gives

$$W_{\mathcal{E}_L}(\boldsymbol{\rho}_+, \mathbf{k}, \omega_+, \omega_-)$$

$$= \int \mathrm{d}^2\boldsymbol{\rho}_{0_+} \int \mathrm{d}^2\boldsymbol{\rho}_{0_-} \langle \mathcal{E}_0(\boldsymbol{\rho}_{0_+} + \boldsymbol{\rho}_{0_-}/2, \omega_+ + \omega_-/2)\mathcal{E}_0^*(\boldsymbol{\rho}_{0_+} - \boldsymbol{\rho}_{0_-}/2, \omega_+ - \omega_-/2)\rangle$$

$$\times \frac{e^{i\omega_- L/c}}{(\lambda_0 L)^2}e^{i\omega_-|\boldsymbol{\rho}_+-\boldsymbol{\rho}_{0_+}|^2/2cL}e^{-2icL|\mathbf{k}-(\omega_0+\omega_+)(\boldsymbol{\rho}_+-\boldsymbol{\rho}_{0_+})/cL|^2/\omega_-}e^{-i\mathbf{k}\cdot\boldsymbol{\rho}_{0_-}}(i8\pi cL/\omega_-) \tag{C.25}$$

$$= \int \mathrm{d}^2\boldsymbol{\rho}_{0_+} W_{\mathcal{E}_0}(\boldsymbol{\rho}_{0_+}, \mathbf{k}, \omega_+, \omega_-)\frac{e^{i\omega_- L/c}}{(\lambda_0 L)^2}e^{i\omega_-|\boldsymbol{\rho}_+-\boldsymbol{\rho}_{0_+}|^2/2cL}$$

$$\times e^{-2icL|\mathbf{k}-(\omega_0+\omega_+)(\boldsymbol{\rho}_+-\boldsymbol{\rho}_{0_+})/cL|^2/\omega_-}(i8\pi cL/\omega_-). \tag{C.26}$$

The term

$$e^{-2icL|\mathbf{k}-(\omega_0+\omega_+)(\boldsymbol{\rho}_+-\boldsymbol{\rho}_{0_+})/cL|^2/\omega_-}i8\pi cL/\omega_-(\lambda_0 L)^2$$

in Eq. (C.26)'s integrand behaves like the impulse $\delta[\boldsymbol{\rho}_{0+} - \boldsymbol{\rho}_+ + kcL/(\omega_0 + \omega_+)]$. This delta-function behavior follows because: (1) The term in question is a highly-oscillatory function outside of a narrow slow-oscillation region that is centered at $\boldsymbol{\rho}_+ - kcL/(\omega_0 + \omega_+)$ with nominal width $\sqrt{\omega_- cL}/2(\omega_0 + \omega_+)$, and $\omega_0 \gg \max|\omega_+|$ implies that it integrates to one. (2) The other $\boldsymbol{\rho}_{0_+}$-dependent terms in Eq. (C.26) are the oscillatory term, $\exp(i\omega_-|\boldsymbol{\rho}_+ - \boldsymbol{\rho}_{0_+}|^2/2cL)$, which varies much more slowly than its predecessor, because $\omega_0 \gg \max|\omega_-|$, and the Wigner distribution, whose $\boldsymbol{\rho}_{0_+}$ dependence can reasonably be assumed to be nearly constant over regions of diameter

$\sqrt{\omega_- cL}/2(\omega_0 + \omega_+)$. So, using the delta-function approximation in Eq. (C.26), we get

$$W_{\mathcal{E}_L}(\boldsymbol{\rho}_+, \mathbf{k}, \omega_+, \omega_-) = W_{\mathcal{E}_0'}\left(\boldsymbol{\rho}_+ - \frac{cL\mathbf{k}}{(\omega_0 + \omega_+)}, \mathbf{k}, \omega_+, \omega_-\right) e^{i\frac{\omega_- L}{c}\left(1 + \frac{c^2|\mathbf{k}|^2}{2(\omega_0 + \omega_+)^2}\right)}. \quad \text{(C.27)}$$

Finally, again making use $\omega_0 \gg \omega_+$, we have

$$W_{\mathcal{E}_L}(\boldsymbol{\rho}_+, \mathbf{k}, \omega_+, \omega_-) = W_{\mathcal{E}_0'}\left(\boldsymbol{\rho}_+ - \frac{cL\mathbf{k}}{\omega_0}, \mathbf{k}, \omega_+, \omega_-\right) e^{i\frac{\omega_- L}{c}\left(1 + \frac{c^2|\mathbf{k}|^2}{2\omega_0^2}\right)}. \quad \text{(C.28)}$$

As a consistency check on Eq. (C.28), let us use it to calculate $\mathcal{P}_L(\boldsymbol{\rho}_+, \omega_-)$ when $z = 0$ illumination with TFSWD $W_{\mathcal{E}_0}(\boldsymbol{\rho}_{0_+}, \mathbf{k}, \omega_+, \omega_-)$ passes through the diffuser specified in Eq. (C.1) before undergoing Fresnel diffraction over a distance L. We then have that

$$\mathcal{P}_L(\boldsymbol{\rho}_+, \omega_-) = \int \frac{\mathrm{d}\omega_+}{2\pi} \int \frac{\mathrm{d}^2\mathbf{k}}{(2\pi)^2} W_{\mathcal{E}_0'}\left(\boldsymbol{\rho}_+ - \frac{cL\mathbf{k}}{\omega_0}, \mathbf{k}, \omega_+, \omega_-\right) e^{i\frac{\omega_- L}{c}\left(1 + \frac{c^2|\mathbf{k}|^2}{2\omega_0^2}\right)}. \quad \text{(C.29)}$$

Using Eq. (C.6) now gives us

$$\mathcal{P}_L(\boldsymbol{\rho}_+, \omega_-) = \lambda_0^2 \int \frac{\mathrm{d}\omega_+}{2\pi} \int \frac{\mathrm{d}^2\mathbf{k}}{(2\pi)^2} \int \frac{\mathrm{d}^2\mathbf{k}'}{(2\pi)^2} W_{\mathcal{E}_0'}\left(\boldsymbol{\rho}_+ - \frac{cL\mathbf{k}}{\omega_0}, \mathbf{k}', \omega_+, \omega_-\right) e^{i\frac{\omega_- L}{c}\left(1 + \frac{c^2|\mathbf{k}|^2}{2\omega_0^2}\right)}.$$
$$\text{(C.30)}$$

Changing variables so that $\mathbf{k} = \omega_0(\boldsymbol{\rho}_+ - \boldsymbol{\rho}_0)/cL$ leaves us with

$$\mathcal{P}_L(\boldsymbol{\rho}_+, \omega_-) = \int \frac{\mathrm{d}\omega_+}{2\pi} \int \mathrm{d}^2\boldsymbol{\rho}_0 \int \frac{\mathrm{d}^2\mathbf{k}'}{(2\pi)^2} W_{\mathcal{E}_0}(\boldsymbol{\rho}_0, \mathbf{k}', \omega_+, \omega_-) \frac{e^{i\frac{\omega_- L}{c}(1 + |\boldsymbol{\rho}_+ - \boldsymbol{\rho}_0|^2/2L^2)}}{L^2} \quad \text{(C.31)}$$

which reduces to the result from Chapter. 2,

$$\mathcal{P}_L(\boldsymbol{\rho}_+, \omega_-) = \int \mathrm{d}^2\boldsymbol{\rho}_0 \, \mathcal{P}_0(\boldsymbol{\rho}_0, \omega_-) \frac{e^{i\omega_- L/c} e^{i\omega_- |\boldsymbol{\rho}_+ - \boldsymbol{\rho}_0|^2/2cL}}{L^2}, \quad \text{(C.32)}$$

by virtue of Eq. (3.14).

Appendix D

Synthetic-Wavelength-Holography Approach

In this appendix, we will develop the synthetic-wavelength-holography approach of Willomitzer *et al.* [14] in our $\mathcal{P}$-field framework. Within the limitations of current laser and detector technology, this approach offers a more practical method to access higher $\mathcal{P}$-field frequencies than is possible with the naive approach of modulating incident illumination then directly detecting the returning diffuser-averaged STA irradiance and computing its spectrum. To begin, consider the simple $\mathcal{P}$ field associated with single-frequency irradiance modulation at angular frequency Ω:

$$\mathcal{P}(\boldsymbol{\rho},\omega_-) = \mathcal{P}_\Omega^*(\boldsymbol{\rho})2\pi\delta(\omega_- + \Omega) + \mathcal{P}_0(\boldsymbol{\rho})2\pi\delta(\omega_-) + \mathcal{P}_\Omega(\boldsymbol{\rho})2\pi\delta(\omega_- - \Omega). \qquad \text{(D.1)}$$

It consists of three peaks, one at zero frequency, one at the modulation frequency, and one at the negated modulation frequency. The zero-frequency component $\mathcal{P}_0(\boldsymbol{\rho})$ is positive, owing to the positivity of the diffuser-averaged STA irradiance. The fact that the modulation-frequency components have a conjugate relationship follows from the diffuser-averaged STA irradiance's being real valued. Moreover, $|\mathcal{P}_\Omega(\boldsymbol{\rho})| \leq \mathcal{P}_0(\boldsymbol{\rho})/2$ is required because the STA irradiance is non-negative. So, this represents the simplest physical $\mathcal{P}$ field one can generate. One way to generate it is by coherently summing optical fields at two angular frequencies, ω_1 and ω_2. Taking $\omega_1 = \omega_0$ to be our

optical frequency and $\omega_2 = \omega_0 + \Delta\omega$ to be detuned from ω_0 by $\Delta\omega = \omega_2 - \omega_1$, the frequency-domain complex field envelope associated with such a signal is then

$$\mathcal{E}(\boldsymbol{\rho}, \omega) = \mathcal{E}_{\omega_1}(\boldsymbol{\rho}) 2\pi \delta(\omega) + \mathcal{E}_{\omega_2}(\boldsymbol{\rho}) 2\pi \delta(\omega - \Delta\omega). \tag{D.2}$$

The $\mathcal{P}$ field associated with this complex field envelope is given by

$$\mathcal{P}(\boldsymbol{\rho}, \omega_-) = \int \frac{\mathrm{d}\omega_+}{2\pi} \langle \mathcal{E}(\boldsymbol{\rho}, \omega_+ + \omega_-/2) \mathcal{E}^*(\boldsymbol{\rho}, \omega_+ - \omega_-/2) \rangle \tag{D.3}$$

$$= \langle \mathcal{E}_{\omega_1}(\boldsymbol{\rho}) \mathcal{E}_{\omega_2}^*(\boldsymbol{\rho}) \rangle 2\pi \delta(\omega_- + \Delta\omega) + (\langle |\mathcal{E}_{\omega_1}(\boldsymbol{\rho})|^2 \rangle + \langle |\mathcal{E}_{\omega_2}(\boldsymbol{\rho})|^2 \rangle) 2\pi \delta(\omega_-)$$

$$+ \langle \mathcal{E}_{\omega_1}^*(\boldsymbol{\rho}) \mathcal{E}_{\omega_2}(\boldsymbol{\rho}) \rangle 2\pi \delta(\omega_- - \Delta\omega). \tag{D.4}$$

This is a single-frequency $\mathcal{P}$ field for frequency $\Delta\omega$. In particular, we have that

$$\mathcal{P}_0(\boldsymbol{\rho}) = \langle |\mathcal{E}_{\omega_1}(\boldsymbol{\rho})|^2 \rangle + \langle |\mathcal{E}_{\omega_2}(\boldsymbol{\rho})|^2 \rangle \tag{D.5a}$$

$$\mathcal{P}_{\Delta\omega}(\boldsymbol{\rho}) = \langle \mathcal{E}_{\omega_1}^*(\boldsymbol{\rho}) \mathcal{E}_{\omega_2}(\boldsymbol{\rho}) \rangle. \tag{D.5b}$$

For systems that are linear and time invariant with respect to the optical field—as is true for all elements discussed in this thesis—the frequency structure of the $\mathcal{P}$ field and complex field envelope remain unchanged, and our goal becomes simply to relate the input quantities to the output quantities at each frequency. For single-frequency modulation in particular this means that there exist relations

$$\mathcal{E}_{\mathrm{in},\omega_1}(\boldsymbol{\rho}) \rightarrow \mathcal{E}_{\mathrm{out},\omega_1}(\boldsymbol{\rho}) \tag{D.6}$$

$$\mathcal{E}_{\mathrm{in},\omega_2}(\boldsymbol{\rho}) \rightarrow \mathcal{E}_{\mathrm{out},\omega_2}(\boldsymbol{\rho}) \tag{D.7}$$

$$\mathcal{P}_{\mathrm{in},0}(\boldsymbol{\rho}) \rightarrow \mathcal{P}_{\mathrm{out},0}(\boldsymbol{\rho}) \tag{D.8}$$

$$\mathcal{P}_{\mathrm{in},\Delta\omega}(\boldsymbol{\rho}) \rightarrow \mathcal{P}_{\mathrm{out},\Delta\omega}(\boldsymbol{\rho}), \tag{D.9}$$

and that these relations suffice to fully characterize the phasor-field input-output behavior. Provided diffuser averaging can be accounted for, it follows from Eq. (D.5)

that the relations for the complex field envelope suffice to characterize the relations for the $\mathcal{P}$ field. More importantly, for linear time-invariant systems, the input-output relations for $\mathcal{E}_{\omega_1}(\boldsymbol{\rho})$ and $\mathcal{E}_{\omega_2}(\boldsymbol{\rho})$ are the same as the complex-field-envelope input-output relations for illuminating the system with unmodulated light at each frequency *individually.* The implication is that, provided we can accurately measure the output complex field envelope and account for diffuser averaging, phasor-field imaging tasks can be carried out by *sequentially* illuminating the system with unmodulated inputs, meaning we are not burdened by needing direct detectors that are sufficiently fast to capture the $\mathcal{P}$-field modulation frequency. We will turn now to each of these concerns.
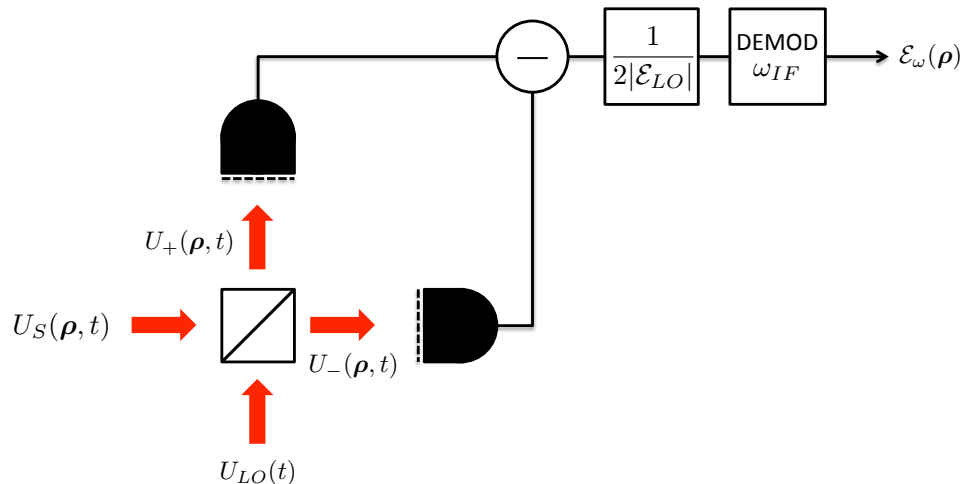

Figure D-1: Setup for balanced heterodyne detection. The signal field is combined with a strong local oscillator, detuned from the optical frequency by ω_{IF}, on a 50-50 beam splitter. The outputs of the beam splitter are detected with arrays of photodetectors (shown by the dashed lines). The two detection signals are subtracted, then twice the local oscillator amplitude is divided out, and the resulting signal is demodulated at ω_{IF}. The result is a detection of the signal field's complex field envelope.

To measure the output complex field envelope, we propose using balanced heterodyne detection, as depicted in Fig. D-1. The signal—characterized by positive-frequency optical field $U_S(\boldsymbol{\rho}, t) = \mathcal{E}_\omega(\boldsymbol{\rho})e^{-i\omega t}$—is mixed on a 50-50 beam splitter with a strong, plane-wave local oscillator—characterized by positive-frequency optical field $U_{LO}(t) = \mathcal{E}_{LO}e^{-i(\omega-\omega_{IF})t}$—detuned from the optical frequency by an intermediate frequency ω_{IF} that is slow enough for electronics to capture. The positive-

frequency optical fields at the output arms of the beam splitter are given by $U_{\pm}(\boldsymbol{\rho}, t) = (U_S(\boldsymbol{\rho}, t) \pm U_{LO}(t))/\sqrt{2}$. Each output arm is then directly detected, at high spatial resolution, i.e., with a detector array. For simplicity, we will assume ideal continuum photodetection. We will also ignore the effects of noise[1] and assume the detectors have unity quantum efficiency $\eta = 1$. In effect, we take each detector to accurately detect the STA irradiance, at full spatial resolution:

$$I_{\pm}(\boldsymbol{\rho}, t) = |U_{\pm}(\boldsymbol{\rho}, t)|^2 \tag{D.10}$$

$$= \frac{|\mathcal{E}_{\omega}(\boldsymbol{\rho})|^2 + |\mathcal{E}_{LO}|^2}{2} \pm \Re\left[\mathcal{E}_{LO}^* \mathcal{E}_{\omega}(\boldsymbol{\rho}) e^{-i\omega_{IF} t}\right]. \tag{D.11}$$

We then subtract the two detector outputs and divide[2] by twice the local oscillator amplitude, leaving

$$\frac{I_{+}(\boldsymbol{\rho}, t) - I_{-}(\boldsymbol{\rho}, t)}{2|\mathcal{E}_{LO}|} = \Re\left[\mathcal{E}_{\omega}(\boldsymbol{\rho}) e^{-i(\omega_{IF} t - \theta)}\right], \tag{D.12}$$

where $\mathcal{E}_{LO} = |\mathcal{E}_{LO}| e^{i\theta}$. The desired optical-frequency complex-field envelope now appears at the intermediate frequency. Thus the quadratures of that signal can be extracted by standard communication electronics and we obtain $\mathcal{E}_{\omega}(\boldsymbol{\rho})$. Applying this technique at the output of the system of interest and sequentially illuminating the input at frequencies ω_1 and ω_2 allows us to recover $\mathcal{E}_{\text{out}, \omega_1}(\boldsymbol{\rho})$ and $\mathcal{E}_{\text{out}, \omega_2}(\boldsymbol{\rho})$.

Now we can computationally form $\mathcal{E}_{\text{out}, \omega_1}^*(\boldsymbol{\rho}) \mathcal{E}_{\text{out}, \omega_2}(\boldsymbol{\rho})$,[3] but we still need to account for diffuser averaging. Unfortunately, it does not suffice to rely on our detectors averaging over multiple speckles, as we did in Chapter 5. In fact, if our detector elements are large enough to do so, we lose the signal entirely in that

$$\left\langle \frac{I_{+}(\boldsymbol{\rho}, t) - I_{-}(\boldsymbol{\rho}, t)}{2|E_{LO}|} \right\rangle = \Re\left[\langle \mathcal{E}_{\omega}(\boldsymbol{\rho}) \rangle e^{-i(\omega_{IF} t - \theta)}\right] = 0. \tag{D.13}$$

---

[1] A strong local oscillator serves to increase the signal-to-noise ratio of the direct detection, as compared to detecting the signal field alone. However, some fundamental quantum noise is unavoidable.

[2] A physical implementation would omit this division. However, it serves here to improve the aesthetics of the theory.

[3] Since the information relevant to imaging tasks is encoded in the modulation frequency component of the $\mathcal{P}$ field, we ignore the zero-frequency component, although that too could be computed.

So, it is critical that we use high-enough resolution detectors to resolve the speckle pattern. In practice, we want no more than a few speckle cells to fall on a single pixel of our detector to avoid the associated signal attenuation. Instead, we propose low-pass spatial filtering our computed correlation with a $e^{-1/2}$-attenuation-radius-R Gaussian spatial filter to generate an estimate, $\hat{\mathcal{P}}_{\mathrm{out},\Delta\omega}(\boldsymbol{\rho})$, given by

$$\hat{\mathcal{P}}_{\mathrm{out},\Delta\omega}(\boldsymbol{\rho}) \equiv \frac{1}{2\pi R^2} \int \mathrm{d}^2\tilde{\boldsymbol{\rho}}\, e^{-|\boldsymbol{\rho}-\tilde{\boldsymbol{\rho}}|^2/2R^2} \mathcal{E}^*_{\mathrm{out},\omega_1}(\tilde{\boldsymbol{\rho}}) \mathcal{E}_{\mathrm{out},\omega_2}(\tilde{\boldsymbol{\rho}}). \tag{D.14}$$

Provided that our filter is finer than the spatial feature size of the $\mathcal{P}$ field, viz. $R < \Delta\lambda \equiv 2\pi c/\Delta\omega$, then this is an approximately unbiased estimate of the desired $\mathcal{P}$-field component:

$$\langle\hat{\mathcal{P}}_{\mathrm{out},\Delta\omega}(\boldsymbol{\rho})\rangle = \frac{1}{2\pi R^2} \int \mathrm{d}^2\tilde{\boldsymbol{\rho}}\, e^{-|\boldsymbol{\rho}-\tilde{\boldsymbol{\rho}}|^2/2R^2} \langle\mathcal{E}^*_{\mathrm{out},\omega_1}(\tilde{\boldsymbol{\rho}}) \mathcal{E}_{\mathrm{out},\omega_2}(\tilde{\boldsymbol{\rho}})\rangle \tag{D.15}$$

$$= \frac{1}{2\pi R^2} \int \mathrm{d}^2\tilde{\boldsymbol{\rho}}\, e^{-|\boldsymbol{\rho}-\tilde{\boldsymbol{\rho}}|^2/2R^2} \mathcal{P}_{\mathrm{out},\Delta\omega}(\boldsymbol{\rho}) \tag{D.16}$$

$$\approx \mathcal{P}_{\mathrm{out},\Delta\omega}(\boldsymbol{\rho}). \tag{D.17}$$

What remains then is to assess our estimate's variance. To do so, we hark back to our speckle analysis in Chapter 5, and consider the three-bounce scenario from Fig. 5-1 with the input illumination of Eq. (5.1), taking $\boldsymbol{\mu} = 0$ without loss of generality: $\mathcal{E}_{\mathrm{in},\omega_1}(\boldsymbol{\rho}_0) = \mathcal{E}_{\mathrm{in},\omega_2}(\boldsymbol{\rho}_0) = E_0(\boldsymbol{\rho}_0; 0)$. Since we're probing the system sequentially at each frequency, our unmodulated analysis from Chapter 5 suffices. Moreover, as in Chapter 5, we will assume that there is no albedo pattern on the hidden plane. Furthermore, we shall also assume that the Fresnel numbers Ω_{01} and Ω_{12} are large enough that the third-bounce speckle is well-approximated as single-bounce speckle from the final diffuser, so that the output complex field envelope is Gaussian dis-

tributed. Under these conditions, Gaussian moment factoring gives us

$$
\begin{aligned}
\text{var}(\hat{\mathcal{P}}_{\text{out},\Delta\omega}(\boldsymbol{\rho})) = & \langle|\hat{\mathcal{P}}_{\text{out},\Delta\omega}(\boldsymbol{\rho})|^2\rangle - |\langle\hat{\mathcal{P}}_{\text{out},\Delta\omega}(\boldsymbol{\rho})\rangle|^2 \\
= & \frac{1}{4\pi^2 R^4}\int d^2\boldsymbol{\rho}_3 \int d^2\tilde{\boldsymbol{\rho}}_3\, e^{-(|\boldsymbol{\rho}-\boldsymbol{\rho}_3|^2+|\boldsymbol{\rho}-\tilde{\boldsymbol{\rho}}_3|^2)/2R^2} \\
& \times \langle\mathcal{E}^*_{\text{out},\omega_1}(\boldsymbol{\rho}_3)\mathcal{E}_{\text{out},\omega_1}(\tilde{\boldsymbol{\rho}}_3)\rangle\langle\mathcal{E}_{\text{out},\omega_2}(\boldsymbol{\rho}_3)\mathcal{E}^*_{\text{out},\omega_2}(\tilde{\boldsymbol{\rho}}_3)\rangle, & \text{(D.18)}
\end{aligned}
$$

where

$$
\mathcal{E}_{\text{out},\omega}(\boldsymbol{\rho}_3) = \mathcal{E}_{3,\omega}(\boldsymbol{\rho}_3) = \frac{\omega}{i2\pi cL}e^{i\omega L/c}\int d^2\boldsymbol{\rho}_2\,\mathcal{E}_{2,\omega}(\boldsymbol{\rho}_2)e^{i\omega|\boldsymbol{\rho}_3-\boldsymbol{\rho}_2|^2/2cL}e^{i\omega h_2(\boldsymbol{\rho}_2)/c}e^{-4|\boldsymbol{\rho}_2|^2/d_2^2},
$$

$$\text{(D.19)}$$

and similar relations hold for the previous bounces. Accordingly, we find that

$$
\langle\mathcal{E}^*_{\text{out},\omega}(\boldsymbol{\rho}_3)\mathcal{E}_{\text{out},\omega}(\tilde{\boldsymbol{\rho}}_3)\rangle = \langle I_3\rangle e^{-\frac{\omega^2 d_2^2}{32c^2L^2}|\boldsymbol{\rho}_3-\tilde{\boldsymbol{\rho}}_3|^2}e^{-i\omega(|\boldsymbol{\rho}_3|^2-|\tilde{\boldsymbol{\rho}}_3|^2)/2cL}, \qquad \text{(D.20)}
$$

with $\langle I_3\rangle$ as in Eq. (5.8). This in turn implies

$$
\begin{aligned}
\text{var}(\hat{\mathcal{P}}_{\text{out},\Delta\omega}(\boldsymbol{\rho})) = & \frac{\langle I_3\rangle^2}{4\pi^2 R^4}\int d^2\boldsymbol{\rho}_3 \int d^2\tilde{\boldsymbol{\rho}}_3\, e^{-(|\boldsymbol{\rho}-\boldsymbol{\rho}_3|^2+|\boldsymbol{\rho}-\tilde{\boldsymbol{\rho}}_3|^2)/2R^2} \\
& \times e^{-\frac{(\omega_0^2+(\omega_0+\Delta\omega)^2)d_2^2}{32c^2L^2}|\boldsymbol{\rho}_3-\tilde{\boldsymbol{\rho}}_3|^2}e^{i\Delta\omega(|\boldsymbol{\rho}_3|^2-|\tilde{\boldsymbol{\rho}}_3|^2)/2cL} & \text{(D.21)} \\
= & \frac{\langle I_3\rangle^2\exp\left(-\Delta\omega^2 R^2|\boldsymbol{\rho}|^2/c^2L^2Z(R)\right)}{Z(R)}, & \text{(D.22)}
\end{aligned}
$$

where

$$
Z(R) \equiv 1 + \frac{\Delta\omega^2 R^4}{c^2L^2} + \frac{d_2^2 R^2}{8c^2L^2}(\omega_1^2+\omega_2^2). \qquad \text{(D.23)}
$$

Equation (D.22) takes its maximum value at $\boldsymbol{\rho}=\mathbf{0}$, so we'll limit our attention to that bound. It's not hard to see that $|\langle\hat{\mathcal{P}}_{\text{out},\Delta\omega}(\boldsymbol{\rho})\rangle|^2 = \langle I_3\rangle^2$, and so the ratio of the squared mean to the variance is bounded below by

$$
\frac{|\langle\hat{\mathcal{P}}_{\text{out},\Delta\omega}(\boldsymbol{\rho})\rangle|^2}{\text{var}(\hat{\mathcal{P}}_{\text{out},\Delta\omega}(\boldsymbol{\rho}))} \geq \frac{|\langle\hat{\mathcal{P}}_{\text{out},\Delta\omega}(\boldsymbol{\rho})\rangle|^2}{\text{var}(\hat{\mathcal{P}}_{\text{out},\Delta\omega}(\mathbf{0}))} = Z(R). \qquad \text{(D.24)}
$$

It's clear that the variance approaches zero as R gets large. However, we'd like to find that the variance is significantly less than the squared mean for a small enough value of R that we don't destroy the $\mathcal{P}$ field's spatial detail. Taking reasonable parameter values $\lambda_0 = 532\,\text{nm}$, $L = 1\,\text{m}$, $d_2 = 2\,\text{m}$, we ambitiously take the difference frequency to be $\Delta\omega/2\pi = 1\,\text{THz}$ so that $\Delta\lambda = 300\,\mu\text{m}$. Even setting our low-pass-filter width as small as $R = 1\,\mu\text{m}$ we find $Z(1\,\mu\text{m}) \approx 141$, implying that the squared mean greatly exceeds the variance, and so $\hat{\mathcal{P}}_{\text{out},\Delta\omega}(\boldsymbol{\rho}) \approx \mathcal{P}_{\text{out},\Delta\omega}(\boldsymbol{\rho})$. Of course, we have traded the need for exceedingly good time resolution in detection for exceedingly good spatial resolution, as sub-micron pixel sizes (to avoid speckle averaging at the detectors) seem unrealistic. Moreover, our thin diffusers model a surface scattering process, and for NLoS imaging applications, subsurface-scattering phenomena may become significant at THz-scale frequency differences. Nevertheless, Willomitzer *et al.* [14] have provided some promising proofs-of-concept for this technique in experimental NLoS imaging scenarios.

Bibliography

[1] Kirmani, A., Hutchison, T., Davis, J. & Raskar, R. Looking around the corner using ultrafast transient imaging. *International Journal of Computer Vision* **95**, 13–28 (2011).

[2] Velten, A. *et al.* Recovering three-dimensional shape around a corner using ultrafast time-of-flight imaging. *Nature Communications* **3**, 745 (2012).

[3] Heide, F., Xiao, L., Heidrich, W. & Hullin, M. B. Diffuse mirrors: 3D reconstruction from diffuse indirect illumination using inexpensive time-of-flight sensors. *2014 IEEE Conference on Computer Vision and Pattern Recognition (CVPR)* 3222–3229 (2014).

[4] Buttafava, M., Zeman, J., Tosi, A., Eliceiri, K. & Velten, A. Non-line-of-sight imaging using a time-gated single photon avalanche diode. *Opt. Express* **23**, 20997–21011 (2015).

[5] Gariepy, G., Tonolini, F., Henderson, R., Leach, J. & Faccio, D. Detection and tracking of moving objects hidden from view. *Nature Photonics* **10**, 23–26 (2015).

[6] Kadambi, A., Zhao, H., Shi, B. & Raskar, R. Occluded imaging with time-of-flight sensors. *ACM Transactions on Graphics* **35**, 1–12 (2016).

[7] Klein, J., Laurenzis, M. & Hullin, M. Transient imaging for real-time tracking around a corner. *Proc. SPIE* **9988**, 998802 (2016).

[8] O'Toole, M., Lindell, D. B. & Wetzstein, G. Confocal non-line-of-sight imaging based on the light-cone transform. *Nature* **555**, 338—341 (2018).

[9] Reza, S. A., Manna, M. L., Bauer, S. & Velten, A. Phasor field waves: A Huygens-like light transport model for non-line-of-sight imaging applications. *Opt. Express* **27**, 29380–29400 (2019).

[10] Liu, X. *et al.* Non-line-of-sight imaging using phasor-field virtual waveoptics. *Nature* **572**, 620–623 (2019).

[11] Xu, F. *et al.* Revealing hidden scenes by photon-efficient occlusion-based opportunistic active imaging. *Opt. Express* **26**, 9945–9962 (2018).

[12] Thrampoulidis, C. *et al.* Exploiting occlusion in non-line-of-sight active imaging. *IEEE Transactions on Computational Imaging* **4**, 419–431 (2018).

[13] Reza, S. A., Manna, M. L., Bauer, S. & Velten, A. Phasor field waves: experimental demonstrations of wave-like properties. *Opt. Express* **27**, 32587–32608 (2019).

[14] Willomitzer, F. *et al.* Synthetic wavelength holography: An extension of Gabor's holographic principle to imaging with scattered wavefronts arXiv:1912.11438 [physics.optics] (2019).

[15] Ishimaru, A. *Wave Propagation and Scattering in Random Media, Vol 1: Single Scattering and Transport Theory* (Academic, New York, 1978).

[16] Gershun, A. The light field. *Journal of Mathematics and Physics* **18**, 51–151 (1939).

[17] Adelson, E. H. & Bergen, J. R. The plenoptic function and the elements of early vision. In *Computational Models of Visual Processing*, 3–20 (MIT Press, 1991).

[18] Levoy, M. & Hanrahan, P. Light field rendering. In *Proceedings of the 23rd Annual Conference on Computer Graphics and Interactive Techniques*, SIGGRAPH '96, 31–42 (ACM, New York, NY, USA, 1996).

[19] Walther, A. Radiometry and coherence. *J. Opt. Soc. Am.* **58**, 1256–1259 (1968).

[20] Bastiaans, M. J. Wigner distribution function and its application to first-order optics. *J. Opt. Soc. Am.* **69**, 1710–1716 (1979).

[21] Alonso, M. A. Wigner functions in optics: describing beams as ray bundles and pulses as particle ensembles. *Adv. Opt. Photon.* **3**, 272–365 (2011).

[22] Ishimaru, A. *Wave Propagation and Scattering in Random Media, Vol 2: Multiple Scattering, Turbulence, Rough Surfaces, and Remote Sensing* (Academic, New York, 1978).

[23] Hecht, E. *Optics* (Addison-Wesley, 2002). Section 10.3.4: Circular Obstacles, pg. 494.

[24] Goodman, J. W. *Introduction to Fourier Optics* (McGraw-Hill, San Francisco, 1968). Eq. (3-26).

[25] Mandel, L. & Wolf, E. *Optical Coherence and Quantum Optics* (Cambridge University Press, 1995).

[26] Goodman, J. W. *Speckle Phenomena in Optics* (Roberts & Company, Englewood, Colorado, 2007).

[27] Teichman, J. A. Phasor field waves: a mathematical treatment. *Opt. Express* **27**, 27500–27506 (2019).

[28] Weisstein, E. W. Meijer G-Function. URL `http://mathworld.wolfram.com/MeijerG-Function.html`. Accessed 11/18/2019.

[29] Wikipedia contributors. Meijer G-function — Wikipedia, the free encyclopedia (2019). URL `https://en.wikipedia.org/w/index.php?title=Meijer_G-function&oldid=915962192`. Accessed 11/20/2019.

[30] Foix, S., Alenya, G. & Torras, C. Lock-in time-of-flight (ToF) cameras: A survey. *IEEE Sensors Journal* **11**, 1917–1926 (2011).

[31] Heliotis heliCam C3 documentation. URL `https://www.heliotis.com/en/lock-in-camera/`.

[32] Birks, T. A., Gris-Sánchez, I., Yerolatsitis, S., Leon-Saval, S. G. & Thomson, R. R. The photonic lantern. *Adv. Opt. Photon.* **7**, 107–167 (2015).